Portable Mass Spectrometry for Residual Gas Analysis

Thesis submitted in accordance with the requirements of the

University of Liverpool for the degree of

Doctor in Philosophy

by

Jeyan Sreekumar

Department of Electrical Engineering and Electronics

The University of Liverpool

September 2010

Abstract

This work is mainly concerned with the modelling of mass spectra of gases using the quadrupole mass spectrometer (*QMS*) model developed in the University of Liverpool. This model is capable of the accurate simulation of mass spectra for both hyperbolic and circular electrode shapes, allowing the user to specify different values of mass spectrometer dimensions and applied input signals. The existing model demonstrates the possibility of using a *QMS* to identify the low mass isotopes of hydrogen and helium with an improved resolution and sensitivity. The model has been upgraded, since the present QMS2-Ion model does not support the calculation of ionic current of the gas molecules. An ion source model has been developed which supports the calculation of ionic currents for different gas components. This new approach includes pressure dependence in the ion source to allow better prediction of instrument performance. The predicted results are compared with the experimental results obtained from a commercial *QMS* residual gas analyzer. This work also demonstrates the capability of the portable *QMS* system developed to reveal *Helicobacter pylori* infection using a non-invasive carbon-13 urea breath test. This work was conducted with the help of the Royal Liverpool University Hospital and provides accurate diagnosis within 30 minutes.

Contents

List of Figures

List of Tables

Acknowledgement

I sincerely thank **Dr. Stephen Taylor**, Head of Mass Spectrometry Group, Department of Electrical Engineering and Electronics, The University of Liverpool, my revered supervisor, for his invaluable guidance, advice, constructive criticism and encouragement during the course of this work and in all my endeavours in life. It has been a great privilege to work under him. The freedom of expression that he gave, his practical approach to problems and the confidence he had on me to interact have made me to complete this report successfully.

I would like to express my special gratitude to my colleagues, **Dr. Boris Brkic, Mrs. Farnoush Salarzaei,** and **Mr. Sarfaraz Uddin Ahmed Hashmi Syed** for their whole-hearted support and constructive comments, **Mr. Thomas Hogan** and **Dr. Neil France,** for their views, technical assistance and support in learning QMS2 software. I would like to thank my annual oral examiners: **Dr. J R Gibson, Dr. Jason F Ralph, Dr. John Y Goulermas, Dr. David Bakewell, Dr. John S Marsland,** and **Dr. Jonathan H Batey** (Consultant in mass spectrometry, ion optics and vacuum technology) for sparing their valuable time, interest, insightful questions and helpful comments.

I wish to place my grateful thanks to my mentor **Dr. V. Ganesan,** Professor Emeritus, Department of Mechanical Engineering, Internal Combustion Laboratory, Indian Institute of Technology Madras, Chennai, India for his love, encouragement and guidance throughout my pursuits.

Acronyms

APCI	atmospheric pressure chemical ionisation
BEB	Binary encounter Bethe
BED	Binary encounter dipole
CE	capillary electrophoresis
CI	chemical ionisation
DART	direct analysis in real time
DC	direct current
DIOS	desorption/ionisation on silicon
EI	electron impact
ESI	electrospray ionisation
FAB	fast atom bombardment
FD	field desorption
FT	Fourier transform
GC	gas chromatography
GUI	graphical user interface
HPLC	high pressure liquid chromatography
H.pylori	*Helicobacter pylori*
IARC	International Agency for Research on Cancer
ICR	ion cyclotron resonance
IT	ion trap
M	neutral analyte

MALDI   matrix-assisted laser desorption ionisation

MEMS   microengineered mechanical system

MS   mass spectrometry

MS/MS   tandem mass spectrometry

QIT   quadrupole ion trap

QMF   quadrupole mass filter

QMS   quadrupole mass spectrometer

RF   radiofrequency

RGA   residual gas analysis

SIMS   secondary ion mass spectrometry

TOF   time-of-flight

UBT   urea breath test

^{13}C carbon-13

^{14}C carbon-14

Notation

These are terms and notation used throughout this work.

Standard International (SI) Units

ampere	A
candela	cd
coulomb	C
gauss	G
hertz	Hz
joule	J
kelvin	K
kilogram	kg
meter	m
mole	mol
newton	N
second	s
tesla	T
watt	W

Fundamental Physical Constants [78]

Quantity	Symbol	Value	Units
Atomic mass unit, dalton	u, Da	1.6605402	10^{-27} kg
Avogadro constant	N_A	6.0221367	10^{23} mol^{-1}

Bohr radius	a_0	0.5292	Å
Boltzmann constant	k	1.380658	10^{-23} J K^{-1}
Electron mass	m_e	9.1093897	10^{-31} kg
Electron volt	eV	23.06054	kcal mol^{-1}
Elementary charge	e	1.60217733	10^{-19} C
Molar gas constant	R	8.314510	J mol^{-1} K^{-1}
Neutron mass	m_n	1.6749286	10^{-27} kg
Planck constant	h	6.6260755	10^{-34} J s
Proton mass	m_p	1.6726231	10^{-27} kg
Rydberg energy	R	13.61	eV

List of Symbols

Quantity	Symbol	Units
Accelerating voltage	V_i	V
Acceleration	a_n	m/s^2
Angular frequency	ω	Hz
Average kinetic energy	U_i	eV
BEB total ionisation cross section	σ_{BEB}	Å^2
Binding energy	B	eV
Charge density	ρ	C/m^3
Circular trajectory characteristic value	r	–
Density of molecules in ionisation chamber	n_0	m^{-3}
Diameter of final aperture	d_a	m
Distance	d	m
Effective electron path length	S_l	m
Electric field	E_f	V/m
Electric field potential	ϕ	V
Electron density	n_e	m^{-3}

Electron (emission) current	i_e	A
Energy	E_n	J
Energy transfer	E	J
Field radius	r_0	m
Filament current	I	A
Filament length	L_f	mm
Force applied on the ion	F	N
Frequency	f	Hz
Incident electron kinetic energy	T	eV
Ion charge	q_i	C
Ion extraction efficiency	β	–
Ionic current	i^+	A
Ionisation cross section	Q_i	$Å^2$
Ion velocity	v	V
Kinetic energy of an ion	E_k	eV
Length of the QMF	l	mm
Magnetic field	B	G
Magnetic field force	F_m	N
Magnetic field strength	H	G
Mass of the ion	m	kg
Material density	ρ_m	(g/m^3)
Maximum possible electron path length	L_{max}	mm
Momentum	p	kg m/s
Nominal energy	E_n	eV
Number of cycles	N_c	–
Number of elementary charge on the ion	z	–
Number of turns	N_t	–
Occupation number	N	–

Particle kinetic energy	E_p	eV
Polar angle	θ	degree
Radius of sphere	R	mm
Reduced mass	μ	kg
Relative speed	s	m/s
RF sinusoidal voltage	V	V
Scaled time	τ	s
Scattered electron kinetic energy	W	eV
Source potential	V_s	V
Stopping cross section	σ_{stop}	$\mathring{A}^2$
Time	t	s
Time independent voltage	U	V
Time varying position independent factor	E_0	eV
Total cross section	σ_t	$\mathring{A}^2$
Total ionisation cross section	σ_i	$\mathring{A}^2$
Transition energy	E_t	eV
Turn density	n	–
Constants	$\lambda, \sigma, \gamma, k, b$	–

Chapter 1

INTRODUCTION

In modern day living, environmental pollution is a major problem. Therefore, monitoring devices need to be developed in order to understand and monitor pollution effects. Monitoring of nuclear facilities has become of paramount importance because of the health hazard they can pose. Mass spectrometry (*MS*) is an analytical technique that identifies the sample on the basis of mass-to-charge ratio of charged particles. This in turn can help in monitoring nuclear facilities and residual gases for e.g medical applications. Furthermore *MS* can also detect and monitor environmental pollution.

MS has the potential to provide accurate mass measurements from low molecular weight compounds (gases) to large macromolecules. Although mass-spectroscopic techniques have been used to study free ions formed in electric discharges and flames, and even ions existing in the upper atmosphere, it is more commonly desired to examine neutral molecules. These neutral molecules are formed into gaseous ions in an ion source. Ionic current generated in an ion source is pressure-dependent and also depends on the ionisation cross-section of the atoms/molecules. Figure 1.1 shows the typical ionisation cross-section as a function of the electron energy for different gases [92]. These ions are then introduced into an analyzer where they are separated into the appropriate mass-charge groups by the application of an electric or a magnetic field or a combination of the two. The measured property of the ionised species can be

1
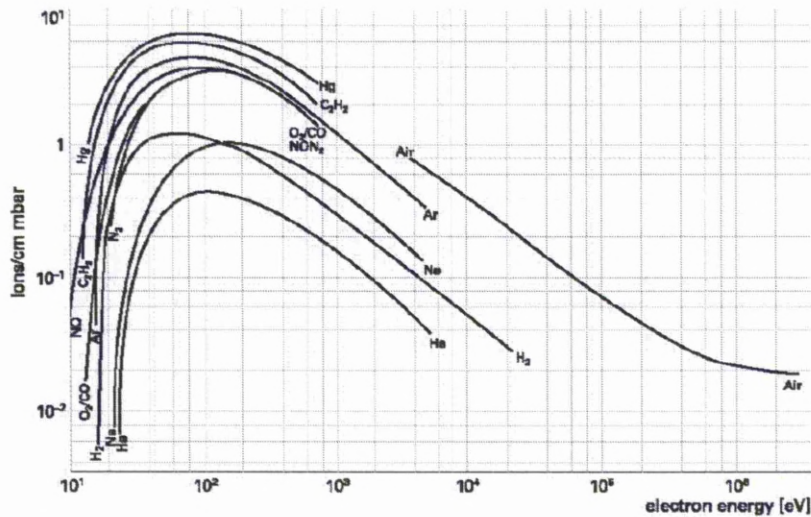
Figure 1.1: Ionisation cross-section as a function of the electron energy

used to study the mass of the sample induced with very high precision.

In applications like chemical, biological and environmental monitoring, a combination of instrumental attributes is required such as speed, sensitivity, wide linear dynamic range, small sample quantity, low detection limits, and capability of on-line analysis in conjunction with separation techniques. Nowadays mass spectrometers are used in physics, chemistry, biology, vacuum process monitoring, medical science and environmental science.

1.1 Key factors influencing a quadrupole mass spectrometer system

The discovery of an alternative method of mass spectrometry that could eliminate the use of magnetic fields in the early 1950s allowed the development of the quadrupole mass spectrometer (QMS) in 1958. The original work was done at the University of Bonn [89] in Germany.

The performance of a QMS system does not only depend on the higher transmission

of a filter, a higher sensitivity of the ion source, or higher detection efficiency. Also relevant are the mass resolution, detection and dynamic range, stability, reproducibility, accuracy and measurement speed. The overall response of any analytical system for a certain analyte when run under well-defined operating conditions is defined by the term sensitivity. In *QMS*, sensitivity is reported as the ionic charge of a specified mass-to-charge ratio (m/z) reaching the detector per unit mass of analyte considered. For gaseous analytes, it can be defined as the ratio of ionic current to analyte partial pressure [44]. Quantities like high transmission of the mass filter, high sensitivity of the ion source, and high detection efficiency contributes to the sensitivity. However, the total sensitivity of a *QMS* system also depends on the instrument resolution setting and the gaseous component under study.

The use of high resolution *QMS* system is of vital importance in certain process control monitoring systems especially if two gaseous components have to be detected which occur at similar mass numbers (e.g overlapping peaks of CO_2^+ and N_2^+).

A mass spectrometer is usually operated at unit resolution, i.e. all peaks are of equal width (one amu) over the whole mass range and 10% valley between two neighbouring peaks of equal heights. Usually this setting is used for *RGA* applications. At unit resolution, the resolution increases with increasing mass number. Sometimes the full width at half maximum is specified for mass resolution. Figure 1.2 shows the mass separation for different peak shapes with the same peak-width at half maximum.

The mass range, and the resolution are dependent on the length and diameter of the rods, the maximum supply voltage to the rods, the rf supply frequency and the ion injection energy [20]. Figure 1.3 shows the relationship of mass range and resolution to the fundamental instrument parameters.

The mass limit determines the highest value of the m/z ratio that can be measured. It is expressed in thomson, or in atomic mass units (u) for an ion carrying an elementary charge. i.e. $z = 1$. The transmission is the ratio between the number of ions reaching the detector and the number of ions produced in the source. The resolution is the ability
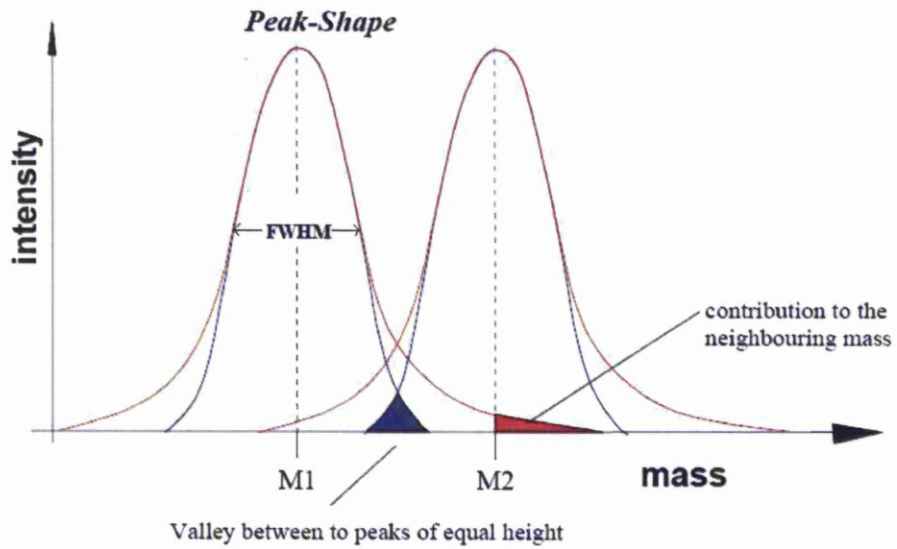
Figure 1.2: Mass separation at different peak shapes with the same peak-width at half maximum
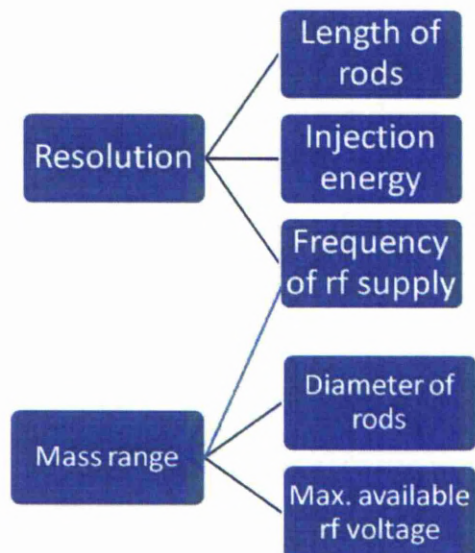
Figure 1.3: Inter-relationship between mass range and resolution of the fundamental instrument parameters
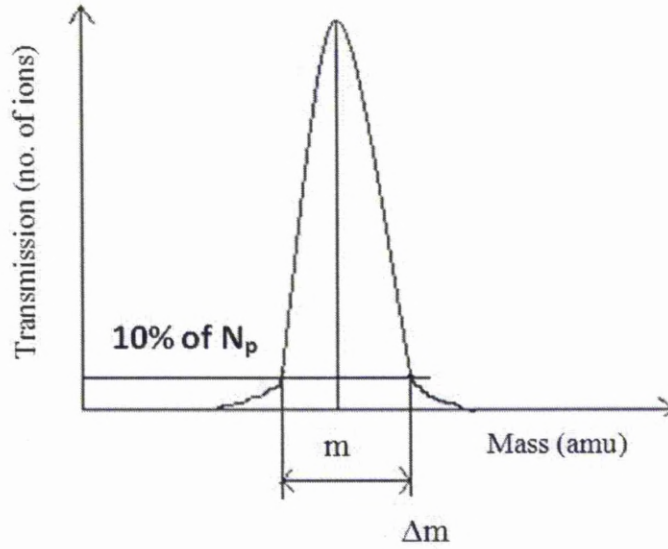
Figure 1.4: Model of mass spectrum

to yield distinct signals for two ions which have a mass difference. Figure 1.4 shows the model of a mass spectrum. Where N_p is the peak height, m is the ion mass, and $\triangle m$ is the mass-dispersion.

The finite length of the quadrupole electrodes limits the time spent by the ions in the focussing field and hence limits the resolution. It is very well established that the number of cycles of RF field to which the ions are exposed governs the resolution limit and the relationship between them is given by

$$\frac{m}{\triangle m} = \frac{1}{K}N_c^{n_s} \tag{1.1}$$

where N_c is the number of cycles, $\triangle m$ is the width of the peak at mass m, n_s is a constant usually around 2, and K another constant usually in the range of $6-20$ [20].

The number of RF cycles experienced by an ion can be defined by the following equation:

$$N_c = \frac{lf}{\sqrt{\frac{2eV_i}{m}}} \qquad (1.2)$$

Where N_c is the number of *RF* cycles experienced by an ion of mass m, l is length of the *QMF* in metres, f is frequency of *RF* excitation in MHz, e electron charge in coulombs, V_i is accelerating voltage in volts, and m is mass of ion in kg.

From the above equation, it is very clear that the number of cycles experienced by the ion is directly proportional to the quadrupole mass filter length, drive frequency, and the square root of the mass, and inversely proportional to the square root of the ion energy.

1.2   A brief description of *QMS* simulation software

Software development plays an important role in QMS design in order to achieve the users requirement at minimal cost. A simulation software suite has been developed in the .Net environment using visual C++ to study the performance of *QMS* for both hyperbolic and circular rod quadrupole mass filter (*QMF*) at University of Liverpool over the last 14 years. Major contributors include: F. M. Ma, J. J. Tunstall, J. R. Gibson, and T. Hogan. The computer code mainly consists of two programs viz. QMS2-Hyperbolic/QMS2-Field and QMS2-Ion.

The QMS2 model consists of a graphical user interface (*GUI*) with an ion trajectory computing engine to calculate individual ion trajectories. The solution method for the Mathieu equation [20] in the x- and y- coordinates is carried out by means of numerical integration using a fourth order Runge-Kutta algorithm. The ion entry conditions into the *QMF* are also taken into account. *QMS2* Ion program generates a large number of individual ion start conditions and stores them in a binary file, which is read by the *QMS2*-Hyperbolic/*QMS2*-Field program. Each ion that enters will have the value of ion initial positions in both the x- and y- axis at the entry to the *QMF*, ion initial

phase with respect to the *RF* drive and ion initial velocity along *x*-, *y*- and *z*- axes. While executing the program, a file is also generated which has the information of ion energy, ion source radius, ion energy spread, ion beam spread and filename prefix saved as a text file. A data file with the information of ion energy, ion source radius, ion energy spread and ion beam spread is also generated in text format and associated files are generated and stored in a subfolder, Ion-Files, for the use of ion source program. The various files generated are also stored in sub folder Ion-Files. Finally, MatLab was used to postprocess the data and for the generation of the graphical results shown in this thesis.

1.3   Scope of the work presented in this thesis

The main aim of this work was to develop a more complete simulation model which includes the effect of pressure to allow better prediction of QMS instrument performance. The existing software model has been upgraded, since the present QMS2-Ion model described in the previous section does not support the calculation of ionic current in the source for different operating conditions. This work also includes the simulation of hyperbolic shaped QMF operated in Zone 3 of the Mathieu stability diagram using QMS2-Hyperbolic to study the performance of QMS for resolving the identification of low mass isotopes. An ion source model, including pressure dependency which will support the calculation of ionic current of individual gas components, has been developed using visual C++ . The predicted results are compared with the experimental results obtained from a commercial QMS residual gas analyzer. This approach allows better prediction of instrument performance which is especially important in miniature and microengineered QMS instruments, important for portable applications. From the application point of view, this work shows the use of a portable QMS for detecting *Helicobacterpylori* (*H.pylori*) infection. *H.pylori* are a type of bacteria believed to play a vital role in peptic ulcer disease. The organism was found to be present more

frequently in idiopathic peptic ulcer disease. *H.pylori* has been associated with duodenal ulcers which may progress to chronic gastric cancer. The World Health Organization's International Agency for Research on Cancer (*IARC*) classified the bacterium as a grade 1 carcinogen on par with hepatitis B virus [107] [76]. Reported in the thesis is a non-invasive carbon-13 urea breath test that can detect *H.pylori* infection using a portable *QMS* system.

1.4   Outline of the thesis

Chapter two gives a good historical survey of the advances made in the field of mass spectrometry since the discovery of parabola spectrograph by J.J. Thomson. This chapter also presents work undertaken by different researchers on numerical simulation techniques for *QMS* simulation to calculate the instrument performance due to imperfection errors in assembling the electrode structure and the effects of displacing the electrodes. Simulation tools are also used to evaluate ion entrance condition by calculating the ion trajectories using the matrix method, to study the effects of *RF* frequency, phase, and magnitude on *QMF* performance, and to investigate the mass spectra generated by both hyperbolic and circular electrode shapes.

Chapter three gives an overview of experimental *QMS* and the description of individual *QMS* components. It also explains the different ionisation processes taking place in the ion source, and the different analyzers and detectors used for the identification of samples under study. This chapter presents a detailed explanation of *QMS* and its theory supporting their operation as a mass detector.

Chapter four gives the description of *QMS2* software developed. Chapter five provides the details of the *QMS* for the identification of low mass isotopes. The qualitative and quantitative identification of low mass isotopes in the mass range 1 - 6 amu poses certain difficulties when attempting to achieve the required resolution with an instrument suitable for deployment within a process environment. Certain adjacent species

present in the process sample (HT and D_2) require a resolution greater than 930 to achieve an accurate measurement. This chapter uses QMS simulation techniques to determine the level of performance required which is not achievable using present day commercially available instruments.

Chapter six is describes an extension to the QMS computer code to allow simulation of QMS spectra over the pressure range from 10^{-6} to 10^{-4} Torr. An important contribution of this work is the development of a novel procedure to include pressure dependence of the ion source to allow better prediction of instrument performance. Electron-impact total ionisation cross-sections in the ionic current expression are calculated using the Binary-Encounter-Bethe (BEB) theory for argon gas. The predicted results are compared with the experimental results obtained from a commercial QMS residual gas analyzer.

Chapter seven is an application study describing how a portable QMS system has been used to detect the $H.pylori$ infection using the non-invasive carbon-13 Urea breath test conducted with the help of Royal Liverpool University Hospital.

Chapter eight presents the conclusions and the future work to be done.

Chapter 2

LITERATURE REVIEW

The analysis [24] of positive rays through the parabolic method by J.J. Thomson [110] opened the way to the mass spectrometry field. Thomson constructed the first mass spectrometer and called it a parabola spectrograph, in which the ions were separated by their different parabolic trajectories in electromagnetic fields and detection occurred by the electrons striking a fluorescent screen or photographic plate. Figures 2.1 and 2.2 show the deflection in the flow of electrons with and without electric field applied.

Figure 2.1: Flow of electrons when no electric field was applied

Figure 2.2: Electron deflection once the electric field was turned on

Thomson's book [110] very well describes the early work of Goldstein, Wein, and others. Aston's "Isotopes" [12], published in 1922 excellently describes the prototypes of early mass spectrometry and its application to isotopic analysis. The mass spectrometer has been the most successful mass analysis technique and provides high resolution. Aston's later books, "Mass Spectra and Isotopes" published in 1933 and 1942 (second edition) gives an admirable account of the rapid modern developments in mass spectrometry field. "Electron impact Phenomena" by Field and Franklin [38], was the first book to give a detailed study of the ionisation of molecules and dissociation of molecular ions by modern mass-spectrometric methods. Its excellent comprehensive explanation of chemical physics for workers in the field has resulted in this book becoming a classic and constant reference text. Since mass spectrometer applications in chemistry were becoming very important in the mid-1950s, subsequent work concentrated on improving instrument design and achieving higher resolutions.

The early work of Dempster's [26] 180° deflection magnetic spectrometer led the way initially. Afterwards the development of mass spectrometers with 90° and 60° deflections by Nier became more wide spread [87], [86]. Industrial applications encouraged mass rapid commercialization resulting in the development of a few standard types of magnetic spectrometers.

Mass spectrometry is a microanalytical technique that can obtain characteristic information of analytes. In the process, some form of energy is transferred to the analyte molecules to effect ionisation. In the electron ionisation technique, the molecular ions of the analyte are converted into a variety of lower mass fragment ions. The resulting fragmentation pattern together with residual molecular ions results in mass spectrum which can be used as a "finger print" to characterize the analyte [46].

In this way the application of mass spectrometers became wide spread in the study of kinetic reactions, biological analysis, biochemistry [29] [100] [102], explosives, and other industrial applications, particularly in the petroleum industry. There are also medical applications like the detection of *Helicobacterpylori* [31] [84] [93] [116] in

11

the urea breath test. Increased applications have led to further demands in instrument design and performance.

In practice, achieving stable and spatial uniform magnetic fields is very difficult with permanent magnets which would lead to degradation of the mass analyser and drifts in the calibration of the instrument. Moreover, the presence of a stray magnetic field can effect other instruments used in conjunction with the mass spectrometer. In the early 1950's it was recognized that the quadrupole electric fields could be used to eliminate the use of magnetic fields and hence the name quadrupole mass spectrometer (QMS). Since the early work conducted by Paul's group at the University of Bonn in the development of quadrupole mass filter (QMF), much research has been performed on the QMS for a variety of in situ range of applications. QMS have impressive attributes and are easier to use than magnetic sector mass spectrometers [21]. The characteristics include classical mass spectra, good reproducibility, a linear mass scale, a trade off between the sensitivity and resolution by electronic adjustment, absence of a bulky magnet resulting in light weight, relatively simple mechanical construction and low cost vacuum systems. These characteristics have ensured a wide range of applications. Using high sensitivity electron multipliers, QMS can measure partial pressures down to 10^{-14} Torr, useful for residual gas analysis.

Before the 1950s magnetic deflection mass spectrometer instruments were widely used, which consisted of static analyzers where the magnetic and electric field remained constant during the passage of an ion. Emerging on-going demands urged the development of mass spectrometer with dynamic mass analyzers. In a dynamic analyzer, the ion separation is based on the time dependence of one of the system parameters. Dynamic type mass spectrometers [95] include ion cyclotron resonance mass spectrometers ($ICR - MS$), a radiofrequency quadrupole mass filter ($RF - QMF$) and RF ion trap mass spectrometers ($ITMS$). Based on the stability and/or dynamic resonance of the characteristic oscillation of ions in electric or magnetic field with application of time-varying fields, a specific ion mass can be selected. $RF - QMF$ and

ITMS are very attractive dynamic mass spectrometers since they can be made compact and at relatively low cost.

Mass analyzers such as magnetic analyzers, the time of flight mass analyzer, the ion cyclotron resonance instruments or the ion trap (explained in Chapter 3, Section 3.3.4) allow the simultaneous transmission of all ions. The time-of-flight mass analyzer operates in a pulse mode that requires the ions to be produced in bundles, and is well suited for pulsed laser sources. The *QMF*, the monopole and the three-dimensional ion trap are the three principle types of mass analyzers which utilize electro-dynamic quadrupole fields. The main function of the mass analyzer is to separate ions formed in the mass spectrometer ionisation source according to their mass-to-charge (m/z) ratios.

The monopole utilizes both filtering action and dynamic focussing to achieve the final mass separation. In the quadrupole ion trap (*QIT*), ions with different masses are present together inside the trap and are expelled according to their masses to obtain the spectrum. The ion trap [73] is a high performance mass spectrometer and is used as a gas chromatography/mass spectrometry (*GC/MS*) analyzer. It is also used as a storage device for the confinement of gaseous ions and their number are measured after a suitable storage period. *ICR − MS* using Fourier transform techniques that obtain the whole spectrum at once, rather than just one frequency at a time, show impressive possibilities at high masses and high resolutions [67]. Mass spectra resulting from the decomposition of a selected ion can be obtained using tandem mass spectrometry (*MS/MS*). In cyclotron or ion trap instruments, the analysis is based on the time-dependent decomposition of a selected ion species.

In the case of the magnetic sector mass spectrometer, multiply-charged ions, generated by electrospray ionisation, are detected at m/z-values much lower than the molecular weight of the large 'parent' molecules thereby removing the mass range limitation which restricts the analysis of single charged compounds. The promising characteristics of *QMS* led to an interest of miniaturization of the instrument through the use of microengineered mechanical system (*MEMS*) techniques. Miniaturization reduces the
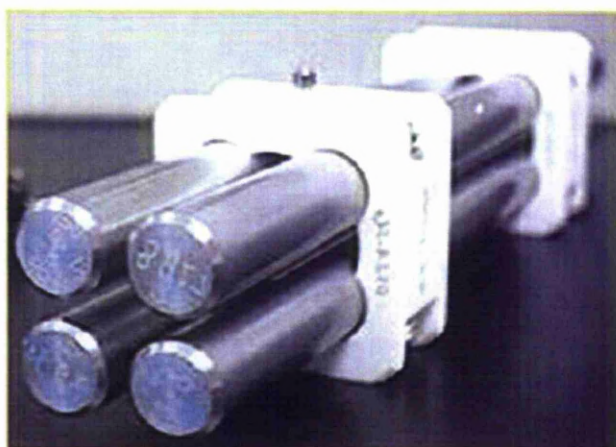
Figure 2.3: Conventional quadrupole mass filter with circular cross-section electrodes

overall size without sacrificing the performance. The reduction in mass filter length means a reduction in the ion path length and hence a reduction in the number of collisions which allows operation at higher pressure. Miniature *QMS* allow reductions in operating voltage and power and can be used used in a range of inaccessible environments [14] [108].

A typical *QMS* consists of a mass analyzer, which has four longitudinal parallel electrodes with an angular spacing of 90°. The ideal electrode surface is hyperbolic. However, in practice circular electrodes (Figure 2.3) are usually used because of the difficulty in machining electrodes with the hyperbolic cross-sections [20]. The field in this case closely approximates to the ideal hyperbolic field provided that the electron diameter and separation are correctly chosen. However even a small positioning error or approximation in the shape of electrodes results in aberrations which reflect on instrument performance. The performance of a mass spectrometer, including mass resolution, mass accuracy and sensitivity is determined by several factors.

Several works have been undertaken to examine *QMS* performance. In early studies of Dawson and Whetten [22] [23], numerical computer simulation techniques were employed to integrate the Mathieu equation and calculate ion trajectories and also to compute a single ion trajectories in the *QIT* mass spectrometer. A detailed study by

Richards et al [98] employed matrix methods to calculate the state transition matrix from the ion's initial conditions to obtain the position and velocity of an ion at a point to the case of a quadrupole analyser driven by a square wave [74]. The calculation of ion trajectories by phase space dynamics using the matrix method to evaluate ion entrance condition has been discussed by Baril et al [15]. All their works were based on ion trajectory analysis in the two dimensional quadrupole field in the plane perpendicular to the four rod electrodes.

As an extension of the above works many numerical simulation techniques have been performed to study the theoretical performance characteristics of the QMS. Some of them include the effects of RF frequency, phase, and magnitude on QMF performance [71]; the computer simulation of a quadrupole mass analyzer considering the effects of initial ion energy and quadrupole rod length on percentage ion transmission through the mass filter [117]; the study of transmission efficiency for a finite length QMS under a range of operating conditions for different design dimensions and to examine the effects of ion energies and entrance aperture for the mass filter for both sinusoidal RF excitation and RF with added harmonics [115]; and the study of ion trajectories using QMS in which a static magnetic field was applied to the body of mass filter [104].

Later research works continued on the detailed investigation of mass spectra using computer simulation techniques for both hyperbolic and circular rods [40], [42]. The field generated from the circular rods approximately represents the quadrupole field plus the sum of a number of higher-order fields which is termed the multipole field [33]. The relative magnitude of the individual components of the multipole field can be controlled by the ratio of the rod radius r to the distance from the center of the quadrupole to a rod, field radius (r_0). Subsequent research works were studied to achieve the best performance QMS by altering the value of r/r_0. Later theoretical research work suggested that the ratio of 1.148 [20] results in the dodecapole (A_6) multipole field coefficient equating to zero produced optimum QMS behaviour rather

than 1.16 [25]. This first higher order harmonic A_6 is determined by the position of the rods and their diameter. Computer simulation has shown that when operating in the first stable region (explained in Chapter 3, Section 3.5), circular rods with $r/r_0 = 1.148$ suffer from increased peak width, lower transmission and low mass tailing than hyperbolic rods [42]. More recently, numerical computer simulations operated in the first stable region (Zone 1) refined r/r_0 ratio from 1.125 to 1.130 [42] [43]. At this ratio, the optimum performance was achieved corresponding to a nonzero value for the dodecapole (A_6) coefficient. Later this value is found to be almost the same for operation in Zone 3 (explained in Chapter 5, Section 5.2) also [53] [52].

The best QMF operational performance is obtained not only with the optimum path stability, but also on the exact focussing of the ion beam from a wide variety of ion sources [20]. More recent work has also shown that this is true when the values of r/r_0 are between 1.125 and 1.127, which give a better approximation to hyperbolic electrodes compared to the quadrupole field at $r/r_0 = 1.148$ [18] [33] [43]. This optimum performance is achieved because the A_6 and A_{10} multipole coefficients are of similar magnitude and opposite sign, thereby partially canceling out each other. Using the simulation programme QMS2, with 60 cycles of RF, a comparison of resolution at 10% peak height and transmission through QMS using filters of different geometry have been studied. Resolution is further improved when QMS are operated in Zone 3 [53].

Chapter 3

MASS SPECTROMETER

A mass spectrometer has three essential fundamental parts, namely the ionisation source, the analyser, and the detector. These are maintained under high vacuum to allow the ions travelling from one end of the instrument to the other without any hindrance from air molecules. Figure 3.1 shows the schematic representation of mass spectrometric analyser.

3.1 Sample introduction

For an ionisation process to take place in the ion source, the sample has to be introduced into the ionisation chamber. Gaseous samples can be inserted directly into the ionisation source, however in many studies, samples are introduced using chromatography prior to ionisation. Chromatography is a chemical technique for the separation
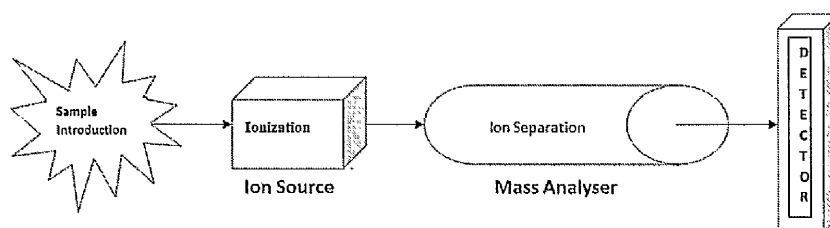
Figure 3.1: Schematic diagram of mass spectrometric analyser

of chemical mixtures. It includes high pressure liquid chromatography (*HPLC*), gas chromatography (*GC*), and capillary electrophoresis (*CE*). In a mass spectrometer, the ion source is coupled directly to chromatography system which causes sample separation into a series of components which are then analyzed by the mass spectrometer for individual component analysis.

3.2 Ionisation methods

In mass spectrometer, the ion source is the initial part that ionizes the analyzed samples. A variety of ion sources have been developed which cause the formation of positive and negative ions and each has its own advantages and disadvantages [11]. No one ion source is ideally suited to all applications, and the choice of source for a particular application depends on the nature of the sample and the type of information desired.

An ideal ion source should possess the following features [80].

1. An accurate measurement of the separated beams can be possible with the ion beam of sufficient intensity; a total ion-beam intensity of 10^{-10} A is desirable. The limit of detection with electronic amplifiers is about 10^{-15} A, and with an electron multiplier, 10^{-19} A.

2. The ion beam should be stable.

3. The highest resolving power in a single-focussing instrument with low energy spread of the ion beam.

4. The source should be designed to produce the minimum intensity of background ions. This can be achieved by using a high pumping speed in the source region, and the use of pure materials that have less outgassing effect.

5. No cross contamination or "memory effects" between successive samples.

6. Mass discrimination should be negligible.

18

The ion sources produces ions mainly by ionising a neutral molecule through electron ejection, electron capture, protonation, deprotonation, the transfer of a charged species from a condensed phase to the gas phase. In the ionisation process the internal energy transferred and the photochemical properties of the analyte that can be ionized are considered. Sample ionisation mechanism are listed:

- Protonation: $M + H^+ \rightarrow MH^+$

- Cationisation: $M + \mathrm{Cat}^+ \rightarrow M\,\mathrm{Cat}^+$

- Deprotonation: $MH \rightarrow M^- + H^+$

- Electron ejection: $M \rightarrow M^+ + e^-$

- Electron capture: $M + e^- \rightarrow M^-$

Electron ionisation and chemical ionisation (*CI*) are used to compounds that are sufficiently volatile and thermally stable and hence are suitable for gas-phase ionisation. In *CI*, the ionisation of analyte is achieved by chemical ion molecule reactions during collisions in the source. Electrospray Ionisation (*ESI*) and Matrix-Assisted Laserdesorption Ionisation (*MALDI*) are used for many application involving bio-organic compounds due to their softer character and only produce molecular species. Other types of ionisation technique include glow discharge, field desorption (*FD*), desorption/ionisation on silicon (*DIOS*), thermospray, fast atom bombardment (*FAB*), secondary ion mass spectrometry (*SIMS*), atmospheric pressure chemical ionisation (*APCI*), direct analysis in real time (*DART*), spark ionisation and thermal ionisation [19].

3.2.1 Electron ionisation

The attributes of the electron impact ion source make it the most popular choice for many mass spectrometry instruments. The characteristics that allow widespread usage are reproducible mass spectra and fragmentation of ions, which can provide the

structural information of analyte molecules. In an electron ionisation ion source, as shown in Figure 3.2, ionic currents are generated by using electron ionisation process, which enables the conversion of electrically neutral molecules into electrically charged molecules. In electron ionisation, electrons are generated through thermionic emission [99] through an electrically heated coil filament to a temperature at which it emits free electrons. The emitted electrons are accelerated with 70eV (normally used in all RGA applications) so that they form an electron beam between the filament and the anode trap. Analyte sample molecules are introduced to the ion source in a perpendicular direction of the e-beam. Upon interaction between the analyte sample and the e-beam, the neutral molecules ionize to radical cations. The energy generated during the interaction of the analyte molecules with electrons from a hot filament is used for effecting the ionisation process [103], [35]. The generated radical cations are directed towards the mass analyzer by a repeller electrode. The ionisation chamber is maintained at a low pressure in order to minimize ion/ molecule collisions. The cleavage reactions during the ionisation process give rise to fragment ions. The entire ionisation process depends on both the electron emission energy and the initial thermal distribution of neutral molecules.

3.2.2 Chemical ionisation

CI is a technique that produces ionized species when gaseous molecules interact with ions. This technique yields a mass spectrum with less fragmentation compared to electron ionisation in which the molecular species is easily recognized [83]. *CI* involves the transfer of an electron, proton, or other charged species between the reactants namely the neutral analyte *M* and ions from the reagent gas [114]. Figure 3.3 shows schematic representation of *CI* ion source.

The mechanism of *CI* to form ions from a neutral analyte *M* is listed below [47].

- Proton transfer: $M + [BH]^+ \rightarrow [M+H]^+ + B$
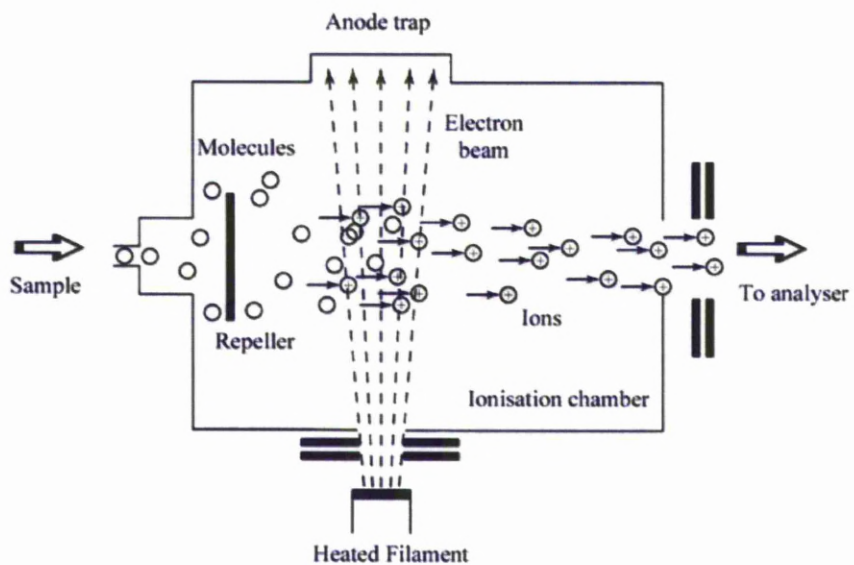
Figure 3.2: Electron ionisation
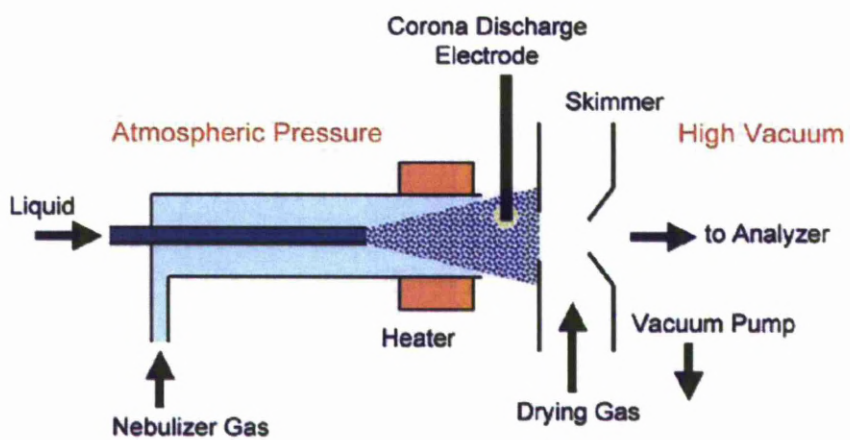
Figure 3.3: Chemical ionisation

- Electrophilic addition: $M + X^+ \rightarrow [M + X]^+$

- Anion abstraction: $M + X^+ \rightarrow [M - H]^+ + HX$

- Charge exchange: $M + X^\pm \rightarrow M^\pm + X$

The proton transfer reaction results in the yield of protonated analyte molecule, $[M + H]^+$. In electrophilic addition, the complete reagent ions get attached to the analyte molecule. Anion abstraction yield $[M - H]^+$ ions rather than $[M + H]^+$ ions. Charge exchange yields low internal energy radical ions. When CI results in a positive ion, the term positive-ion CI should be used. Similarly if it results in a negative ion then the term negative-ion CI should be used [114].

3.3 Mass analyzers

Once the ions have been produced in the ion source, they need to be separated according to their masses. Mass analyzers have the ability to separate the ions formed in the ionisation source according to their mass-to-charge (m/z) ratios. This separation is achieved by the application of either electric or a magnetic field or a combination of the two.

The Lorentz force and Newton's second law of motion are the two laws that govern the charged particle dynamics in both electric and magnetic fields in vacuum. Equations 3.1 and 3.2 show Lorentz force law and Newton's law of motion.

$$F \;=\; q_i(E + v \times B) \tag{3.1}$$

$$F \;=\; ma_n \tag{3.2}$$

where F is the force applied on the ion, m is the mass of the ion, a_n is the acceleration, q_i is the ion charge, E is the electric field, and $v \times B$ is the vector cross product of the ion velocity and the magnetic field.

Equating the expressions of the force applied to the ions results in an equation of motion for charged particles:

$$\frac{m}{q_i} a_n = E + v \times B \tag{3.3}$$

Mass spectrometers determine the particle's motion in terms of mass-to-charge (m/z) ratios, where z is the number of elementary charge (e) on the ion $(z = q_i/e)$.

There are many different types available, of which the most common mass analyzers are listed below :

- Quadrupole

- Magnetic Sector Field

- Electric Sector Field

- Time-Of-Flight (TOF)

- Ion Trap (IT)

- Fourier-Transform Ion Cyclotron Resonance $(FT - ICR)$

Mass analyzers are generally scanning devices that allow successive transmission of ions of different m/z-values with time. The mass analyzers with this property are usually either magnetic sector instruments or quadrupole instruments. Mass analyzers such as dispersive magnetic analyzers, the time-of-flight analyzers, the IT or the ion cyclotron instruments allows the simultaneous transmission of ions.

3.3.1 Sector field mass analyzers

The sector field mass spectrometer is one of the most common types of mass analyzer and uses a magnetic field to affect the charged particle path [27]. Figure 3.4 shows the schematic of a sector field mass spectrometer. As shown in the figure, as ions pass
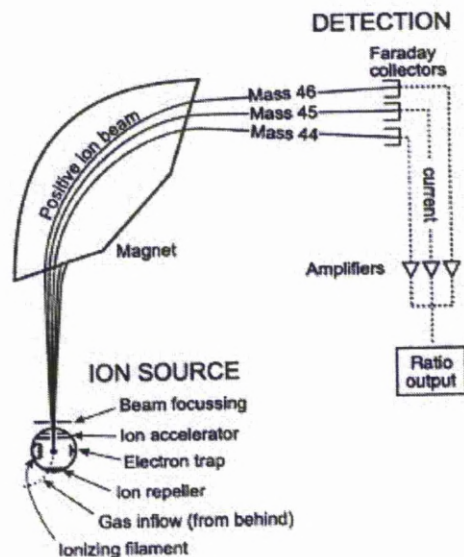
Figure 3.4: Schematic representation of a sector field mass spectrometer

through the mass analyzer, according to their mass-to-charge ratio, the more charged and faster-moving , lighter ions are deflected more.

Consider the kinetic energy of an ion with mass m and charge q_i, accelerated in the source by a potential difference of V_s is given by the following equation.

$$E_k \quad = \quad \frac{mv^2}{2} \quad = \quad q_i V_s \tag{3.4}$$

If the magnetic field applied is perpendicular to the velocity of the ion then the force experienced by the ion is given by:

$$F_m \quad = \quad q_i v B \tag{3.5}$$

where B is the magnetic field.

The ions follow a circular trajectory with a radius r so that the centrifugal force

equilibrates the magnetic force. Equating the equations 3.4 and 3.5 we get

$$q_i v B \;=\; \frac{mv^2}{r} \quad \text{or} \quad mv \;=\; q_i B r \tag{3.6}$$

For every value of B, ions with the same charge and the same momentum (mv) have a circular trajectory with a characteristic r value. Thus, the magnetic analyzer selects the ions according to their momentum. However, taking into account the kinetic energy of the ions at the source outlet leads to

$$\frac{m}{q_i} \;=\; \frac{2V_s}{v^2} \;=\; \frac{2V_s m^2}{q_i^2 r^2 B^2} \;=\; \frac{B^2 r^2}{2V_s} \tag{3.7}$$

In the presence of magnetic field the force experienced by the ions is at right angles both to the direction of motion and to the direction of magnetic field. In the presence of an electrostatic field, the ions have circular trajectories and the velocity is constantly perpendicular to the field.

$$q_i E \;=\; \frac{mv^2}{r} \tag{3.8}$$

where E is the intensity of electric field

An electric sector is not a mass analyzer but rather it separates the ions according to their kinetic energy (energy analyzer).

Figure 3.5 shows a scheme of sector mass spectrometer showing both magnetic and electrostatic sector. The green part of the beam represents ions with higher m/z values that do not pass through the spectrometer.

3.3.2 Quadrupole analyzers

The quadrupole mass analyzer is a "mass filter". Combined DC and RF potentials on the quadrupole rods can be set to pass only a selected mass-to-charge ratio. All other ions do not have a stable trajectory through the quadrupole mass analyzer and will collide with the quadrupole rods, never reaching the detector. (see Section 3.5).
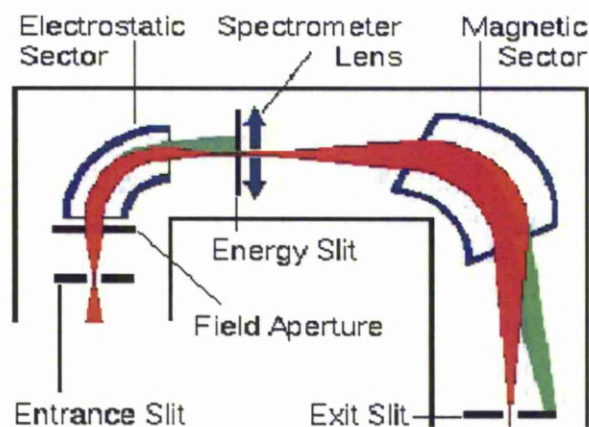
Figure 3.5: Scheme of sector mass spectrometer showing both magnetic and electro-static sectors

Quadrupole mass analyzers act as mass selective filters and have the same principles as that of quadrupole ion traps.

3.3.3 Time-of-flight

In 1946 Stephens described the concept of the linear time of flight (TOF) analyzer. An improved design of a linear TOF mass analyzer was published in 1955 by Wiley and McLaren that later became the first commercial TOF instrument. Due to the development of matrix-assisted laser desorption ionisation $MALDI$, TOF paved the way not only for biological analysis applications but also for synthetic polymer and polymer conjugates. In mass spectrometry, there are number of different ways of performing mass analysis. Some types of instrument measure the deflection of an ionized beam accelerated through a magnetic or electric field to separate ions of different masses. Other types use a high frequency electric field to filter the ion beam. The applied field determines which masses are able to pass through the filter. However, in the case of TOF analyzer, ions formed from the sample atoms, or molecules are identified by measuring their flight time. The electric field applied accelerates the ions through the same potential and the time taken to reach the detector is measured. If the particles all have
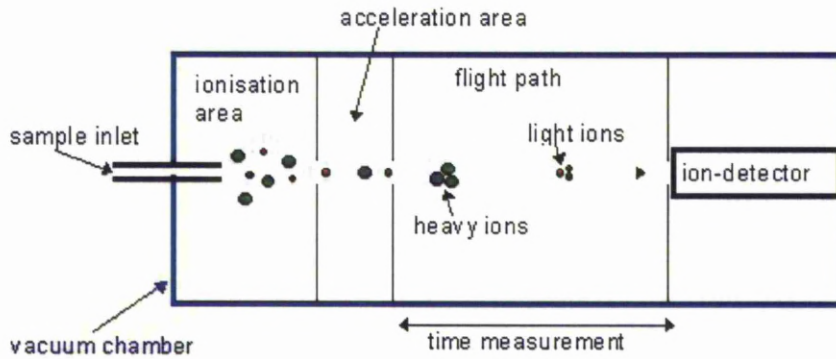
Figure 3.6: Linear time-of-flight mass spectrometer

the same charge, the kinetic energies will be identical, and their velocities will depend only on their masses. The lighter ions reach the detector first [119], [72]. Figure 3.6 shows the scheme of linear time-of-flight mass spectrometer.

Ions are expelled from the source in bundles that are either produced by an intermittent process such as plasma or laser desorption or expelled by a transient application of the required potentials on the source-focussing lenses. They are accelerated by a potential V_s and fly a distance d before reaching the detector.

The kinetic energy of an ion of mass m and charge $q_i = ze$ is given by

$$\frac{mv^2}{2} \quad = \quad q_i V_s \quad = \quad zeV_s \quad = \quad E_k \tag{3.9}$$

The time needed to fly the distance d is given by

$$t \quad = \quad \frac{d}{v} \tag{3.10}$$

Substituting the value of v in the equation 3.10 gives

$$t^2 \quad = \quad \frac{md^2}{z2V_s e} \tag{3.11}$$

From the equation 3.11, the mass-to-charge ratio can be calculated from the measurement of t^2. This equation also show that lower the mass of an ion, faster it will reach the detector.

27

3.3.4 Quadrupole ion trap

The quadrupole ion trap (QIT) mass analyzer was developed by Wolfgang Paul and has been modified to a useful mass spectrometer by Stafford et al [105]. The QIT mass spectrometer is a derivative of quadrupole mass spectrometer (QMS). Both work on the same principle, but in the QIT mass spectrometer the ions are trapped [73]. Figure 3.7 shows a schematic representation of QIT mass spectrometer. Ions are generated and trapped on a three dimensional trajectory. RF potential is ramped along z to expel ions of a given mass.

Ions generated in the ion source enter the trap through an inlet and are trapped in the field. The analyser consist of a parallel array of four rod electrodes mounted in a square configuration. The field within the analyser is created by coupling opposite pairs of rods together and applying RF and direct-current (DC) potentials between the pairs. Ions created within the source are injected through the parallel array, and under the influence of the fields they form complex trajectories. Some of these trajectories are unstable in that they tend toward infinite displacement from the center so that the ions are lost through collision with an electrode. Ions that are successfully transmitted through the analyser are said to possess stable trajectories, and these recorded on the detection system. For a given interelectrode spacing $2r_0$, the path stability of an ion with a particular value of m/z depends on the amplitude of the RF drive potential (V), the magnitude of its frequency, and the ratio of the amplitudes of the RF and DC (U) potentials. When U = 0, a wide band of m/z values is transmitted, and as the value of the ratio U/V is increased, the resolution increases so that at the stability limit only a single value of m/z corresponds to a stable trajectory, resulting in the transmission and collecting of ions of mass-to-charge ratio.

In a linear QIT [101], the difference is that ions are trapped in a two dimensional quadrupole field, instead of a three dimensional quadrupole field.

28
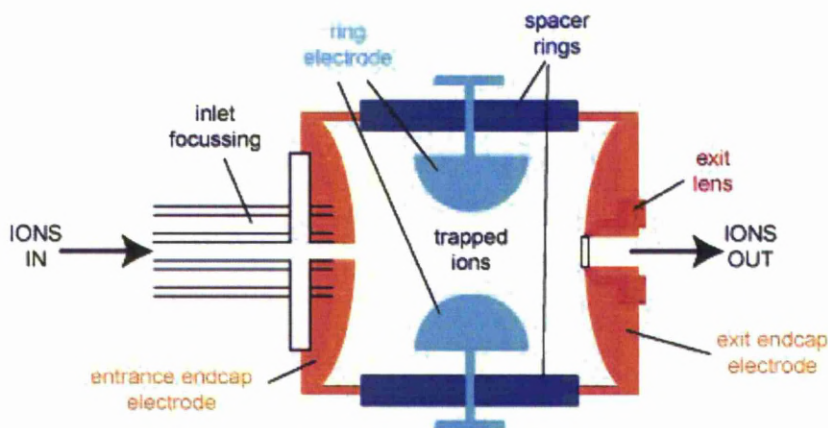
Figure 3.7: Schematic of a quadrupole ion trap mass spectrometer (Paul trap)

3.3.5 Fourier-transform ion cyclotron resonance

Fourier-Transform Ion Cyclotron Resonance mass spectrometry ($FTICR - MS$) is based on the measurement of mass by detecting the image current produced by the cyclotron movement of the charged particles in a magnetic field. The cyclotron frequency directly depends on the m/z ratio of the ions. The movement of ion packets are converted to frequency spectra by means of a Fourier transform, and after calibration each frequency spectrum is converted to a mass spectrum [75].

Ions move in a circular path in a magnetic field. The cyclotron frequency of the ion's circular motion is mass-dependent. By measuring the cyclotron frequency, one can determine an ion's mass. A group of ions of the same mass-to-charge ratio will have the same cyclotron frequency, but they will be moving independently and out-of-phase at roughly thermal energies. If an excitation pulse is applied at the cyclotron frequency, the "resonant" ions will absorb energy and be brought into phase with the excitation pulse. As ions absorb energy,the size of their orbit also increases [54].

The packet of ions passes close to the receiver plates in the *ICR* cell and induces image currents that can be amplified and digitized. The signal induced in the receiver plates depends on the number of ions and their distance from the receiver plates. If sev-

29

eral different masses are present, then one must apply an excitation pulse that contains components at all of the cyclotron frequencies. This is done by using a rapid frequency sweep ("chirp"), an "impulse" excitation, or a tailored waveform. The image currents induced in the receiver plates will contain frequency components from all of the mass-to-charge ratios. The various frequencies and their relative abundances can be extracted mathematically by using a Fourier transform which converts a time-domain signal (the image currents) to a frequency-domain spectrum (the mass spectrum). Figure 3.8 shows Fourier-Transform Ion Cyclotron Resonance instrument.

The cubic *ICR* cell consists of three pairs of parallel plates. The functions of the excitation and receiver plates are apparent from the preceding discussion. A small potential is applied to the trapping plates to keep the ions contained within the *ICR* cell because the magnetic field does not constrain the ion motion along the direction of the applied magnetic field. Beside the cubic cell, many other *ICR* cell designs have been evaluated, and each has its own special characteristics.

Excitation events can be used to increase the kinetic energy of ions, or to eject ions of a given mass-to-charge ratio from the cell by increasing the orbital radius until ions are lost by collisions with the cell plates.

The background pressure of an *FTICR* should be very low to minimize ion-molecule reactions and ion-neutral collisions that damp the coherent ion motion. A variety of external ion source designs have been developed to deal with this problem, and each design has its own performance characteristics.

Most *FTICR* mass spectrometers use superconducting magnets, which provide a relatively stable calibration over a long period of time. Although some mass accuracy can be obtained without internal calibrant, mass accuracy and resolution are inversely proportional to m/z, and the best accurate mass measurements require an internal calibrant. Unlike the quadrupole ion trap, the *FTICR* mass spectrometer is not operated as a scanning device.
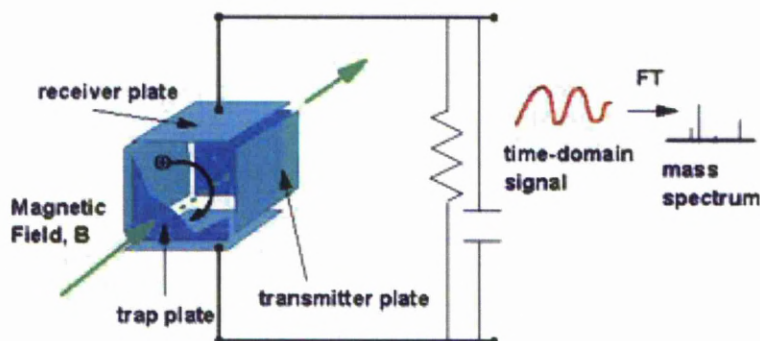
Figure 3.8: Fourier transform ion cyclotron resonance instrument

3.4 Detector

The final part of the mass spectrometer is the detector. The detector records the ion current, amplifies it and the signal is transmitted to the data system which will produce a mass spectrum, a record of ion as a function of mass-to-charge ratios (m/z).

There are many different detectors available to suit the mass analyzer type, of which the most common detectors are listed below.

- The electron multiplier

- The Faraday cup

- The photomultiplier

3.4.1 Electron multiplier

An electron multiplier is used to detect the presence of ion signals emerging from the mass analyzer of a mass spectrometer. The task of the electron multiplier is to detect every ion of the selected mass passed by the mass filter. The basic physical process that allows an electron multiplier to operate is called secondary electron emission.When a charged particle (ion or electron) strikes a surface it causes secondary electrons to be

31
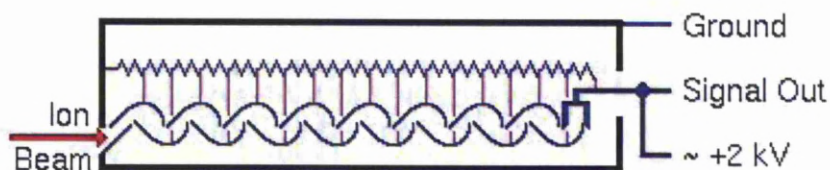
Figure 3.9: Electron multiplier with discrete dynodes

released from atoms in the surface layer. The number of secondary electrons released depends on the type of incident primary particle, its energy and characteristic of the incident surface.

There are two basic forms of electron multipliers that are commonly used in mass spectrometry: the discrete-dynode electron multiplier and the continuous-dynode electron multiplier (often referred to as a channel electron multiplier or CEM). All ETP electron multipliers are of the discrete - dynode type. Figure 3.9 shows the electron multiplier with discrete dynodes and the Figure 3.10 shows electron multiplier with continuous dynodes. A typical discrete-dynode electron multiplier has between 12 and 24 dynodes and is used with an operating gain of between 104 and 108, depending on the application. In GC/MS applications, for example, the electron multiplier is typically operated in analog mode with a gain of around 105.

3.4.2 Faraday cup

A Faraday cup or cylinder is essentially a metal electrode. Ions reach the inside of the cylinder and discharge producing a current which is amplified and measured. The sensitivity of the detector is determined by the noise level of the amplifiers. Figure 3.11 shows the Faraday cup detector
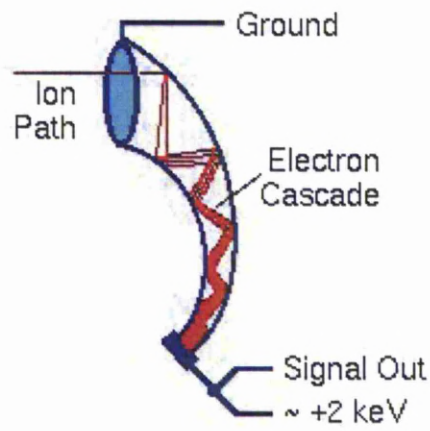
Figure 3.10: Electron multiplier with continuous dynodes
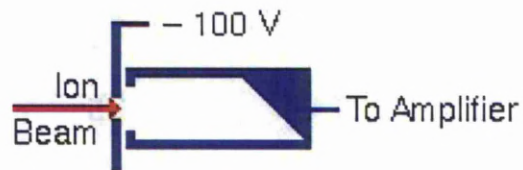
Figure 3.11: Faraday cup detector
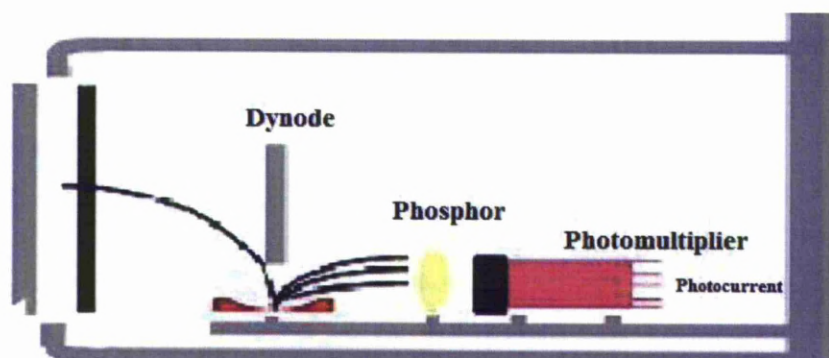
Figure 3.12: Photon multiplier

3.4.3 Photon multipliers

Figure 3.12 shows the photon multiplier with dynodes. Ions exiting the quadrupole are converted to electrons by a conversion dynode. These electrons strike a phosphor which when excited, emit photons. The photons strike a photocathode at the front of the photomultiplier to produce electrons and the signal is amplified by the photomultiplier. The photomultiplier is sealed in glass and held under vacuum. This prevents contamination and allows the detector to maintain its performance for a considerably longer period than conventional electron multipliers.

3.5 Quadrupole mass spectrometer

3.5.1 *QMS* geometry

The geometry of a *QMS* is shown in the Figure 3.13. The analyzer consists of a parallel array of four rod electrodes mounted in a square configuration. An ideal *QMF* is constructed from four parallel hyperbolic cross-section electrodes mounted at a common pitch centre with equal angular spacing of 90° as shown in Figure 3.14, but in practice, for ease of manufacture, round cylindrical rods are employed. By applying radio frequency (*RF*) and direct current (*DC*) potentials between the pairs and by coupling opposite pairs of rods together, the field within the analyzer is created [16].

In the QMS, an alternating electric field generates the required mass selection action. The small size of the quadrupole, its relatively low cost, modest power requirements and linear mass scale have all contributed to its widespread acceptance as an instrument for residual gas analysis (RGA). When the electrodes are energized, by varying the voltages produces a time varying hyperbolic potential in the xy axis, which is invariant along the z-axis as shown in Figure 3.15.

3.5.2   Theory of QMS

A major contributing component to the maximum achievable resolution of a QMS instrument is the quadrupole mass filter (QMF). This component provides mass discrimination by combining the functionality of low mass and high mass filters.

Electrode types

A close approximation to the ideal QMF consists of four hyperbolic shaped electrodes mounted on the corners of an imaginary square and forming a central inscribed circle, the circumference of which just touches the tips of the four electrodes as shown in Figure 3.16. The majority of commercially available QMS utilize a circular electrode QMF as shown in Figure 3.17 to simplify construction and reduce manufacturing costs [53]

Hyperbolic electrodes

An ideal hyperbolic electrode QMF produces a central electric field whose strength increases linearly with increasing displacement from the central axis and is independent in x and y [20], [81].

The hyperbolic field of a QMF is expressed by the following equation [7]

$$E_h \quad = \quad E_0(\lambda x + \sigma y + \gamma z) \tag{3.12}$$
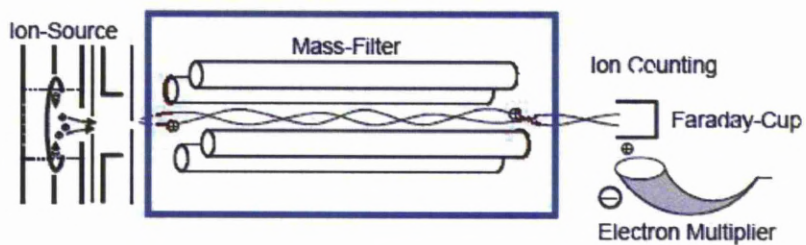
Figure 3.13: Quadrupole analyzer
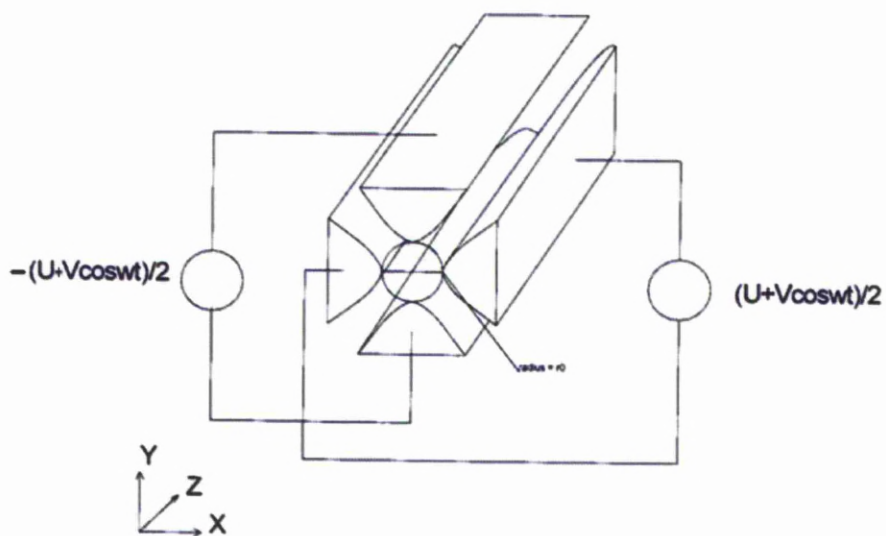
Figure 3.14: Physical arrangement of hyperbolic electrodes for a *QMF*
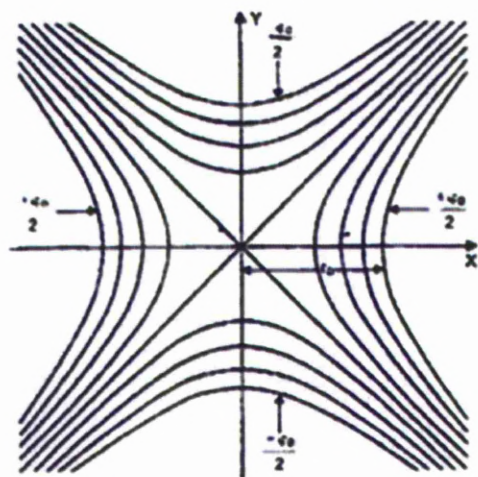
Figure 3.15: Quadrupole potential
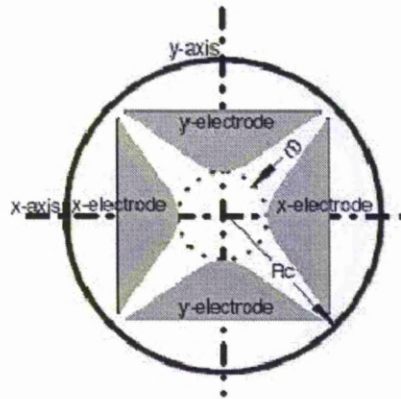
Figure 3.16: Hyperbolic electrode *QMF*
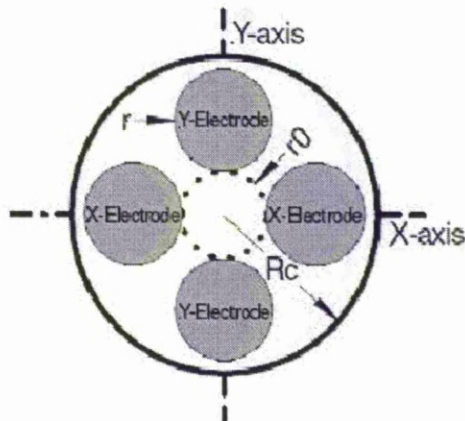
Figure 3.17: Circular electrode *QMF*

where λ, σ, γ are weighting constants and E_0 is a time varying position independent factor.

In this field, the analysis of ion motion is simplified so that it is uncoupled in the three directions. The ion motion can be considered independently in each direction. For an ion in a quadrupole field, the force acting upon it, eE, increases according to the displacement of the ion from zero.

From the above equation the following equation 3.13 can be derived

$$\Phi(x,y,z) \quad = \quad \Phi_0\left(\frac{\lambda x^2 + \sigma y^2 + \gamma z^2}{2r_0^2}\right) \qquad (3.13)$$

This potential distribution satisfies the Laplace equation, and is invariant along the z-axis. For a particular value of Φ_0, the equipotential in the xy plane are four rectangular hyperbolas with asymptotes at 45° to the Cartesian axes, as indicated in Figure 3.15.

If an ion is injected with a certain velocity in the z direction into the mass filter then the ion motion will be in the xz and yz plane. If Φ_0 is a constant, then all ion trajectories would be stable (simple harmonic motion) in the xz plane and would diverge from the z axis (called defocusing) in the yz plane and eventually be lost. On the other hand, if Φ_0 is time variant, the trajectories in both the planes will alternately be deflected towards and away from the zero. The stability can be foreseen in both the planes providing that periodicity is short enough and the ion is heavy enough that it cannot respond sufficiently during the defocusing part of the cycle to escape the device.

Consider the combination of a direct current component in Φ_0 and a periodic alternating component. Light ions are able to follow the alternating component. For the x-direction, they tend to have unstable trajectories whenever the alternating component is larger than the direct component and exhibits oscillation of ever increasing amplitudes. The x-direction is therefore the equivalent of a high pass mass filter. Alternately the y-direction acts as a low pass filter. However, some lighter ions will be stabilized by the alternating component if its magnitude and frequency are adjusted whenever its amplitude is set to increase. The two directions together give a mass filter with a certain pass-band. The motion in the x- and y- directions depend on the variation with time of the potential Φ_0 .

For the QMF, a combination of direct and alternating voltages are chosen for mass analysis. The electric field potential Φ at the surface of the upper and lower electrodes

is given by

$$\Phi = -\frac{[U - V\cos(\omega t)]}{2} \tag{3.14}$$

when

$$y = \pm\sqrt{x^2 + r_0^2} \tag{3.15}$$

Similarly the left and right potentials are

$$\Phi = \frac{[U - V\cos(\omega t)]}{2} \tag{3.16}$$

when

$$x = \pm\sqrt{y^2 + r_0^2} \tag{3.17}$$

where U is a constant, i.e. time-independent voltage, V is the maximum value of a time-varying RF sinusoidal voltage and $\omega = 2\pi f$, where f is the frequency.

The electric field potential Φ between the rods is given by the poisson equation

$$\nabla^2\Phi = \frac{-\rho}{\varepsilon} \tag{3.18}$$

where ρ is the charge density between the rods. Since there is negligible charge in that region, the electric potential,

$$\nabla^2\Phi = 0 \tag{3.19}$$

The general solution to the equation 3.19 is

$$\Phi(x,y) = ax^2 + by^2 \tag{3.20}$$

with $a + b = 0$ (i.e. the sum of the constants a, b must add up to zero.)

By solving the above equation we have therefore

$$\Phi(x,y) = a(x^2 - y^2) \tag{3.21}$$

where the constant a can be determined from the above given boundary conditions.

39

If the y values are given along the surface of the upper and lower hyperbolic rods, then from equations 3.14 and 3.15 we get

$$-\frac{[U - V\cos(\omega t)]}{2} = a(-r_0^2) \tag{3.22}$$

and therefore the electrical potential is uniquely determined by the relation

$$\Phi(x,y) = [U - V\cos(\omega t)]\frac{(x^2 - y^2)}{2r_0^2} \tag{3.23}$$

Similarly if the x values are given along the surface of the left and right hyperbolic electrode, then from equations 3.16 and 3.17, we get

$$\frac{U - V\cos(\omega t)}{2} = a(r_0^2) \tag{3.24}$$

and therefore the electrical potential is uniquely determined by the relation same as equation 3.23. The surface contains a saddle point. If the particle were near the saddle point and the surface oscillates at the correct frequency, the particle executes a stable motion and might get trapped. The particle executes an unstable motion if the surface does not oscillate at the correct frequency.

The injected ion experiences a force given by

$$\vec{F} = -e\nabla\Phi \tag{3.25}$$

From equation 3.23 and 3.25, Newton's equation of motion for a particle with charge e and mass m can be derived in terms of vector equations as follows

$$\frac{d^2x}{dt^2} = -\left(\frac{e}{m}\right)\frac{[U - V\cos(\omega t)]}{r_0^2}x \tag{3.26}$$

$$\frac{d^2y}{dt^2} = \left(\frac{e}{m}\right)\frac{[U - V\cos(\omega t)]}{r_0^2}y \tag{3.27}$$

$$\frac{d^2z}{dt^2} = 0 \tag{3.28}$$

The motion of the charged particle along either x or y-axis in terms of differential

40

equations can be written as

$$\frac{d^2f}{d\tau^2} = -[a - 2q\cos(2\tau)]f \qquad (3.29)$$

where

$$\left.\begin{array}{rcl} a &=& \frac{4}{\omega^2 r_0^2}\left(\frac{e}{m}\right)U \\[2mm] q &=& \frac{2}{\omega^2 r_0^2}\left(\frac{e}{m}\right)V \\[2mm] \tau &=& \frac{\omega t}{2} \end{array}\right\} \qquad (3.30)$$

where τ is a scaled time and if $f = x$ the constants a, q are defined as shown in equation 3.30. Similarly if $f = y$ then a and q are replaced by $-a$ and $-q$.

Mathieu solutions helps in understanding the functioning of a QMS. The general solution of the Mathieu equation (i.e. Equation (3.30)) is given by

$$f = Ae^{\mu\tau}F(\tau) + Be^{-\mu\tau}F(-\tau) \qquad (3.31)$$

where A, B are constants of integration. These constants are determined by the initial values of the x- and y- coordinates and their corresponding velocity components. The quantity μ is a function of the constants a and q and its complex form is given by

$$\mu(a, q) = \alpha + i\beta \qquad (3.32)$$

where α, β are real functions of a and q.

A stable state exists only when $\alpha = 0$ and β is not equal to an integer, i.e. it exists only for certain values of a and q. In other cases the x- and y- coordinates of the charge become very large as time increases which results in unstable motion of the charged particles between the rods and so that they are lost. In the stable state, the ion oscillates between the free space of the rods and reaches the detector safely.

Circular electrodes

Circular electrodes produce a more complex field, which arises from a quadrupolar potential (second order) and higher order components. The resultant is termed a multipole potential[2]. This potential equation is given by

$$\Phi(x,y) = \sum_{n=0}^{\infty} \frac{A_n \Phi_n}{r_0^n} \tag{3.33}$$

where A_n is the amplitude of the multipole Φ_n consisting of $2N$ poles, with $A_o \Phi_o$ defining the offset potential, $A_1 \Phi_1$ defining the dipole potential, $A_2 \Phi_2$ defining the quadrupole potential, $A_3 \Phi_3$ defining the hexapole potential and continuing thereon. For the four fold symmetric QMFs as considered here, only multipole terms $n = 4N + 2$ for $N = 0, 1, 2, 3, \ldots$ contribute to the field.

$$\Phi = \frac{A_0 \Phi_0}{r_0^0} + \frac{A_1 \Phi_1}{r_0^1} + \frac{A_2 \Phi_2}{r_0^2} + \frac{A_3 \Phi_3}{r_0^3} + \ldots + \tag{3.34}$$

Mathieu stability functions

If β is equal to an integer then it produces curves in the a, q plane where stable solutions do not exist. On the other hand for special combinations of a and q boundaries are established between regions in which stable solutions exist.

Rewriting the equation 3.29, we get

$$\left\{ -\frac{d^2}{d\tau^2} + 2q \cos(2\tau) \right\} f = af \tag{3.35}$$

The curly brackets in the equation 3.35 are called the eigenvalues of the operator, because for a given value of q, only special values of a are allowed. There is a eigenfunction f for each eigenvalue of a. The cosine value in equation 3.35 is periodic and an even function of τ and hence the eigenfunctions must be either even or odd functions.

42

For $q = 0$,

$$f_\gamma = \begin{cases} \cos(r\tau) \\ \sin(r\tau) \end{cases}, a = r^2 \tag{3.36}$$

For $q \neq 0$,

$$f_\gamma = \begin{cases} ce_\gamma(\tau) \\ se_\gamma(\tau) \end{cases}, a(q) = \begin{cases} a_\gamma(q) \\ b_\gamma(q) \end{cases} \tag{3.37}$$

where $ce_\gamma(\tau, q)$ are even eigenfunctions and $se_\gamma(\tau, q)$ are odd eigenfunctions of the Mathieu equation. Because of the different even and odd values of the eigenfunctions, the curves cannot cross each other no matter what the value of q as shown in the figure 3.18. The shaded areas in the Figure 3.18 show the regions in the stability plane (a, q) which correspond to simultaneous stability for the both x and the y coordinates. Figure 3.19 shows clear view of the first stable region coloured pink. The value of q which corresponds to the maximum value of $-a_o$, and b_1 curves is $q_{max} = 0.706$ and the value of either $-a_o$ or b_1 at this point is 0.24276
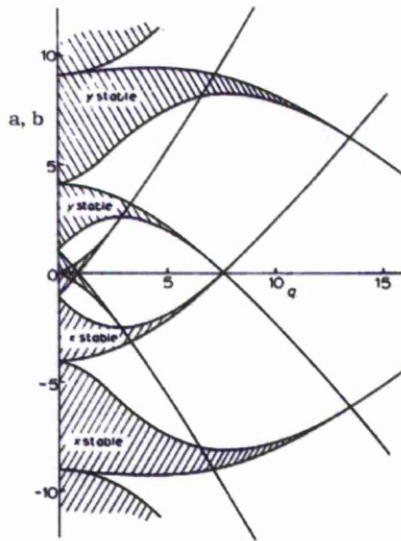
Figure 3.18: Stability diagram showing the regions of stability plane (a,q) for both x- and the y- coordinates
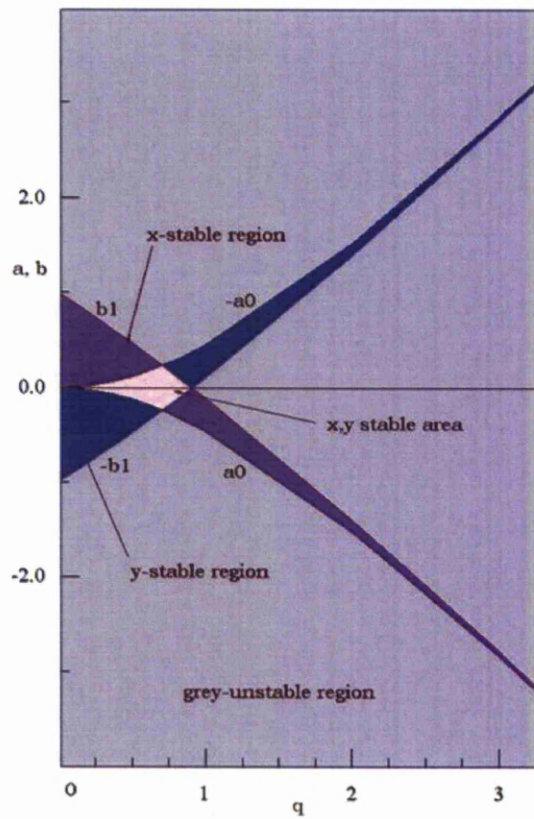
Figure 3.19: Expanded view of the first stable region

Chapter 4

SOFTWARE

A simulation software suite has been developed in the .Net environment using visual C++ to model the performance of the Quadrupole mass spectrometer (*QMS*) for both hyperbolic and circular rod quadrupole mass filter (*QMF*). The computer code consists mainly of two programs, viz. QMS2-Hyperbolic/QMS2-Field and QMS2-Ion.

4.1 QMS2-Hyperbolic

The graphical user interface (*GUI*) of QMS2-Hyperbolic is divided into a number of control groups containing user controls consisting of one or more text boxes, combo drop down, check boxes, radio buttons [112]. Mass scan range, voltages and the geometry of filter can be set in QMS2-Hyperbolic user interface. Figure 4.1 shows QMS2-Hyperbolic *GUI*.

4.1.1 Mass scan range

Mass scan range controls the m/z range of a mass scan simulation and consists of the text boxes such as start, stop and steps. The start and stop value (integer) of the mass scan m/z can be set in their respective boxes.
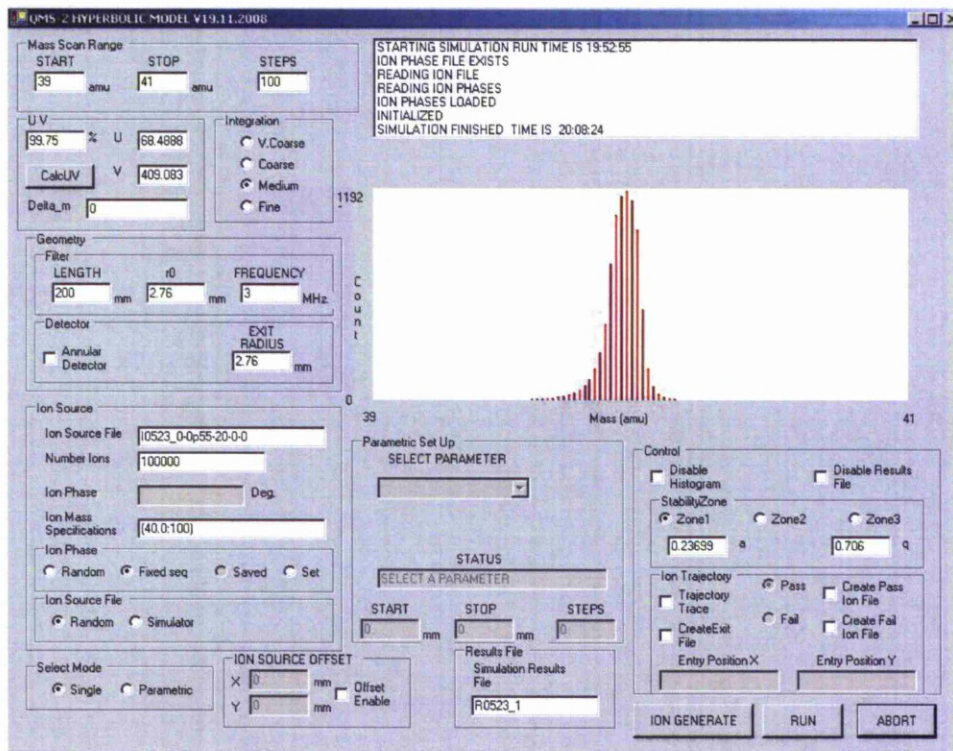
Figure 4.1: QMS2-Hyperbolic *GUI*

4.1.2   U and V

For a given mass-to-charge ratio the values of the voltages U and V can be calculated for particular points on the a-q plane, as shown in the Figure 4.2.

The mass scan line shown in the figure represents one possible set of values. As the slope of the scan line increases, the line approaches the apex of the stable envelope and the range of mass-to-charge ratios that pass successfully through the filter decreases, the resolution increases and the sensitivity decreases. Conversely as the scan line slope decreases, the range of mass-to-charge ratios that are passed successfully increases, the resolution decreases with a corresponding increase in sensitivity(explained in Chapter1, Section 1.1). The scan line determines the resolution of the scan The movement of the mass scan line can be achieved by varying V along the line $U = (const/2)V$.

46
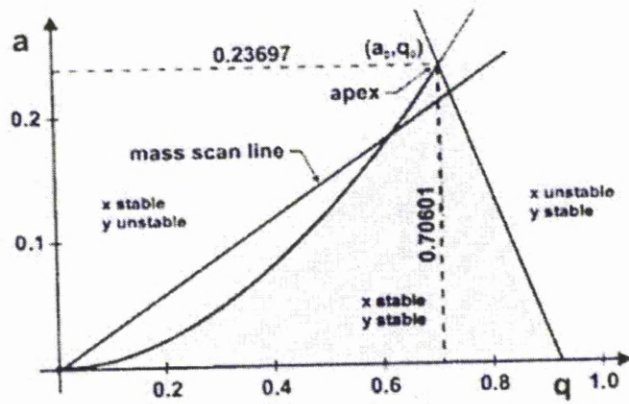
Figure 4.2: Stability region Zone 1 (a-q plane)
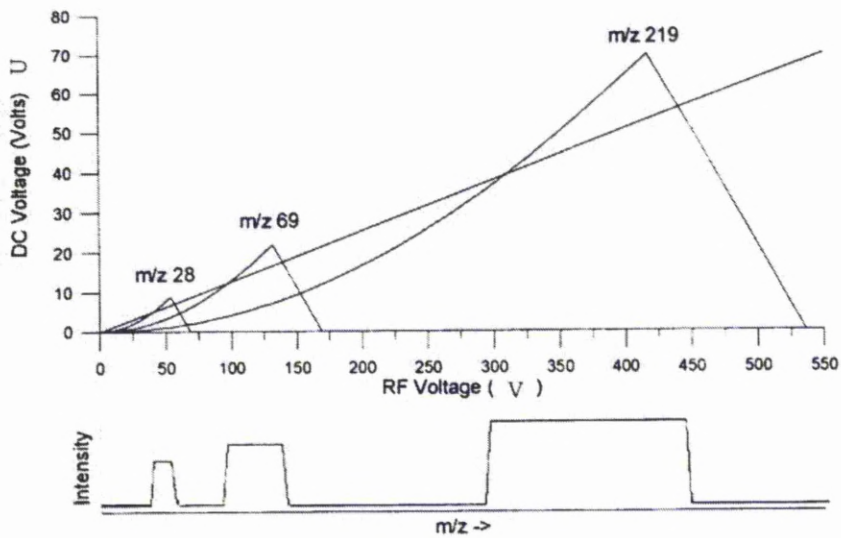
Figure 4.3: stability boundary of the first stable region (Zone 1) and mapping in to the

V,U plane for a given mass-to-charge ratio

Solving the equation 3.31 for U and V we get,

$$V = \frac{r_0^2 \omega^2}{8} \left(\frac{m}{e}\right) q \qquad (4.1)$$

$$U = \frac{r_0^2 \omega^2}{4} \left(\frac{m}{e}\right) a(q) \qquad (4.2)$$

Figure 4.3 shows how the $a(q)$ verses q stability boundary of the first stable region can be mapped onto the V, U plane for a given mass to charge ratio. It is very clear from the figure that as the mass scan line approaches the tip of the stability region, the peak width of the mass spectrum reduces.

By altering the absolute values of the U and V voltage amplitudes but keeping the ratio between the two the same, ions of a different charge to mass ratio are transmitted through the filter. Therefore UV controls the simulated mass filter resolution. Figure 4.1 shows the UV section of the QMS2-Hyperbolic user interface. Percentage (%) represents the QMF resolution which alters the effective slope of the mass scan line and 100% corresponds to $a = 0.2366$ and $q = 0.706$ on the stability diagram. U displays the current mass scan point dc voltage value (resolution dependent). V displays the current mass scan point ac voltage value. CalcUV operation provide the U and V voltage values for the current resolution and mass start value.

4.1.3 Integration

In the integration section of the QMS2-Hyperbolic user interface, there are four radio switches which is used to control the Runge-Kutta step size. Runge-kutta integration is a clever extension of Euler integration that allows substantially improved accuracy, without imposing a severe computational burden. The idea is to step into the interval and evaluate derivatives. This is similar to shortening time step in Euler integration, but provides more accuracy with less increase in computation. The four radio switches includes V Coarse, Coarse, Medium and Fine. V coarse is suitable for a quick check but low accuracy. Fine is suitable for highest accuracy but increases the time steps.

4.1.4 Geometry

The physical characteristics of the QMF to be simulated can be set by the geometry section of the QMS2-Hyperbolic user interface. The geometry section consists of the text boxes such as Filter and Detector. In the filter section the length of the QMF, the field radius, RF excitation frequency and detector radius can be set. In the detector section the context of the value of exit radius, inner radius of the detector and outer radius of the detector can be set.

Filter

Length   :   Length of the QMF in mm

r_0 :   Field radius in mm

Frequency : RF excitation frequency in Hz.

Exit Radius :   Detector radius mm

Detector

Annular detector :   Enables an additional text box and

                         changes the context of the Exit Radius

Inner radius   :   Inner radius of the detector in mm

Outer radius   :   Outer radius of the detector in mm (previously exit radius)

4.1.5 Ion source

The Ion Source section of the QMS2-Hyperbolic user interface consists of the text boxes ion source file, number of ions, ion phase, ion mass specification.

In the Ion source file box, the required ion source file name can be entered. The file stores all the files related to the ion source that have been simulated by the software. In the Number of ions box the integer value for the number of ions to simulate at each mass scan point can be set. Ion phase is used to set the ion phase group controls. Ion mass specification defines the m/z-value(s) for the ion(s) entering the QMF. The Ion

Phase section consists of random, fixed sequence, saved, and set check-in boxes. The Ion Source File section consists of two check-in boxes, one is random for default settings and other is simulator for not applicable. Select Mode is used to switch between the single sweep mode and the parametric sweep mode. By selecting Single, the single sweep mode can be selected and a single mass scan is undertaken using the parameters displayed on the *GUI*. Similarly by selecting Parametric, the parametric sweep mode can be selected and additional user controls are activated on the *GUI*. Finally the result file automatically generates a result file name of the format *RMMDD* Number, where *R* - fixed start character, *MM* − 2digit for month, *DD* − 2 digit for day and Number indicates incrementing number starting at 0.

Ion source

Ion source file   :   Enter required ion source file name.

Number of ions   :   Integer value for the number of ions to simulate at

each mass scan point.

Ion phase   :   Not normally enabled, see Ion Phase group controls.

Ion mass   :   Defines the m/z value(s) for the ion(s) entering the *QMF*.

Specification   :   Requires the following format

m/z value : percentage (40:100)

Entered value 40 m/z ion

100% indicates all ions of this type

If parameter number of ions = 100,000 then 100,000 ions of

$m/z = 40$ would be simulated (i.e trajectories calculated)

at each mass scan point.(20:25)(32:75)

Entered value : 20 m/z ion

25% indicates a quarter of the ions are this type

32 m/z ion

75% indicates three quarters of ions are this type

If parameter number of ions = 100,000 then 25,000 ions of

m/z =20 would be simulated at each mass scan point and

75,000 ions of m/z =32 would be simulated at each mass scan point.

Ion phase

Random	:	Each mass scan starts from a random place in the ion file.
Fixed sequence	:	Each mass scan starts from the same place in the ion source file.
Saved	:	Enabled by trajectory mode, uses the ion phase stored in the trajectory file.
Fixed	:	The program ignores the phase value held in the ion file and uses the value entered in the Ion Phase box in group Ion Source.

Ion source file

Not an active control group, provided for future functionality. Leave at default setting.

Random	:	Default setting
Simulator	:	Not applicable

Select mode

Used to switch between single sweep mode and parametric sweep mode.

Single	:	Selects single sweep mode. A single mass scan is undertaken using the parameters displayed on the *GUI*.
Parametric	:	Selects parametric sweep mode. Additional user controls are activated on the *GUI* (see group Parametric Set Up).

Ion generate

Runs QMS2-Ion

Ion Source Offset

Offset selects the ion offset mode and enables the following additional controls. Provides a means of simulating an ion source that is not correctly aligned with the x and y axis of the QMF.

X : X axis ion source offset in mm (Numeric value can be $+/-$)

Y : Y axis ion source offset in mm (Numeric value can be $+/-$)

Results File

Automatically generates a result file name of the format *RMMDD* Number. Where *R* is a fixed start character

MM = 2 digit for month

DD = 2 digits for day

Number = Incrementing number start at 0

4.1.6 Profiler

It is a utility function to classify ion entry position or ion detector position onto a user-defined 2D grid and it also defines the grid size

Generate Ion 2D profile : Classify ion entry position

Generate Exit 2D Profile : Classify ion detector position

Grid size : Define XY square grid size in mm.

4.1.7 Control

The simulator functionality can be controlled using this section of the QMS2-Hyperbolic user interface.

Disable Histogram : Disables real time histogram display. Allows faster execution. Speed, useful when a large number of sweeps are to be undertaken (ie parametric mode).

Disable Report   :   Disables the generation of the report files.

Useful, when undertaking quick-look simulations for choosing simulation settings etc. Avoids generation of a large number of unwanted files.

4.1.8   Stability zone

Selects the required stability zone and displays the a and q values in text boxes corresponding to the tip of the stability zone. The displayed values can be changed manually if required.

Zone 1   :   Selects stability Zone 1.

Zone 2   :   Selects stability Zone 2.

Zone 3   :   Selects stability Zone 3.

4.1.9   Ion trajectory

This function can be used only when operation is on single ion mode.

Trajectory trace   :   Switches between mass scan and ion trajectory mode.

Unchecked   :   Mass scan mode

Checked   :   Trajectory trace mode. Enables Select Source File and Cancel Trajectory Mode user controls.

Pass   :   Displays list of files containing successful ion start conditions. Enabled when trajectory trace mode selected.

Fail   :   Displays list of files containing unsuccessful ion start conditions. Enabled when trajectory trace mode selected.

Select Source   :   Enabled when in trajectory mode. Used to select required

File/Select Ion	:	Ion start file. When file selected switch changes
		context and label to Select Ion and contents of
		trajectory start file is displayed. Use Select Ion to
		choose one of the ion start conditions.
Cancel Trajectory Mode	:	Switches mode back to mass scan mode.
Create Pass Ion File	:	For each mass scan step creates a file containing ion start conditions that results in a successful hit on the detector. Enabled when mass scan mode is selected.
Create Pass Ion File	:	For each mass scan step creates a file containing ion start conditions that fail to hit the detector. Enabled when mass scan mode is selected.
Create exit file	:	If enabled creates a file containing the ion position when detected.
Unchecked	:	No exit file.
Checked	:	Creates file of ion exit positions.
Entry Position X	:	Displays the X axis entry position of the selected ion. Value can be altered by user. Enabled when trajectory trace mode selected.
Entry Position Y	:	Displays the Y axis entry position of the selected ion. Value can be altered by user Enabled when trajectory trace mode selected.

Figures 4.4 and 4.5 show typical behaviour of the trajectories of an ion transmitted for different operating parameters. Figure 4.4 shows the simulation of ion trajectories in the x- and y- directions for $^{40}Ar^+$ operated in stability Zone 1 (i.e., $a = 0.23699$ and $q = 0.706$). The simulation was carried out using QMS2 hyperbolic software by setting the following parameters, mass filter length $(l) = 100$ mm, frequency $(f) = 50$ MHz,

U/V - 99.99%, field radius (r_0) = 0.15 mm, exit radius = 10 mm, nominal energy (E)
= 5 eV, source radius = 0.5 mm, number of ions = 100.

Figure 4.5 shows the simulation of ion trajectories in the x- and y- directions for
$^{40}Ar^+$ operated in stability Zone 1 (i.e., $a = 0.23699$ and $q = 0.706$). The simulation
was carried out using QMS2 hyperbolic software by setting the following parameters:
mass filter length (l) = 50 mm, frequency (f) = 10 MHz, $U/V - 99\%$, field radius (r_0)
= 0.09 mm, exit radius = 10 mm, nominal energy (E) = 2 eV, source radius = 0.5 mm,
number of ions = 100.

4.2 QMS2-Field

QMS2-Field is an ion trajectory simulation program for circular electrode quadrupole
mass filters. Figure 4.6 shows the QMS2-Field *GUI* [113].

The software consists of a *GUI* exactly the same as QMS2-Hyperbolic *GUI* with
an additional field file section in the program. The field files are generated by third
party tools copied into the Field folder.

LIST FIELD FILES button in the QMS2-Field File *GUI* displays the field files
contained in the Field folder. One selects the file for the required r/r_0 ratio. The field
file name is constructed as follows QMFXXXX.GRD. Where XXXX represents the
r/r_0 ratio. For example, GRD1127.GRD is the field file for a circular rod *QMF* with
an $r/r_0 = 1.127$. When the file is selected the r/r_0 text box in the geometry area of the
GUI reflects the chosen field file r/r_0 ratio.

4.3 QMS2-Ion

By choosing the Ion Generate button, QMS2-ION can be called from QMS2-models.
Figure 4.7 shows the QMS2-Ion *GUI*.
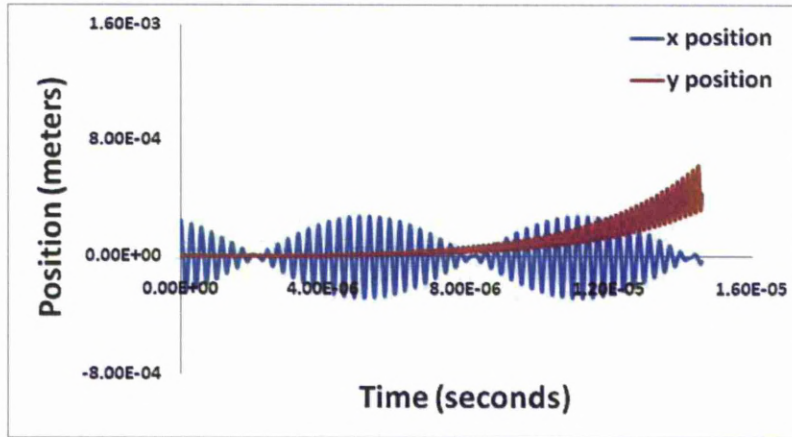
Figure 4.4: Numerical simulation of ion trajectories in x- and y- directions for ^{40}Ar$^+$ for the *QMF* electrodes of length 100 mm
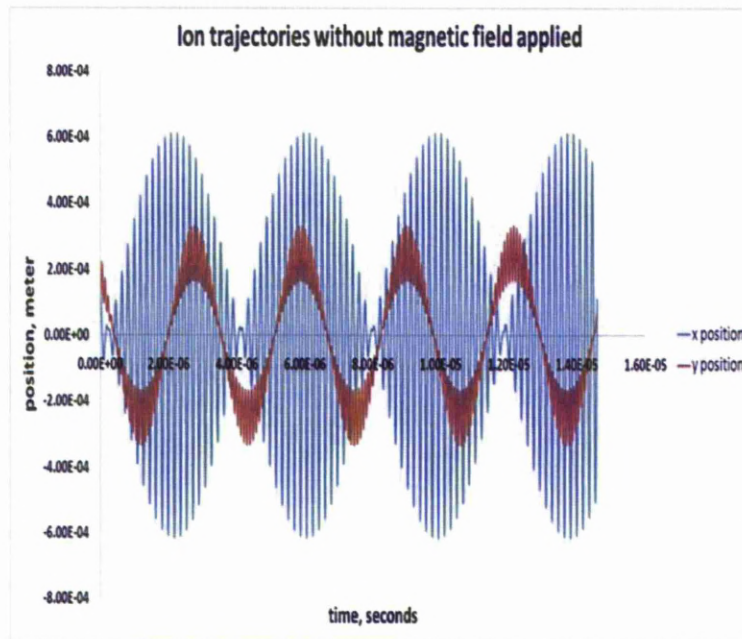
Figure 4.5: Numerical simulation of ion trajectories in x- and y- directions for ^{40}Ar$^+$ for the *QMF* electrodes of length 50 mm
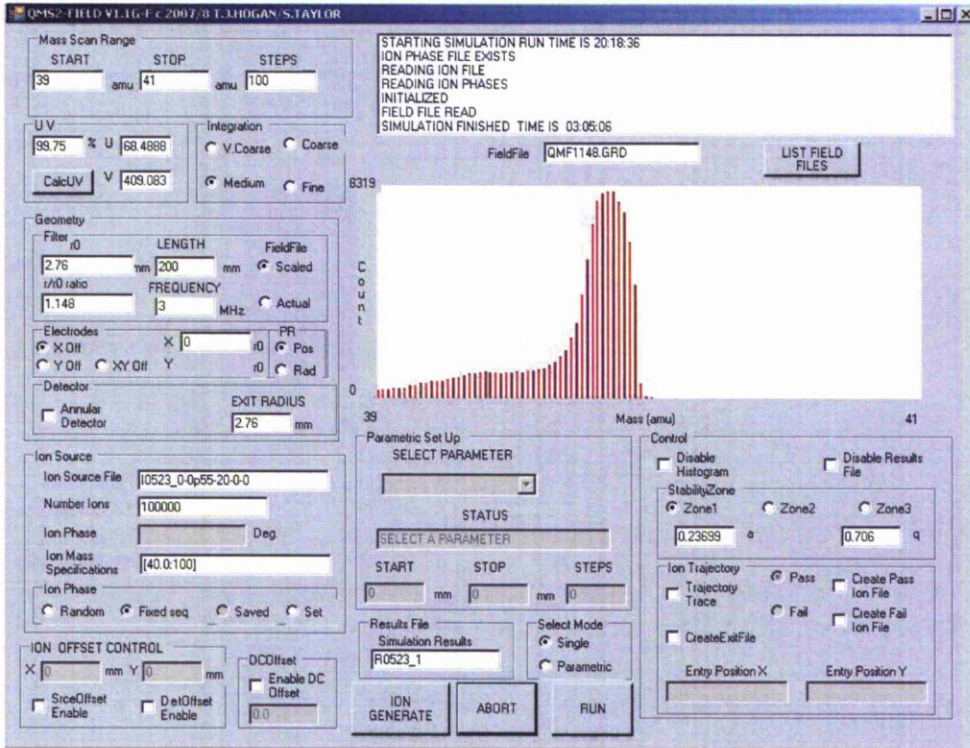
Figure 4.6: QMS2-Field *GUI*
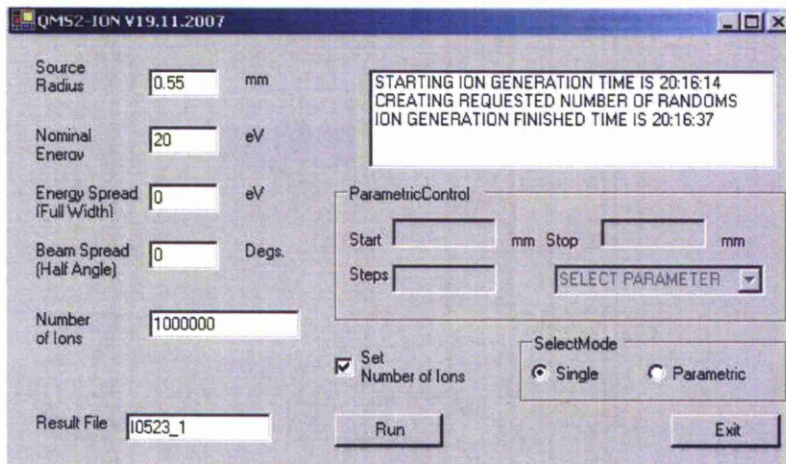
Figure 4.7: QMS2-Ion *GUI*

This program simulates an ion source by generating a large number of individual ion start conditions and storing them in a binary file which is read by the QMS2-Hyperbolic program.

4.4 QMS2-Hyperbolic simulation results

The main objective of this section is to show the mass spectra of gases modelled using QMS2-Hyperbolic program operated in Zone1/Zone3 by setting different values of the mass spectrometer dimensions and applied input signals. The value of K (see Chapter 1, Section 1.1) is also calculated from mass range and resolution graph plotted for Zone 3. These test simulations will enable the use of the QMS2-Hyperbolic program to model the mass spectra of different gases for later research studies.

4.4.1 Modelling of mass spectrum of air

Air mass spectrum

The layer of gases surrounding the planet Earth and retained by the Earth's gravity is called the Earth atmosphere. The Earth atmosphere contains about 78.09% of nitrogen, 20.95% of oxygen, 0.93% of argon, 0.04% of carbon dioxide, 0.0018% of neon, 0.0005% of helium, 0.0001% of krypton, 0.0005% of hydrogen, 0.000008% of xenon, 0.000002% of ozone and some traces of radon. Figure 4.8 shows the proportional volume of gases comprising dry air.

Simulated mass spectrum of air

By setting the values of the QMF length (l), frequency (f), field radius (r_0), exit radius, nominal energy (E_n) and, source radius, the simulated mass spectrum of atmospheric air is generated by running the programs QMS2-Hyperbolic and QMS2-Ion. Using QMS2 software, it is possible to model a maximum of three gases at a time.

58
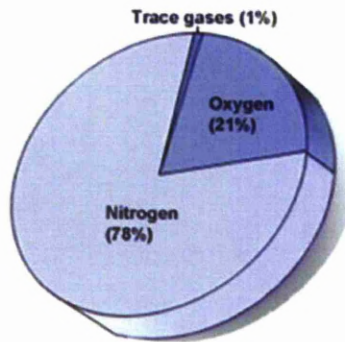
Figure 4.8: Proportional volume of gases comprising dry air

Since the number of gases present in air is more, the simulation has to be run more than twice considering the most important gas components, which contribute the major percentage of the total volume of air.

Figure 4.9 shows the mass spectrum of air modelled using the QMS2 hyperbolic software by setting the following parameters, mass filter length $(l) = 40$ mm, frequency $(f) = 3.68$ MHz, field radius $(r_0) = 0.1$ mm, exit radius = 0.9 mm, nominal energy (E_n) = 3 eV, source radius = 0.8 mm, number of ions = 62500, and varying the mass scan range according to the gas taken.
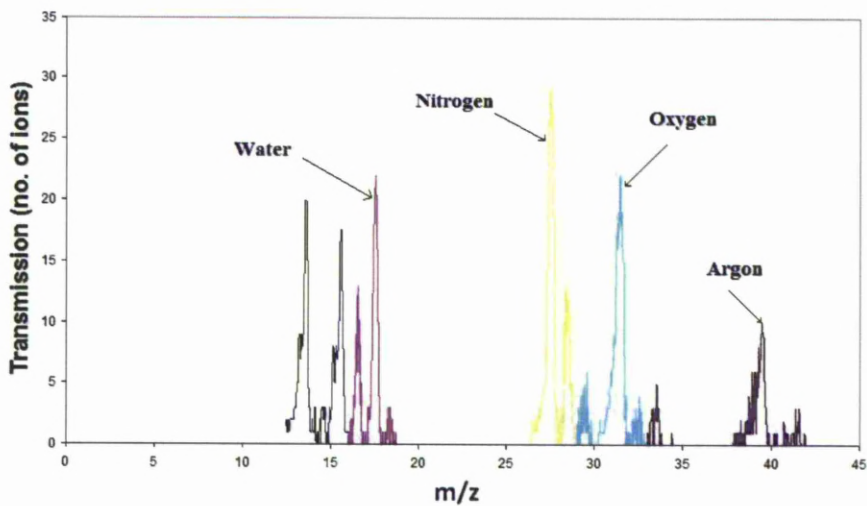
Figure 4.9: Mass spectrum of air modelled using QMS2 software

Table 4.1: Computer Simulation Test Conditions

QMF PARAMETER	CONDITION
Length	250 mm
r0	6 mm
Detector radius	10 mm
Ion Source	
Ion energy	20 eV
Ion Source radius	0.5 mm
Ion energy spread	0
Ion angular spread	0
Ion species	40 m/z

4.4.2   Modelling of mass spectrum of argon gas

Presented here are the simulated mass spectra for argon gas using the computer simulation software described, and operated at the upper left hand tip of stability Zone 3 ($a = 3.16$ and $q = 3.23$). All the simulations use 300 steps across the mass range, with 1×10^5 ions traced at each mass step. The other computer simulation test conditions are given in Table 4.1.

Figure 4.10 shows the simulated mass spectra of argon gas of m/z 40 with the frequency in the ranges from 4 to 8 MHz. In the mass spectrum shown in Figure 4.10, the x-axis displays mass-to-charge ratio and the y-axis displays number of ions transmitted. Increase in the frequency results in an increase in the number of cycles thereby an increase in resolution which in turn results in the increase in peak heights.

Figure 4.11 shows the number of RF cycles versus the maximum resolution for the argon gas of m/z 40 with the frequency in the ranges from 4 to 8 MHz. The value of K (see Chapter 1, Section 1.1) was calculated using the equation 1.1 and was found to be close to 6 for the quadrupole mass analyzer operated in Zone 3.
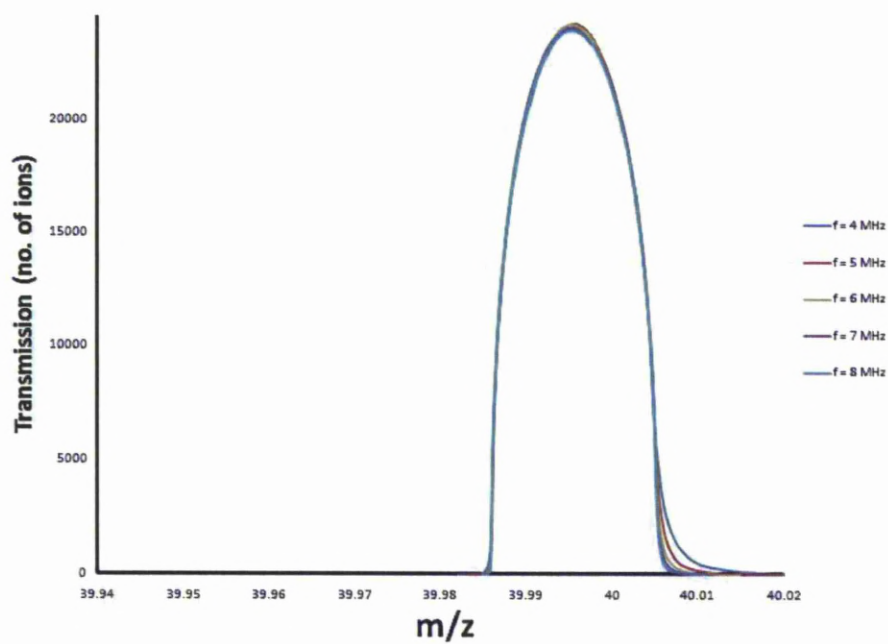
Figure 4.10: Simulated mass spectrum of argon gas showing the variation of peak width with increasing frequency
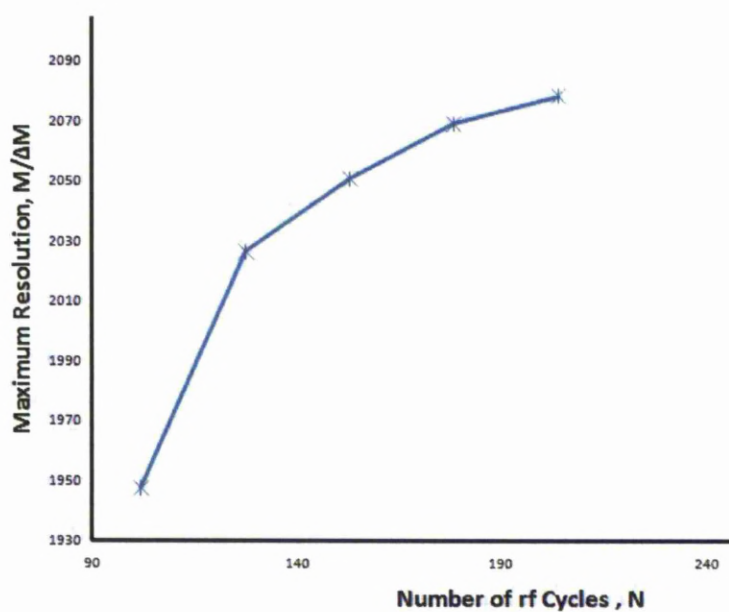
Figure 4.11: Maximum resolution versus number of rf cycles

Table 4.2: QMS2-Field computer simulation test conditions

QMF PARAMETER	CONDITION
Length	254 mm
r0	2.76 mm
Frequency	2 MHz
U/V	99.75
Detector radius	2.76 mm
Ion Source	
Ion energy	2 eV
Ion Source radius	0.5 mm
Ion energy spread	0
Ion angular spread	0
Ion species	40 m/z

Table 4.3: Comparison of QMS resolution and transmission for values of r/r_0

r/r0	R(M/ΔM)	T (%)
1.148	56.91	9.1
1.127	133	10.53

4.5   QMS2-Field simulation results

A few simulation studies have been carried out to become familiarized with the QMS2-Field simulation package. Reported here are the simulated mass spectra for argon gas using the QMS2-field simulation software described previously and operated at Zone $1(a = 3.16$ and $q = 3.23)$. All the simulations used 100 steps across the mass range, with 1×10^5 ions traced at each mass step. The other computer simulation test conditions are shown in the Table 4.2.

Figure 4.12 shows the computed $^{40}Ar^+$ spectra for circular rods with two values of r/r_0 and with hyperbolic rods. All the simulations determined the QMS peak profiles with the number of ions equal to 10^5 for single mass step between the mass scan range 38.5 and 40.5 m/z

Using the simulation programs QMS2-Field and QMS2-Hyperbolic , with 60 cycles of RF, a comparison of resolution at 10% peak height and transmission through QMS using filters as shown in Table 4.3.
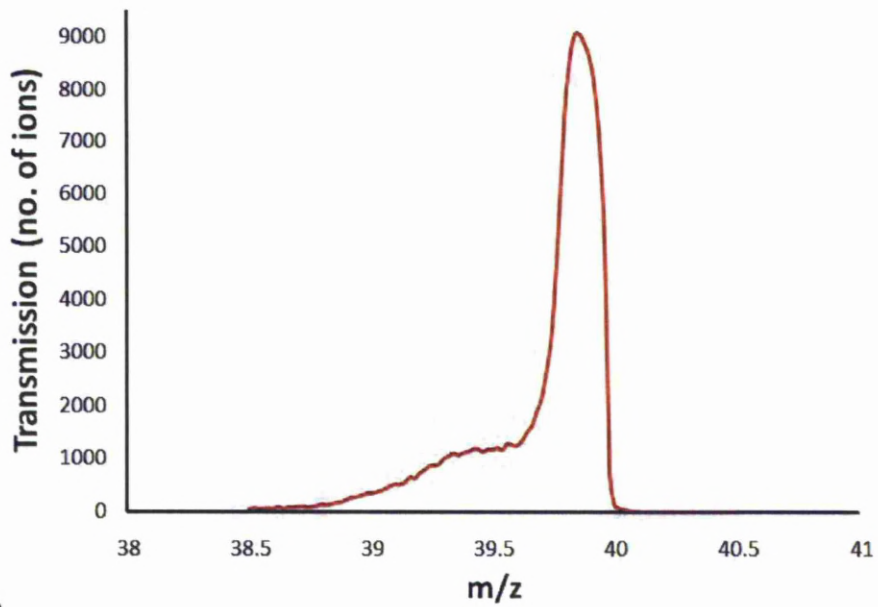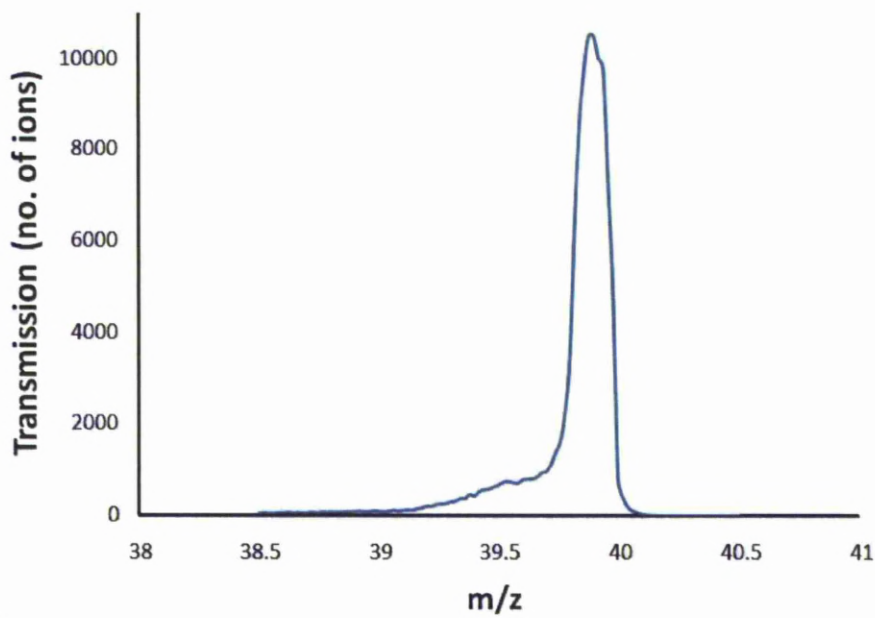
Figure 4.12: Computed ^{40}Ar$^+$ mass spectrum, a) with circular electrodes of $r/r_0 =$ 1.127, b) with circular electrodes of $r/r_0 = 1.148$

4.6 Conclusions

A computer model of a *QMS* has been developed (see Chapter 1, Section 1.2) for both hyperbolic and circular shaped electrodes, which allows the field study of electrodes of any *QMS* electrode geometry to be used. *QMS* models can model the very large number of ions ($> 10^5$), which cannot be generated in other ion optics packages (e.g.) SIMION [40]. The disadvantage of the model is that it does not support three dimensional modelling. In the following chapter, the use of this *QMS* model to simulate the performance of high resolution *QMS* instrument is described.

Chapter 5

A QUADRUPOLE MASS SPECTROMETER FOR RESOLUTION OF LOW MASS ISOTOPES

5.1 Atomic theory

Atomic theory originated with an idea that matter is made of extremely small particles called atoms. Later research works discovered that an atom internally is made up of smaller particles. It was early 300 BC when that Democritus came up with a conceptual definition of an atom as invisible particles which are indivisible [97]. It was the later work of Dalton in 1803 which laid the foundation of atomic theory of modern chemistry [12]. Dalton postulated that atoms of the same element are similar to one another and equal in weight, but that the weights of atoms of different elements are different. The background for this theory was the law of conservation of mass and the law of constant proportions [79] [82].
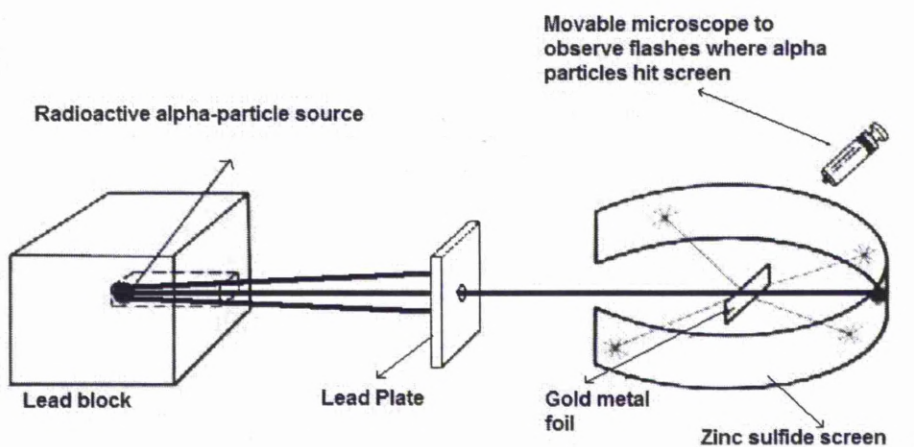
Figure 5.1: Gold foil experiment showing alpha-particles scattering from metal foil

In 1897, J.J. Thomson, with his discovery of the electron, dramatically changed the modern Dalton's view of atom as solid, unbreakable spheres. With the discovery of Eugen Goldstein in 1886 that the atoms had positive charges, Thomson suggested that the atoms are solid spheres made up of a solid positive with embedded tiny negative particles. Later research works performed with radio active alpha particles by Ernest Rutherford in 1908, a former student of Thomson, proved that Thomson's view of atomic structure was incorrect. He suggested that the nucleus is positive and the electrons are revolving outside the nucleus. In conjunction with Geiger and Marsden, Rutherford's gold foil experiment provided evidence for the nucleus due to the scattering of alpha particles. Figure 5.1 shows a schematic diagram of the gold foil experiment showing alpha-particles scattering from metal foil. The nucleus was suggested to be a positively charged body. These positively charged particles in the nucleus of the atom were called protons, which are much larger and heavier than electrons. Figure 5.2 shows J.J. Thomson's "plum pudding" atomic model and Rutherford's atomic model.

Rutherford discovered the pattern by using alpha particles from a radioactive source. He and his co-workers found that when a beam of alpha particle radiations was directed towards a thin film of metal foil, they were scattered from their original paths in a sys-

66
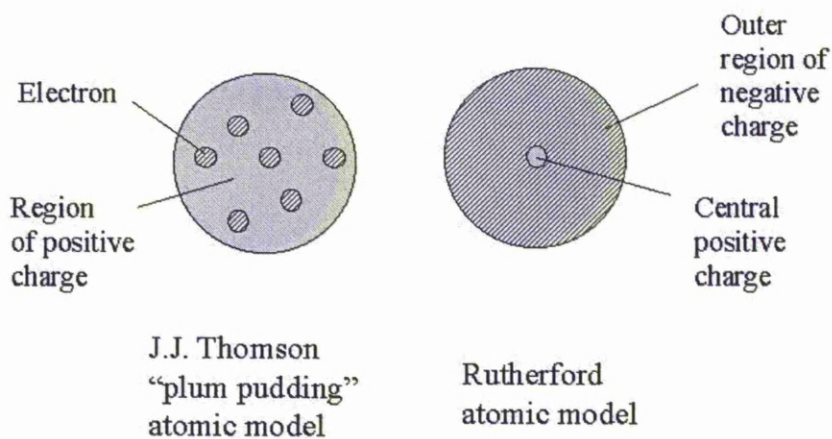
Figure 5.2: J.J. Thomson and Rutherford atomic models

tematic way. The pattern of the back scattered alpha particles could only be explained by assuming that most of the mass of an atom was in a small, dense, central core or nucleus which carried a positive electric charge, and that the nucleus was surrounded by a number of much lighter, negatively charged electrons.

This theory was further extended by Bohr, who showed how the electrons could be assigned to particular paths or orbits around the nucleus, similar in essence to the orbits of planets around the sun. The electrons are sufficient in number to neutralize the charge on the nucleus, leaving the atom uncharged as a whole. Figure 5.3 is a diagram of the atom of hydrogen, the lightest and simplest atomic system, having only one electron which balances a single positive charge on the nucleus. Figure 5.4 shows an atom of the light metal, beryllium, with four orbiting electrons and a mass nine times that of the hydrogen atom.

The nucleus accounts for most of the atomic weight, but it is the electrons which enter into the encounters with other atoms and, in particular, it is the electrons which determine the chemical properties. The nuclear charge is equal to a whole number (Z) times the charge on the hydrogen nucleus. The parameter Z is called the atomic number and each atomic number defines a chemical element. Ninety different elements are found in nature, with atomic numbers ranging from 1 (hydrogen) to 92 (uranium).
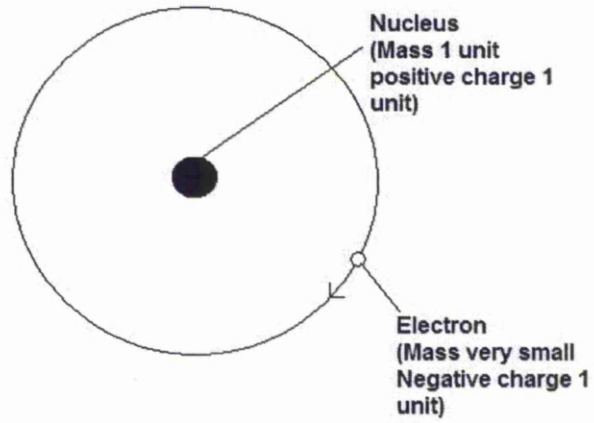
Figure 5.3: Hydrogen atom
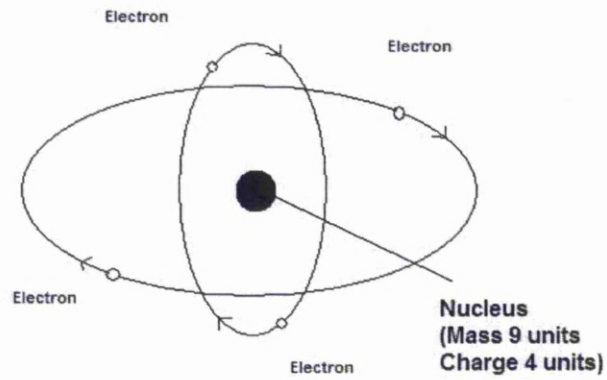
Figure 5.4: Beryllium atom
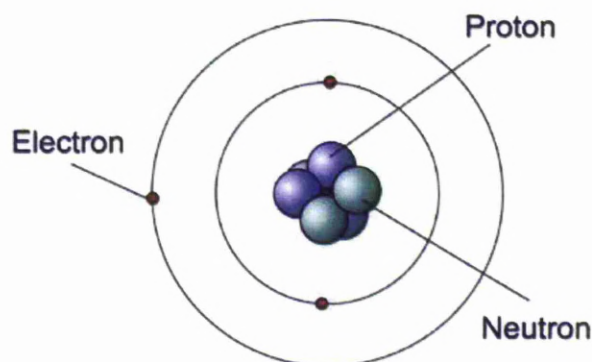
Figure 5.5: Chadwick atomic model

Further work by Chadwick in 1932 revealed a third type of subatomic particle within the nucleus of the atom, which he named the neutron.The atomic number describes the number of protons in the nucleus. For a neutral atom this is also the number of electrons outside the nucleus. Subtracting the atomic number from the atomic mass number gives the number of neutrons in the nucleus. Figure 5.5 shows Chadwick atomic model showing electrically neutral neutrons.

5.1.1 Isotopes

The existence of isotopes are atoms of the same element which have the same atomic number (i.e., the same number of protons) but different mass number and this was established by the chemist, Soddy. The word 'isotope' is derived from two Greek words *isos topes* meaning 'the same place' and referring to their identical position in the periodic table of the chemical elements. The development of Aston's mass spectrograph in 1919 showed that many of the natural elements are composed of atoms with different masses. Isotopes of an element have similar chemical properties. In addition to the natural isotopes, others can be made artificially. These are the radioactive isotopes or radioisotopes.
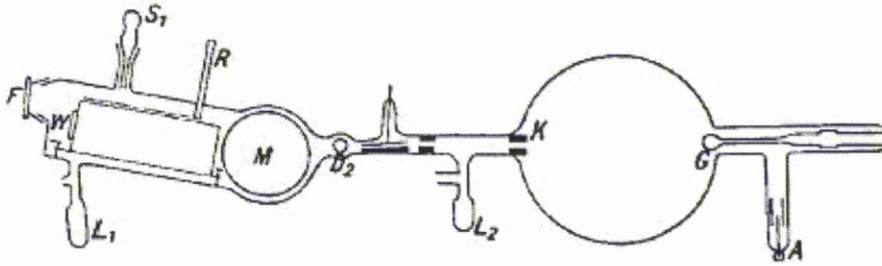
Figure 5.6: Aston mass spectrograph

Aston mass spectrograph

Figure 5.6 shows the spectrograph of Aston. It consists of a discharge tube with an anode A, cathode K and a beam dump G for the cathode rays. The ions pass in front of the deflection plates and behind them fine slits S_b and D_2 and penetrate then the magnet field M. Before making the photograph, the patch of the canal rays on the screen discovered by Willemit W can be observed through the window F. L_1 and L_2 are pumps (liquid air traps).

The beam of charged particles produced in the right tube of the instrument pass through a small hole in the cathode and a narrow slit in front of the deflection plates. After traversing the bending magnetic field, which is perpendicular to the electric field, the rays impact on to photographic paper. The position of the spot focussed on to photographic paper depends only upon the ion mass, not upon ion kinetic energy.

5.1.2 Low mass isotopes

We have seen that an atom is composed of three types of particles: protons(+), neutrons(0), and electrons (-); the electrons are bound to the nucleus by the force due to the positively charged protons. In the periodic table, elements with lowest mass are hydrogen with an atomic weight of 1.00794 amu and helium 4 with an atomic weight

70

Table 5.1: Low mass isotopes

SYMBOL	MASS	UNITS
H	1.007825	amu
D	2.014101779	amu
T	3.01604927	amu
^{3}He	3.016029319	amu
^{4}He	4.002602	amu

of 4.002602 amu. Table 5.1 shows some isotopes of low mass gases obtained from AWE on-line hydrogen isotope process monitoring and surveillance system manual.

Hydrogen isotopes

The isotopes of the element hydrogen are protium, deuterium, and tritium. They are distinguished by the difference in the number of neutrons. Figure 5.7 shows the isotopes of hydrogen element. Hydrogen has no neutron with an atomic weight of 1.007825 amu, deuterium has one with 2.014101779 amu, and tritium has two neutrons with an atomic weight of 3.01604927 amu.

Helium isotopes

Figure 5.8 shows the helium atom consists of a nucleus comprising of two positively charged protons and two uncharged neutrons, orbited by a two negatively charged electrons. Helium is the second lightest element after hydrogen and is less dense than air by about one seventh. Natural helium has two stable isotopes helium-3 (^3He) and helium-4 (^4He). The isotopes 5 through 10 are exotic isotopes that are radioactively unstable and they are extremely short lived. The stable isotopes of helium: ^3He has two protons and one neutron and ^3He has two protons and two neutrons. Figure 5.9 shows the natural helium isotopes (helium-3 and helium-4).

$_{1}^{1}\text{H}$ $_{1}^{2}\text{H}$ $_{1}^{3}\text{H}$

Protium   **Deuterium**   **Tritium**

1 Proton   1 Proton   1 Proton

0 Neutron   1 Neutron   2 Neutron

Neutrons = 1 - 1   # Neutrons = 2 - 1   # Neutrons = 3 - 1
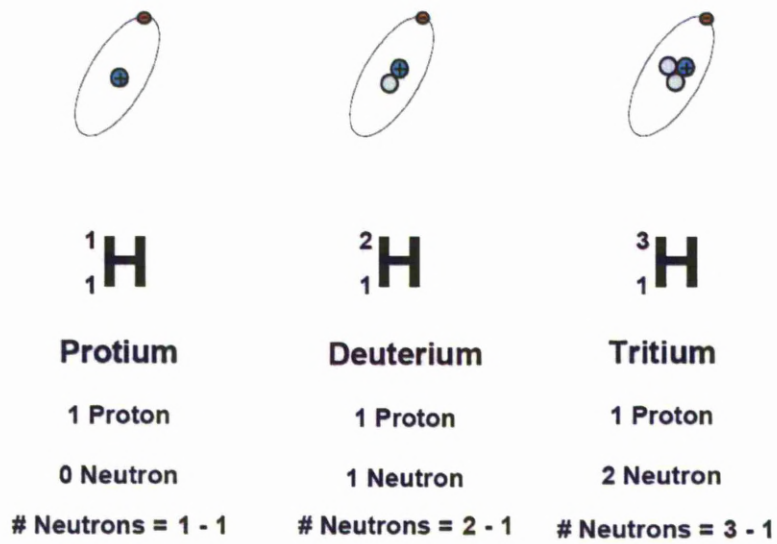
Figure 5.7: Hydrogen isotopes.

⊕ Proton

◯ Neutron

⊖ Electron
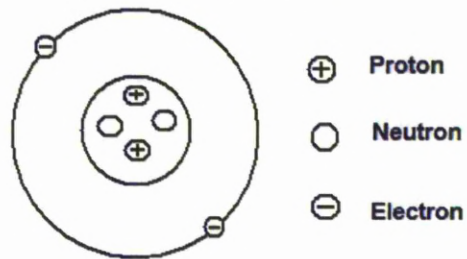
The Helium Atom

Figure 5.8: Helium atom.

^{3}He ^{4}He

● Proton   ◯ Neutron   ● Electron
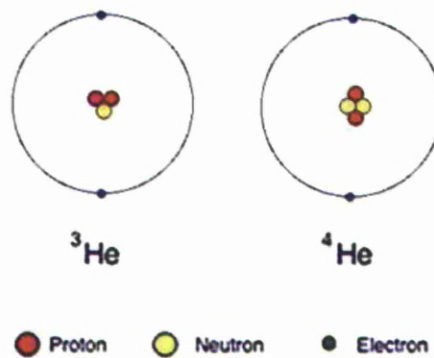
Figure 5.9: Natural helium isotopes.
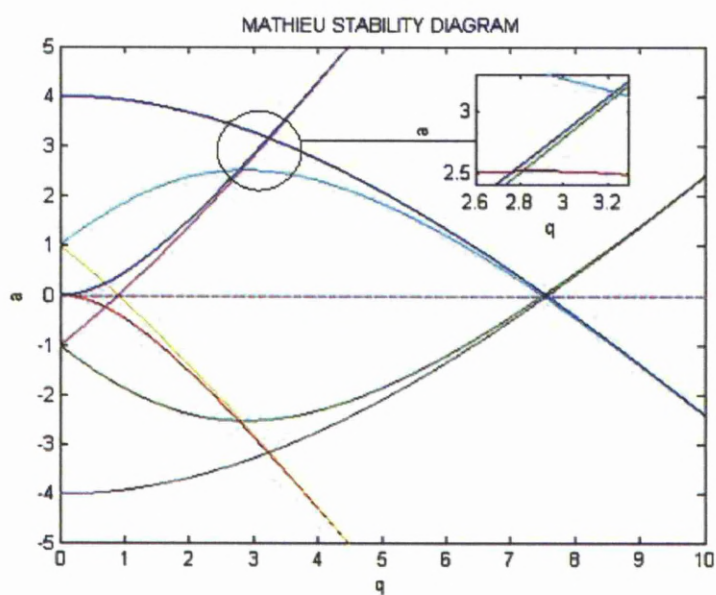
Figure 5.10: Mathieu stability diagram with Zone 3 detail shown in the inset.

Table 5.2: Mathieu coefficient values for Zone 1 and Zone 3

ZONE	a_{tip}	q_{tip}
1	0.237	0.706
3 (upper)	3.16	3.23
3 (lower)	2.52	2.82

5.2 Stability Zone 3

Figure 5.10 shows the Mathieu stability diagram which provides a graphical representation of the zones of the stable and unstable areas. This diagram shows the lowest three operating zones. Zone 1 (a = 0.237, q = 0.706) and Zone 3 (a = 3.16, q = 3.23) are examined for the purpose of this study. Table 5.2 shows Mathieu coefficient values for Zone 1 and Zone 3.

As described previously, the amplitudes of U and V are determined by the stability zone, the frequency, the ion mass and the r_0 of the quadrupole mass spectrometer (QMS). The effects of these operating parameters on the voltage V are presented graphically in the Figure 5.11.
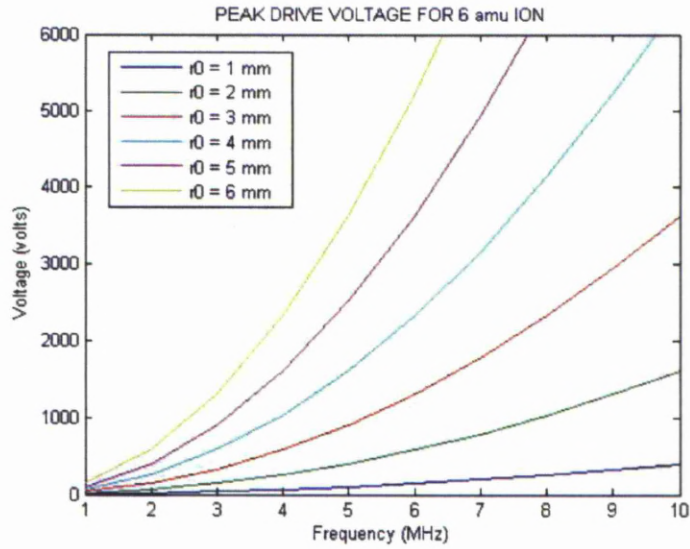
Figure 5.11: Variation of *RF* voltage with *RF* frequency and r_0, for a 6 amu ion in Zone 3.
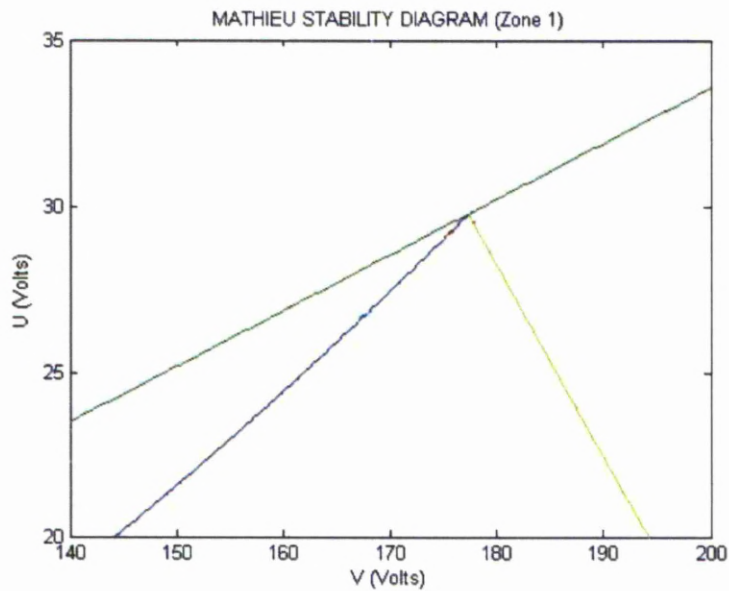
Figure 5.12: Detail stability Zone 1 showing a mass scan line that touches the apex of the stability diagram.
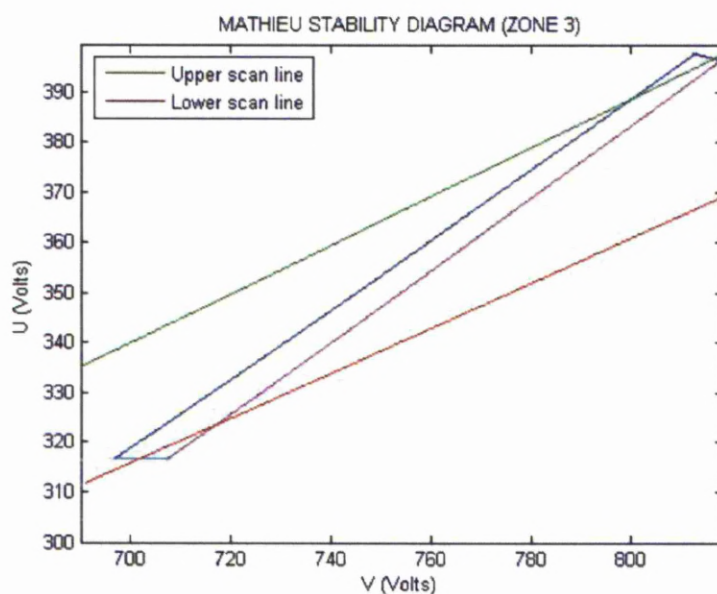
Figure 5.13: Detail of stability Zone 3 showing mass scan lines for the upper and lower corners.

The mass filtering action of the quadrupole mass filter (QMF) is controlled by varying the $U(DC)$ and $V(RF)$ voltages. The voltage V sets the position on the mass scale and the ratio of the U and V voltages controls the instrument resolution setting. Varying V and therefore U (while keeping the ratio of U to V constant) changes the m/z value that can successfully pass through the filter. This variation of the voltages is called the mass scan line. An instrument resolution of 100% represents a scan line that touches the apex of the stability diagram. It is normal to operate with a scan line of little lower than this to obtain an acceptable sensitivity, the exact position being a compromise between the required resolution and sensitivity. Figure 5.12 shows the detail of stability Zone 1 showing a mass scan line that touches the apex of the stability diagram and Figure 5.13 shows the detail of stability Zone 3 showing mass scan lines for the upper and lower corners. These plots are simulated using Liverpool University QMS2 model.

5.2.1 Mass discrimination

For each ion m/z value there is a unique stability diagram, which provides the mechanism for selective mass filtering. To achieve mass discrimination, it is necessary to set the mass scan line such that only one mass value can successfully pass through the filter at a time. Figure 5.14 demonstrates the effect of different instrument resolution settings of the mass scan line for stability Zone 3. For the initial position (Figure 5.14a), adequate resolution and sensitivity is provided, with good separation between the species. For the second position (Figure 5.14b), the resolution is decreased with increased sensitivity but the separation between the species is marginal. In the third position (Figure 5.14c), the resolution has been reduced to a point where there is significant overlap between the stable zones of the two species. In this position, adequate mass discrimination may not occur.

5.3 A *QMS* instrument for low mass isotopes

Most commercial QMS utilize a QMF based on circular rods and operate in stability Zone 1 (a = 0.237, q = 0.706) [20]. A scan line that provides a mass resolution that increases linearly with m/z and commonly referred to as unit resolution is the default mass scanning mode. There are a number of applications that require a high resolution at the lower end of the m/z range, i.e. 1 - 6 amu, where 1 atomic mass unit (amu) = 1.6605×10^{-27} kg [59]. Example applications include the quantitative measurement of hydrogen isotopes in the presence of helium [36] [49] [50] [39] and helium leak detection in a deuterium rich atmosphere [51]. For instance, to measure $^3He^+$ in the presence of HD^+ requires a minimum baseline resolution of 512 and for HT^+ in the presence of D_2^+, 930 is required [111]. These resolutions are not readily achievable with commercial instruments suitable for deployment in a process environment. A list of hydrogen and helium isotopes and the resolutions (taken 10% peak height) to separate adjacent species is contained in Table 5.3.
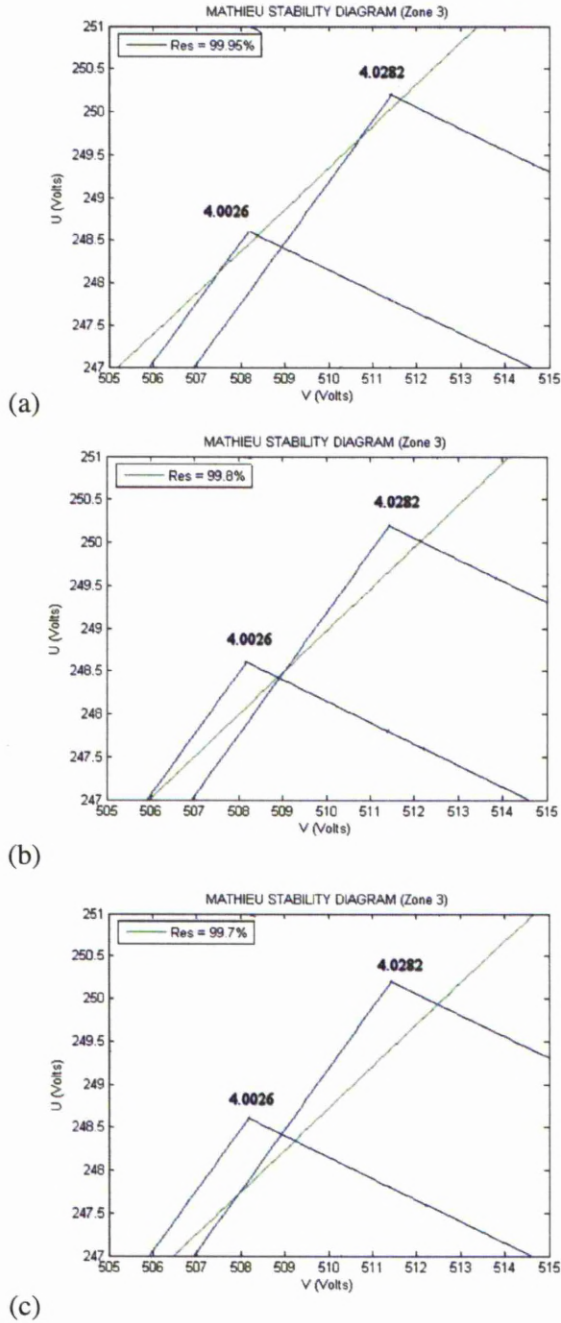
Figure 5.14: Stability Zone 3 upper corner showing mass scan line through two adjacent mass stability zones for different settings (^4He 4.0026 amu and D_2 4.0282), a) with adequate mass peak separation, b) with zero separation, c) with mass peak overlap.

Table 5.3: Minimum resolution required to discriminate between each of the species present

Species		H_2^+	$^3He^+$	HD^+	$^4He^+$	HT^+	D_2^+	T_2^+
	Mass (amu)	2.01565	3.01602932	3.021926779	4.002602	4.02387427	4.0282036	6.03209854
		MINIMUM RESOLUTION						
H_2^+	2.01565	NA	3.0	3.0	2.0	2.0	2.0	1.5
$^3He^+$	3.016029319	2.0	NA	512.4	4.1	4.0	4.0	2.0
HD^+	3.021926779	2.0	511.4	NA	4.1	4.0	4.0	2.0
$^4He^+$	4.002602	1.0	3.1	3.1	NA	189.2	157.3	3.0
HT^+	4.02387427	1.0	3.0	3.0	188.2	NA	930.5	3.0
D_2^+	4.028203558	1.0	3.0	3.0	156.3	929.5	NA	3.0
T_2^+	6.03209854	0.5	1.0	1.0	2.0	2.0	2.0	NA

General purpose instruments are also arranged to have relatively large m/z ranges, 100-300 Th being common. These characteristics result in relatively coarse control of the mass step size, e.g. 64 mass steps/amu is common [24]. The ability to achieve high resolution quantitative measurements of closely spaced species requires a high number of data points or mass steps across the mass peaks. A small mass step size imposes a reduced maximum mass due to the finite dynamic range of digital to analogue (d/a) converters in the control electronics. This relationship has been demonstrated by Day [24] who used a modified QMS to successfully baseline separate $^4He^+$ and D_2^+. For a given length of QMF the resolving power is dependent on the number of RF cycles the ion is exposed to on its passage through the QMF [34]. Typically 200 RF cycles are required in Zone 1 to achieve a resolution of approximately 1000, but this maximum is dependent on the overall accuracy of the QMF (perfect electrodes positioning) and the drive electronics, with any inaccuracies reducing this value [34]. For a QMF length of 300 mm, an ion of m/z 2 with energy of 5 eV would be exposed to 75 cycles, and an ion of m/z 6 to 120 cycles. Clearly this is insufficient to achieve the required resolution described above, even with perfect electrode profiles, assembly and voltage accuracies.

Stability Zone 3 is a sloping rectangular area that provides two tips one at the lower right (a = 2.52, q = 2.82) and the second, at the upper left (a = 3.16, q = 3.23) corners that enable high resolution mass scanning to be achieved.

With Zone 3 the ions require exposure to a lower number of RF cycles to achieve the same resolution when compared with Zone 1 [34]. However due to the higher Mathieu coefficients associated with Zone 3, increased operating voltages are required. This, to some extent, is in this application mitigated by the limited maximum operating mass of 6 amu that is required for hydrogen isotope measurement. Due to the much narrower stability zone, the sensitivity of a Zone 3 operating instrument is reduced compared to a Zone 1 QMS, with a reduction of a factor of 50 for He^+ being quoted by Hiroki [48]. Hiroki also reported that the upper corner of Zone 3 was the most suitable for high resolution operation [50] but that the lower corner provided increased sensitivity.

Circular rods provide a more cost effective route to implementing a QMF but suffer from reduced performance when compared to hyperbolic rods. Computer simulation has shown that when operating in Zone 1, circular rods with $r/r_0 = 1.148$ suffer from increased peak width, lower transmission and low mass tailing than hyperbolic rods [40]. More recent work has shown that this is also true when values of $r/r_0 = 1.125$ to 1.127 are used, which have been shown to give a better approximation to the quadrupole field than $r/r_0 = 1.148$ [18] [33] [43].

Using the simulation programme QMS2, with 60 cycles of RF, a comparison of resolution at 10% peak height and transmission through QMS using filters as shown in Table 5.4. Performance degradation is further reduced when operating in Zone 3 [53].

Figures 5.15 and 5.16 show the computed mass spectra for a HT^+ and D_2^+ ion species respectively for circular rods with two values of r/r_0 and hyperbolic rods. All the simulations determined the QMS peak profiles with number of ions of 10^5 for single mass step at about 3.9 to 4.08 m/z different mass points. The computer simulation operating test conditions are shown in Table 5.5.
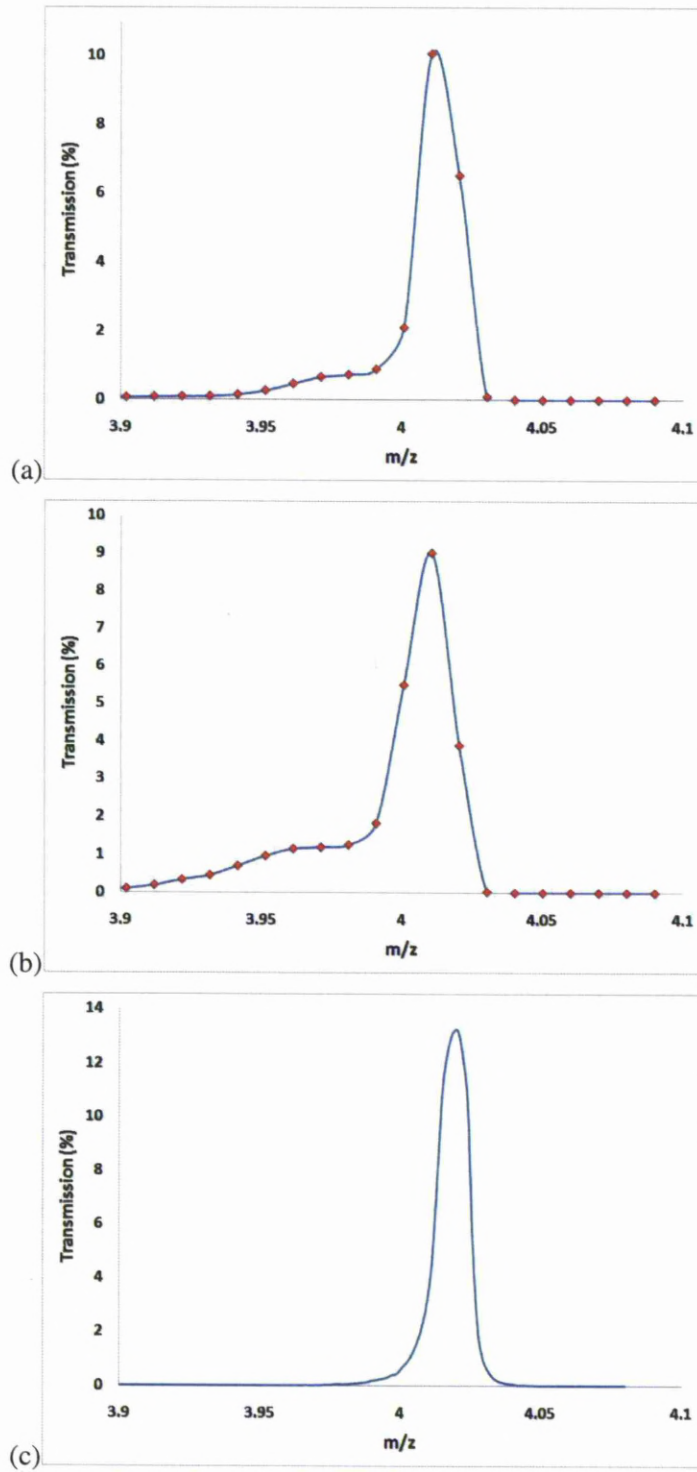
Figure 5.15: Computed mass spectrum for a HT^+ ion species in Zone 1, a) with circular electrodes of $r/r_0 = 1.127$, b) with circular electrodes of $r/r_0 = 1.148$, c) with hyperbolic electrodes
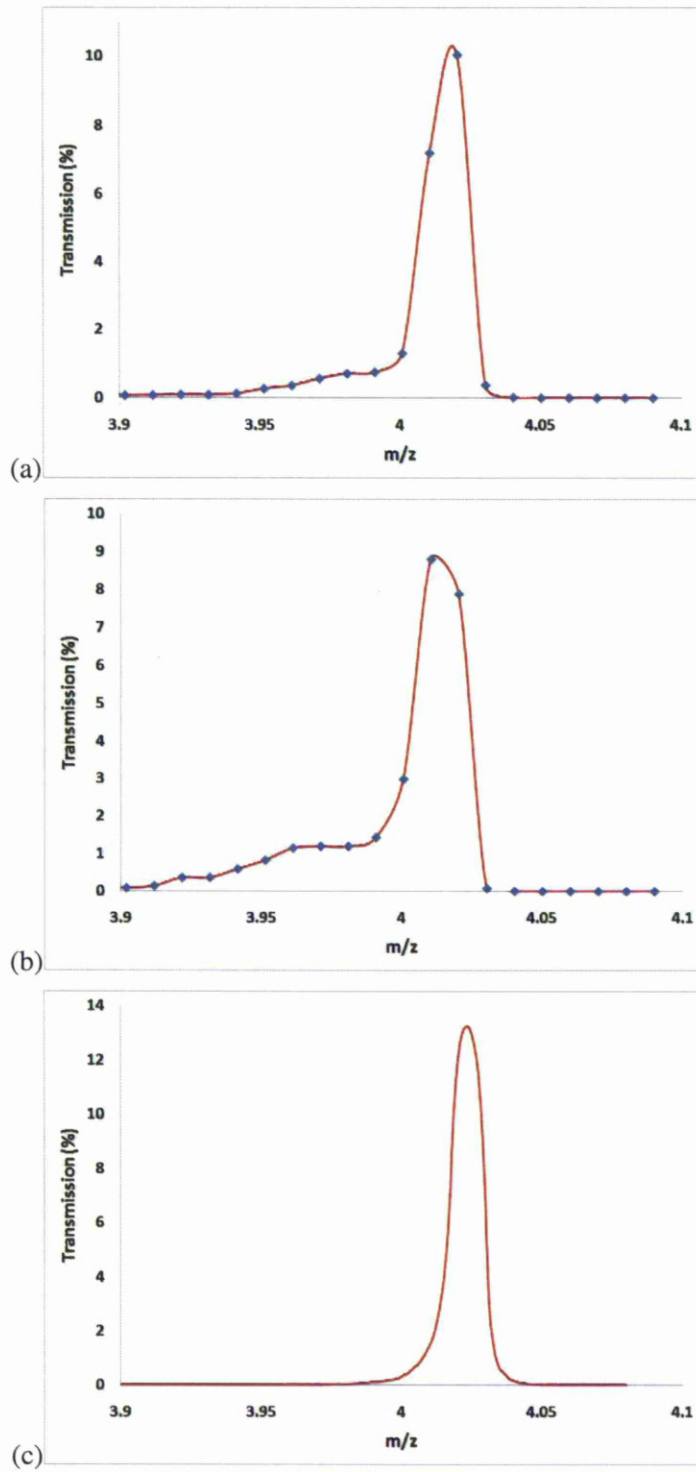
Figure 5.16: Computed mass spectrum for a D_2^+ ion species in Zone 1, a) with circular electrodes of $r/r_0 = 1.127$, b) with circular electrodes of $r/r_0 = 1.148$, c) with hyperbolic electrodes

81

Table 5.4: Comparison of *QMS* resolution and transmission for values of r/r_0 and hyperbolic electrodes (Zone 3)

r/r0	R(M/ΔM)	T (%)
1.148	50.64	8.81
1.127	101.28	10.06
Hyperbolic	159.54	13.21

Table 5.5: Computer simulation test conditions

QMF PARAMETER	CONDITION
Length	200 mm
r0	2.76 mm
Frequency	9.3 MHz
Detector radius	2.76 mm
Ion Source	
Ion energy	20 eV
Ion Source radius	0.55 mm
Ion energy spread	0
Ion angular spread	0
Ion Species	
HT+	4.0238 m/z
D2+	4.0282 m/z

The simulations show that the use of round rods instead of hyperbolic ones typically reduces the resolution by a factor of 2 and the transmission increases from 9% to 13% as we go from circular to hyperbolic.

Previous work in this laboratory [53] [52] has shown the factors which influence the ability of a QMS to achieve the performance necessary to separate HT^+ in the presence of D_2^+. Due to the demanding requirements of this application and for the reasons discussed above the use of circular electrodes was felt to be inadequate for the performance required and the results achieved in this work are based on a hyperbolic rod QMS. The following simulation results show that the product of (frequency) x (length) is a deciding factor in achieving the required resolution. It is also necessary for very accurate control of the mass scan line to ensure adequate abundance sensitivity. Furthermore it is shown that accurate alignment of the ion source to the QMF has to be achieved and this is more critical in the y-axis than in the x-axis due to the narrower shape of the y-stability area.

5.4 Simulation results and discussion

5.4.1 Mass spectral studies for a HT^+ and D_2^+ mixture

Reported are the simulated mass spectra for a HT^+ and D_2^+ mixture using the computer simulation software described earlier in Chapter 4 and operated at the upper left hand tip of stability Zone 3 ($a = 3.16$ and $q = 3.23$). For Zone 3, the amplitude and length of the high mass tail reduces as the frequency increases with corresponding improvement in abundance sensitivity. Increasing frequency also reduces low mass tail but the effect is minimal. As previously noted, hyperbolic electrodes provide superior performance in resolution and ion transmission for a given number of RF cycles than circular or other shaped electrodes, e.g. rectangular [90] [41]. The simulated performance characteristics of a QMF constructed from hyperbolic electrodes are therefore investigated. Tests indicate that only stability Zone 3 is capable of being able to achieve the desired

performance in the mass range in question (1-6 amu). The mass difference between the two species is 0.004329288 amu, requiring a minimum resolution of 930 for mass discrimination. Increasing the frequency improves the resolution measured at 10% of spectrum peak height (PH) and base line resolution, but the 50% PH resolution only increases for a limited range of frequencies before saturating. Due to the closeness of the two species, a higher resolution is required to separate HT^+ and D_2^+ ions. A higher resolution can be achieved only in the upper half of the Zone 3 stability area. This is due to the number of RF cycles that the two species experience being very similar. As the ion mass increases the velocity through the QMF falls (for a given ion energy), this gives an increase in the number of RF cycles experienced and an increase in achievable resolution.

Figure 5.17a shows mass spectra for HT^+, at 10% PH showing a resolution of 914 at 4 MHz, increasing to 1257 at 8 MHz. The corresponding 50% PH resolution ranges from 1749 at the low frequency end up to 1829 at 5 MHz and above. Figure 5.17b shows mass spectra for D_2^+ showing a slightly higher resolution: the 10% PH resolution ranges from 915 at the lowest frequency, up to a maximum of 1299 at 8MHz. The 50% PH resolution was also correspondingly greater, with a minimum 1751 at 4 MHz increasing to 1918 at 6 MHz and above. As was the case for HD^+ the 50% PH resolution limits, with the higher mass D_2^+ limiting at a slightly higher value than for the lower mass HD^+. Both the low and high mass tails for the two species are low, but with the high mass tail having much greater amplitude and mass range. A minimum resolution of 930 is required to separate these two species HT^+ and D_2^+. This is achievable with a length of 300 mm operating at a frequency of 5 MHz. By using the previous length and frequency relationship (Equation 1.2), this should also be achievable with a length of 250mm operating at 6 MHz.

Figure 5.18 shows the simulated mass spectra for equal abundances of HT^+ and D_2^+ in Zone 3. As previously discussed, the high mass tail is the more dominant. Therefore the high mass tail of the HT^+ mass peak is the most likely to be the cause of
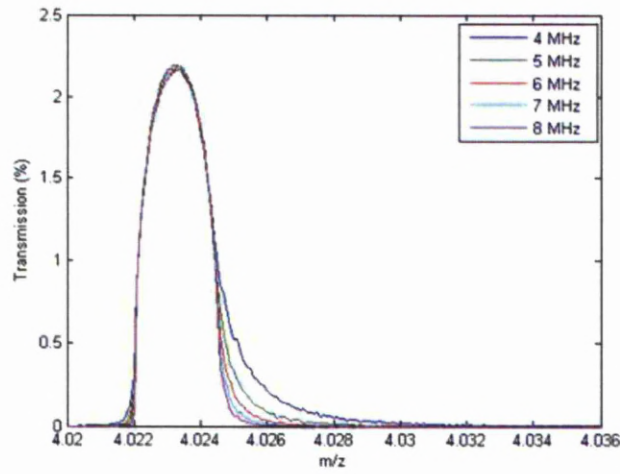
(a)
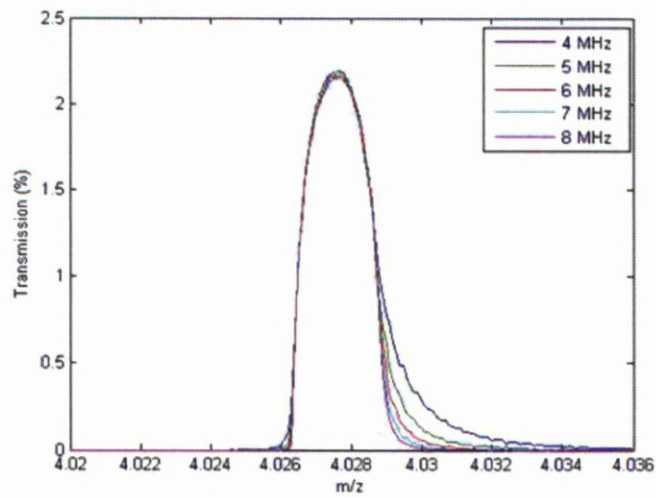
(b)

Figure 5.17: (a) Variation of HT^+ mass spectra with frequency for a hyperbolic electrode QMF in Zone 3(L = 300 mm, r_0 = 2.76 mm, E_i = 15 eV, ion source radius =0.276mm) and (b) variation of D_2^+ mass spectra with frequency for a hyperbolic electrode QMF (L = 300mm, r_0 = 2.76mm, E_i = 15eV, ion source radius = 0.276mm)
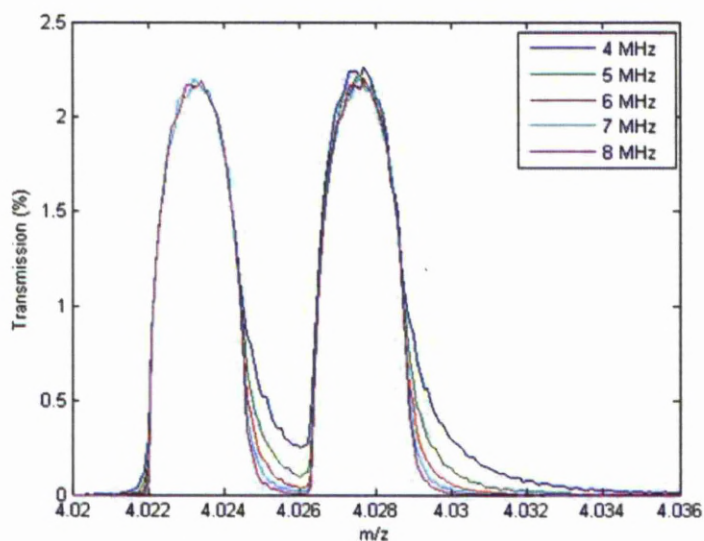
Figure 5.18: Variation of mass spectra with frequency for a hyperbolic electrode QMF in Zone 3 (L = 300 mm, r_0 = 2.76 mm, E_i = 15 eV, , ion source radius = 0.276 mm) for HT^+ and D_2^+ ions with equal abundance.

inter-species interference. The valley between the two peaks decreases with increasing frequency. At the lower frequency, the minimum point on the valley represents approximately 10% of peak height. For the highest frequency, this minimum drops to virtually zero.

Figure 5.19 shows typical mass spectra for D_2^+ for operation in Zone 1 using the computer simulation software described. The mass peaks show both low and high mass tails, which are well formed. In this case (Zone 1) the low mass tail is of greater amplitude and width than the high mass tail. The 10% PH resolution is significantly lower than obtained with Zone 3 simulations. The resolution at the low frequency end is 496, compared to 915 for Zone 3. As the frequency is increased, the difference in resolution between the two zones decreases. For the two higher frequencies in this mass range, Zone 1 achieves a maximum of 1751 at 8 MHz.
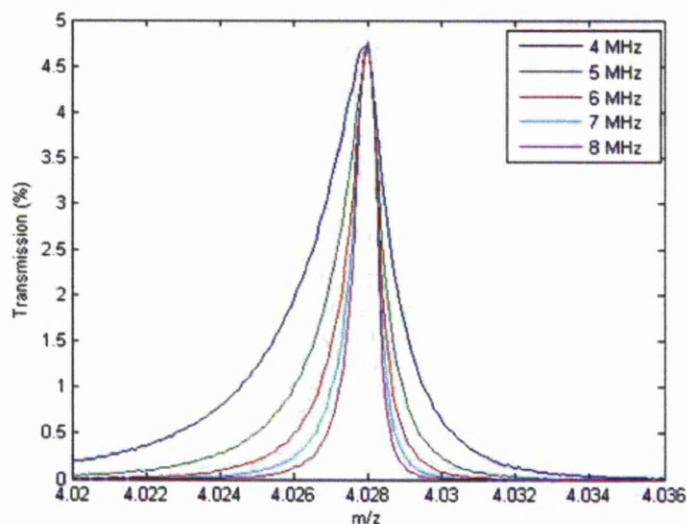
Figure 5.19: Variation of D_2^+ Zone 1 mass spectra (L = 300 mm, r_0 = 2.76 mm, E_i = 3 eV, ion source radius 0.276 mm for a range of RF frequencies.

5.4.2 Effects of drive voltage tolerance

Increasing the amplitudes of the U (DC) and V (RF) drive voltages while keeping the ratio between them constant produces a constant resolution mass scan line (resolution proportional to mass). To achieve unit resolution the ratio of U/V is varied with increasing mass and results in a more complex scan generation system. A shift in the mass scan line is observed as the ratio between the U (DC) and V (RF) voltages is varied, which in turn results in a change to resolution and/or the mass calibration of the system. A very high instrument resolution is achieved with the tight control of the drive voltages. Changes to either U or V independently results in a change to instrument resolution and small changes to peak shape results with minor changes to the inter peak valley shape. These small peak shape changes can occur due to small changes in the U voltage. A greater change in instrument resolution is produced as the tolerance limit increases the error in the ratio of U and V voltages and therefore increasing movement in the position of the scan line relative to the mass stability regions. This increased change in mass scan line position results in increasing distortion of the mass peak. As

87

this voltage error increases, the individual peaks widen with an accompanying increase in peak height. The inter peak valley amplitude increases finally disappearing with the two peaks merging.

Figures 5.20a and 5.20b show simulated mass spectra for a HT^+ and D_2^+ mixture (50:50 ratio) for a range of negative U drive voltage errors. Normally a reduction in DC drive voltage (negative voltage error) due to the power supply tolerances results in an increase in ion transmission and a broadening of the mass peak, resulting in a reduction in resolution. At the lower end of the voltage error range considered (up to -0.025 V) the observable changes in the mass peak are minimal and acceptable. Above this value, the valley between the two species rises resulting in discrimination at 10% PH becoming unachievable, and at a voltage error of -0.1 V the stability zones for the two species merge with the resultant superimposed peak emerging. At the negative voltage error of -0.1 V, the resolution has been reduced to a point where there is significant overlap between the stable zones of HT^+ and D_2^+ species. This results in poor mass discrimination. For this position of the mass scan line, both low and high mass species are transmitted, resulting in higher transmission accompanied by the appearance of the central peak. The drive voltage tolerance limit is clearly at its most stringent at this part of the mass scan range due to high resolution required to discriminate between HT^+ and D_2^+. To maintain this performance, it is necessary to control the U/V ratio to very tight limits. The tolerance limits depend on the achievable mass resolution limit that can be obtained from the instrument.

5.4.3 Ion source potential displacements

Previous research has characterised the dependence of QMF performance on electrode positional tolerance [109]. The degradation in performance that occurs for a range of QMF-to-ion source misalignments is discussed here. Correct alignment of the ion source with the central axis of the QMF is important to ensure maximum sensitivity. Misalignments of less than 0.2mm (for an r_0 of 2.76mm) result in a small reduction
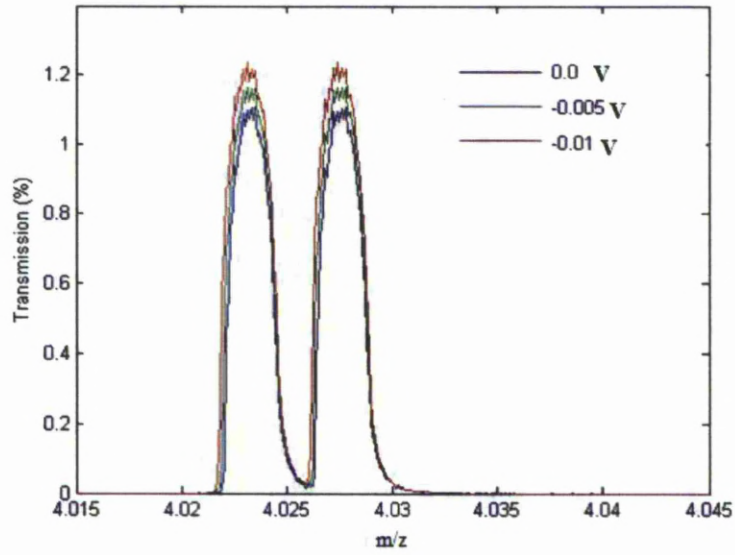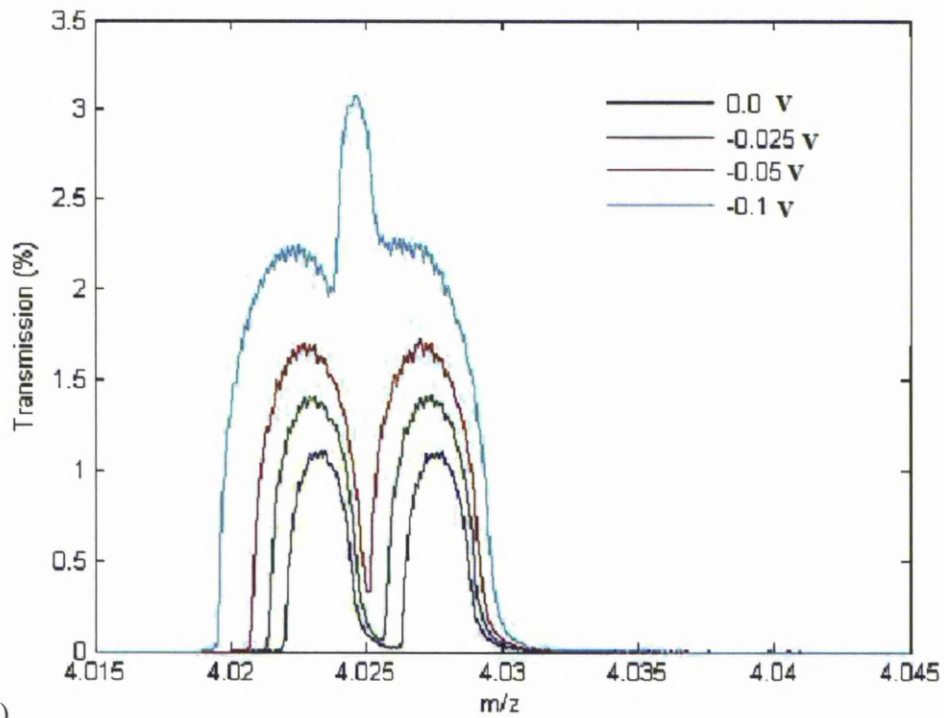
Figure 5.20: Simulated mass spectra for a HT^+ and D_2^+ mixture (50:50 ratio) for a range of U voltage acceptable tolerances (v) in Zone 3 a) acceptable tolerances b) unacceptable tolerances.

in the peak height (sensitivity) with barely discernible changes of the peak shape. For increasing misalignments, the peak heights start to decrease significantly, decreasing by a factor of greater than 2 for a displacement of 0.4mm, associated with an increasing narrowing of the peak width. Similar effects are observed for both x- and y-axis displacements. The y-axis displacement results in greater decrease in peak height reflecting the narrower y-axis stable region of the QMF. Also it is demonstrated that the effects of simultaneous x- and y- displacements are cumulative.

Figures 5.21(a) and 5.21(b) show simulated mass spectra for a HT^+ and D_2^+ mixture (50:50 ratio) for a range of x- and y-axis displacement of the ion source with respect to the QMF axis. Both x- and y- displacements exhibit similar characteristics, with the y-axis displacement having the greater decrease in transmission for a given displacement. Displacement in the positive direction resulting in a similar effect that has confirmed this behaviour, and is due to the asymmetry of the QMF acceptance. For the conditions tested, a tolerance of +/- 0.2mm would probably be acceptable. The effect of the fringing fields is not reported here. This is the subject of continuing work requiring three dimensional modelling of the ion injection and extraction process from the QMF.

5.5 Conclusions

To provide adequate mass discrimination to resolve the peaks of hydrogen and helium isotopes presents certain difficulties. Due to their low mass, these isotopes have a relatively high velocity, which results in them experiencing a low number of RF cycles in their passage through the QMF and results in poor mass resolution with the standard QMS. The use of hyperbolic electrodes is the best option to maximise the theoretical resolution which is necessary for this application.

Simulation results show that the use of hyperbolic electrodes in conjunction with operation in stability Zone 3 provides resolutions greater than 1000, which exceeds
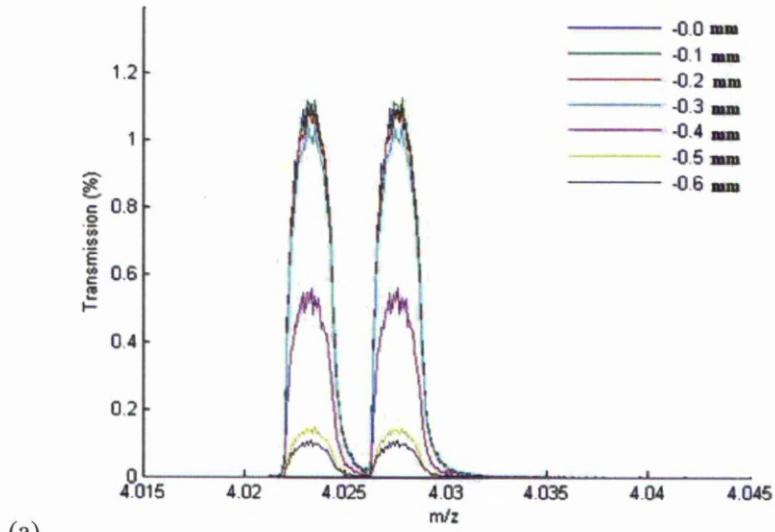
(a)
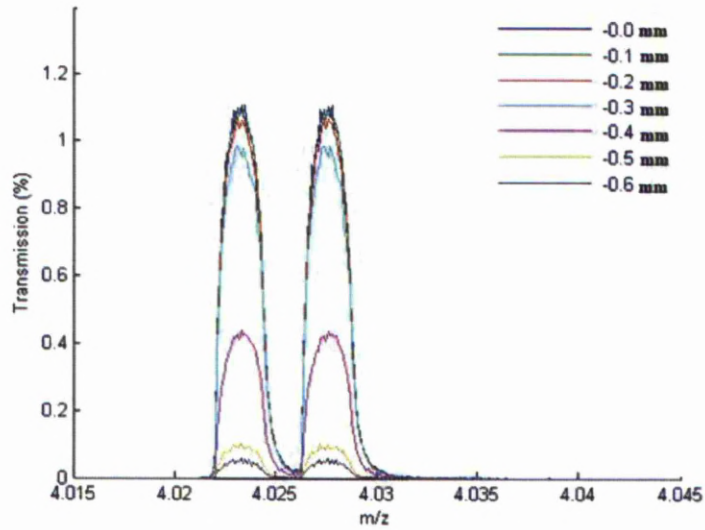
(b)

Figure 5.21: Simulated mass spectra for a HT^+ and D_2^+ mixture (50:50 ratio) for a range of QMF to ion source alignment tolerances (mm) (L = 300mm, F = 6 MHz, r_0 = 2.76 mm, R_s = 0.4 mm, E_i = 15 eV) (a) *x* axis misalignment and (b) *y* axis misalignment.

the minimum required performance criteria for separation of HT^+ and D_2^+ given in the introduction. The closeness in mass of the species discussed demands high resolution to achieve mass discrimination and to achieve adequate abundance sensitivity. This places tight constraints on the tolerance budget for the control electronics of the electrode drive system. The high mass tail has a greater effect than the lower mass tail on abundance sensitivity for these two species. A tighter control of the QMF-to-ion source alignment accuracy is required with respect to the y- axis compared to the x- axis due to the narrower y- axis stability area. The results show that there is scope to optimize the choice of QMF length and drive frequency. The simulation results described in this chapter remain to be demonstrated experimentally, and this is the subject of ongoing work.

Chapter 6

DEVELOPMENT OF AN ELECTRON IMPACT ION SOURCE MODEL INCLUDING PRESSURE DEPENDENCE

In Chapter Four, details of the computer simulation software developed to study the performance of quadrupole mass spectrometer (QMS) for a hyperbolic rod quadrupole mass filter (QMF) are presented. One of the application programs in the software, $QMS2$-Ion holds data and text files which has the information of ion energy, ion source radius, ion energy spread, ion beam spread and filename prefix. $QMS2$-Ion generates a large number of individual ion start conditions but does not support the calculation of the ionic current entering the QMF.

This chapter involves the use of an electron impact (EI) ion source model, which includes pressure dependence to solve the ionic current expression and takes the value of the differential ionisation cross-section of a gas component in the ionic current expression from the values generated using the Binary-Encounter-Bethe (BEB) theory for different electron energies. This allows simulated mass spectra to be determined

93

which include the effects of electron emission current, ionic current, electron energy, and pressure.

6.1 General theory of impact phenomena

Early research work has directed the way of understanding the microscopic nature of matter through the study of the impact phenomena of beams of particles and photons on surfaces. Discovery of the nucleus by Rutherford was made by studying the scattering of a beam of α particles as they passed through thin foils. The confirmation of de Broglie matter-waves was made by observing the diffraction of a beam of electrons by crystalline targets. Much recent research work relies upon impact ionisation phenomena.

When an electron makes a collision with an atom, three possible collisions may results. They are,

1. Elastic collision

2. Inelastic collision

3. Superelastic collision

In an elastic collision, no energy transfer takes place between the internal motion of the atom and the kinetic energy of the electron. In an inelastic collision, some energy transfer takes place between the internal motion of the atom and the kinetic energy of the electron. An inelastic collision is further distinguished into ionising and non-ionising inelastic collisions. In the case of ionising impact, the ionisation of an atom depends on the kinetic energy required to eject one or more electrons from the atom. Non-ionising inelastic collision can occur in which distinct atomic states are excited so that the atom is ionized by the impact. In superelastic collision, an electron gains energy from the internal motion of the atom as it collides with an excited atom.

The wavelength of the incident species can be observed by the nature of the inter-action between a particle and a target. The wavelength of a particle is given by the de Broglie relation [17]

$$\lambda_1 \quad = \quad \frac{h}{\sqrt{2mE_n}} \tag{6.1}$$

where h is Planck's constant, m is the mass of the particle, and E_n is its discrete energy.

If the wavelength of a particle is much larger than the interatomic distance, then the incident particle interacts the target atoms at the same time resulting in a large number of fragment particles.

6.1.1 Scattering from a Coulomb potential

Charged particles traveling through a target material will feel a Coulombic repulsion or attraction between the electrons and nuclei in the material. Because materials are typically macroscopically neutral, it is assumed that long-range interactions are screened, and that only individual classical two-particle collisions are significant. [106].

Low-mass particles scattering from heavy target particles will transfer very little energy. Large scattering angles are possible, and scattering behavior can be determined from the relation of the impact parameter to the scattering angle.

Figure 6.1 shows the relationship between the differential cross-section and impact parameters [37].

Consider the particles incident with impact parameters lying between b and b +db. The number of such particles passing through the associated transverse area $2\pi bdb$ per unit time is given by $2\pi bdbF_1$ where, F_1 is the particle force. The differential elastic scattering cross-section for all the particles passing through the ring of area $2\pi bdb$ scattered through the angle θ is given by [37]

$$F_1 2\pi bdb \quad = \quad F_1 d\sigma_{el}(\theta) \tag{6.2}$$

Consider that the particles entering the original ring all emerge through the area

95
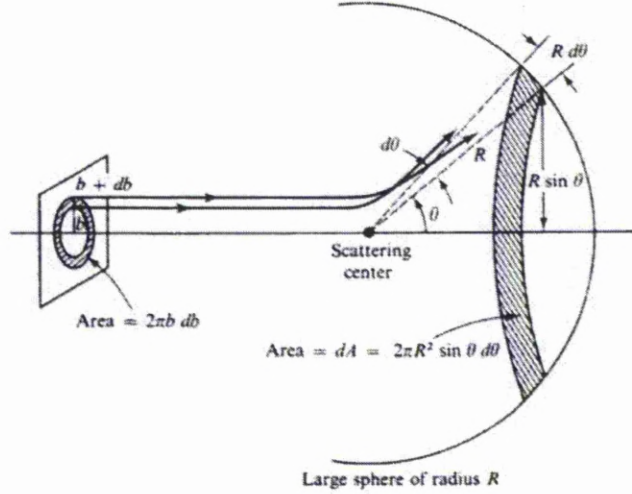
Figure 6.1: Relationship between the differential cross-section and impact parameter

$dA = 2\pi R^2 sin\theta d\theta$. The corresponding solid angle $d\Omega$ into which the particles are scattered is given by

$$d\Omega = \frac{dA}{R^2} = 2\pi \sin\theta d\theta \qquad (6.3)$$

where R is the radius of sphere and θ is the polar angle measured from the incident direction.

By multiplying and dividing the right-hand side of equation (6.2) by $d\Omega$

$$F_1 d\sigma_{el}(\theta) = F_1 \left(\frac{d\sigma}{d\Omega}\right)_{el} d\Omega \qquad (6.4)$$

By solving the equations (6.3) and (6.4) we get the differential cross-section for unit final solid angle

$$\left(\frac{d\sigma}{d\Omega}\right)_{el} = \frac{b}{\sin\theta}\left|\frac{db}{d\theta}\right| \qquad (6.5)$$

The total cross-section is given by integrating all solid angles.

$$\sigma_\tau = \int d\Omega \left(\frac{d\sigma}{d\Omega}\right)_{el} \qquad (6.6)$$

A particle with mass m and charge ze scattering from a particle of mass M and charge Ze will satisfy the following equation

96

$$\mu \ddot{r} = zZe^2 \frac{r}{r^3} \tag{6.7}$$

where μ is the reduced mass, r is the vector from the scattering center to the incident particle.

The reduced mass μ is given by

$$\frac{mM}{M+m} \tag{6.8}$$

The relationship between the impact parameter b and the scattering angle θ is given by

$$b = \frac{|zZ|e^2}{\mu v^2} \cot \frac{\theta}{2} \tag{6.9}$$

where v is the velocity of the incident particle. An attractive potential would draw the particle down rather than push it up, but the scattering angle would be the same.

Substituting the equation (6.9) in equation (6.5), we get the differential cross-section as

$$\frac{d\sigma}{d\Omega} = \left[\frac{zZe^2}{4E \sin^2 \left(\frac{\theta}{2} \right)} \right]^2 \tag{6.10}$$

where E is the kinetic energy of the incident particle. If the scattering center is much more massive than the incident particle, then the incident energy is approximately equal to the laboratory energy. The above derivation is extremely useful to explain the scattering of light particles by heavy particles. The scattering of heavy particles by a light particle will effect the direction of the former only slightly and the amount of energy transfer between the particles is an interesting parameter to be considered.

Consider that the heavy particle does not deflect at all when it interacts with the lighter target, which results in negligible movement. Therefore the net impulse in the direction of travel is zero. By integrating the Coulomb force, the momentum of transfer p in the perpendicular direction Δ is given by

$$\Delta p = \frac{2zZe^2}{bv} \tag{6.11}$$

Therefore, the transferred energy ΔE is given by

$$\Delta E = \frac{\Delta p^2}{2m} = \frac{mz^2 Z^2 e^4}{M b^2 E} \tag{6.12}$$

The kinetic energy in terms of the velocity of the incident particle is given by

$$E_p = \frac{1}{2}mv^2 \Rightarrow v^2 = \frac{2E_p}{m} \tag{6.13}$$

From equation (6.12) the impact parameter in terms of the transferred energy can be found and the differential cross-section may be written in terms of the energy transfer

$$d\sigma = \frac{\pi m z^2 Z^2 e^4}{M E_p \Delta E^2} d\Delta E \tag{6.14}$$

6.1.2 Electron impact

The interaction of a beam of electrons impinging on a solid or liquid target can be modeled to a good approximation by classical two-particle scattering from target electrons. Although the masses of the incident particle and target particle are identical, the impulse approximation applies if the energy of the incoming electron is sufficiently high [106]. Here, the change in momentum Δp and thus the change in energy ΔE as a function of impact parameter b reduces to

$$\Delta p = \frac{2e^2}{bv} \Rightarrow \Delta E = \frac{e^4}{E b^2} \tag{6.15}$$

where e is the electron charge, v is the velocity of the incident charge, and E is the energy of the incident electron in electron volts.

The differential cross-section is given by

$$d\sigma(E) = -2\pi b db = \left(\frac{\pi e^4}{E \Delta E^2}\right) d\Delta E \tag{6.16}$$

A particular transition with energy E_t is obtained by integrating the above equation

$$\sigma = \pi \frac{e^4}{E}\left(\frac{1}{E_t} - \frac{1}{E}\right) \tag{6.17}$$

If the beam energy is much greater than the transition energy, the cross-section simplifies to the following equation

$$\sigma \cong \frac{\pi e^4}{E E_t} \tag{6.18}$$

The transition from a valence-band electron to the conduction band results in an electron-hole pair, or a bound core electron could be rejected from a gas phase. This transition corresponding to the E_t could occur from a bound state, valence-band state, or conduction-band state to any higher energy state.

The rate of energy loss as a function of distance traveled in the target is obtained by integrating energy times the differential cross-section

$$-\frac{dE}{dx} = \frac{2\pi e^4 n_e}{E} \ln\left(\frac{E}{E_t}\right) \tag{6.19}$$

where n_e is the density of electrons in the initial state. Since energy can only be transferred in discrete amounts, the mean free path can be estimated from the rate of energy loss which is given by

$$\frac{1}{\lambda} = -\frac{m\omega e^2}{2\hbar E} \ln\frac{4E}{\hbar\omega} \tag{6.20}$$

where m is the mass of the electron. It is to be noted that the differential cross-section and hence the mean free path depends on the energy of the incident particle. After each collision, the particle loses energy and hence the equation for the mean free path is given by

$$R = \left(\frac{K}{\rho_m}\right) E^{\gamma_n} \tag{6.21}$$

where ρ_m is the density of the material in grams per cubic and K and γ_n are constants. The constant K is dependent on the material's density and the atomic weight. The value of K is approximately 0.064 for all materials. The constant γ_n depends on the target material and its value typically lies between 1.2 and 1.7.

6.2 Cross-section theories

6.2.1 Rutherford cross-section

The collision of a particle with charge $Z_1 e$ with a free electron at rest is described by the Rutherford cross-section[94],[69]

$$\frac{d\sigma(W,T)}{dW} = \frac{4\pi a_0^2 Z_1^2 R^2}{T} \frac{1}{W^2} \tag{6.22}$$

where W is the kinetic energy of the ejected electron, a_0 is the Bohr radius ($= 5.29 \times 10^{-11} m$), R is the Rydberg energy ($= 13.6$ eV), and T is the reduced kinetic energy given by

$$T = \frac{ms^2}{2} \tag{6.23}$$

with the relative speed s and the electron mass m regardless of the actual mass of the projectile. For incident electrons, T is the non-relativistic kinetic energy.

6.2.2 Mott cross-section

A generalized equation for the energy distribution of the ejected electron from the Rutherford cross-section is given by [63]

$$\frac{d\sigma(W,T)}{dW} = \frac{4\pi a_0^2 R^2}{T} \left[\frac{1}{W^2} - \frac{1}{W(T-W)} + \frac{1}{(T-W)^2} \right] \tag{6.24}$$

where T is the kinetic energy of the incident electron, and $T - W$ is the kinetic energy of the scattered electron.

In the above equation, the first term in the square bracket represents the direct collision term, the second term is the interference between the direct and exchange collision terms, and the third term is the exchange collision term.

In the case of electron-electron collision, both the Rutherford and the Mott cross-sections diverges when the kinetic energy of the ejected electron, W approaches zero

or when W reaches the kinetic energy of the incident electron, T. In a real atom, the energy distribution of the incident electron is always finite with $W = 0$ and W cannot be equal to T.

The energy transfer is given by the following equation

$$E \;=\; W + B \tag{6.25}$$

where B is the binding energy. By replacing W by the energy transfer, the modified Rutherford cross-section is given by

$$\frac{d\sigma(W,T)}{dW} \;=\; \frac{d\sigma}{dE} \;=\; \frac{4\pi a_0^2 Z_1^2 N}{T}\frac{R^2}{E^2} \tag{6.26}$$

Substituting equation (6.25) in (6.26)

$$\frac{d\sigma(W,T)}{dW} \;=\; \frac{d\sigma}{dE} \;=\; \frac{4\pi a_0^2 R^2 N}{T}\left[\frac{1}{E^2} - \frac{1}{E(T-W)} + \frac{1}{(T-W)^2}\right] \tag{6.27}$$

6.2.3 Binary encounter cross-section

The ionisation and excitation of atoms by electrons is well explained in the binary-encounter collision theory. An extension of the Mott cross-section, binary encounter cross-section theory further assumed that the atomic electrons initially have an isotropic velocity-direction distribution with one constant magnitude of the velocity [118].

The Binary encounter cross-section is given by:

$$\frac{d\sigma(E,T)}{dE} \;=\; \frac{4\pi a_0^2 R^2 N}{T + U_i + B}\left\{\frac{1}{E^2} - \frac{1}{E(T-W)} + \frac{1}{(T-W)^2}\right.$$
$$\left. + \frac{4U}{3}\left[\frac{1}{e^3} + \frac{1}{(T-W)^3}\right]\right\} \tag{6.28}$$

where U_i is the average kinetic energy and is given by

$$U_i \;\equiv\; \frac{\langle \vec{p}^2 \rangle}{2m} \tag{6.29}$$

where p is the momentum operator of the electrons in a subshell

By substituting the energy variables in units of the binding energy B of the electrons, the modified Mott cross-section is given by

$$\frac{d\sigma(W,T)}{dW} = \frac{d\sigma(w,t_n)}{Bdw}$$

$$= \frac{S}{Bt_n}\left[\frac{1}{(w+1)^2} - \frac{1}{(w+1)(t_n-w)} + \frac{1}{(t_n-w)^2}\right] \quad (6.30)$$

Similarly the modified binary encounter cross-section is given by

$$\frac{d\sigma(W,T)}{dW} = \frac{S}{B(t_n+u+1)}\left\{\frac{1}{(w+1)^2} + \frac{1}{(t_n-w)^2} - \frac{1}{(w+1)(t_n-w)}\right.$$

$$\left. + \frac{4u}{3}\left[\frac{1}{(w+1)^3} + \frac{1}{(t_n-w)^3}\right]\right\} \quad (6.31)$$

where t_n, w, u, and s are given as follows

$$t_n = \frac{T}{B} \quad (6.32)$$

$$w = \frac{W}{B} \quad (6.33)$$

$$u = \frac{U_i}{B} \quad (6.34)$$

$$S = 4\pi a_0^2 N\left(\frac{R}{B}\right)^2 \quad (6.35)$$

6.2.4 Binary encounter dipole model

Binary-Encounter-Dipole (*BED*) model developed by Kim and Rudd [63] combines the modified form of the Mott cross-section [118] and the high-incident-energy behavior of the Bethe Theory [56] [57] to provide an approach to calculate single differential and total ionisation cross-sections. The BED model solves the Mott cross-section with the leading dipole part of the Bethe cross-section and provides the differential ionisation cross-section by *EI* as a function of the secondary electron energy W and the incident electron energy [63], [94].

The total ionisation cross-section is given by

$$\sigma_i = \int\left(\frac{d\sigma}{dW}\right)dW \quad (6.36)$$

where $d\sigma/dW$ is the singly differential cross-section and W is the ejected electron energy.

102

The stopping power can be evaluated using the stopping cross-section [56]

$$\sigma_{stop} = \int (W+B) \left(\frac{d\sigma}{dW} \right) dW \qquad (6.37)$$

where B is the binding energy of the ejected electron

The energy loss of the incident electron is given by

$$E = W + B \qquad (6.38)$$

where B (binding energy) is a constant for a given orbital and hence the continuum dipole oscillator strength df/dE, can replace df/dW. The continuum dipole oscillator strength occurs due to the prediction of the dominance of dipole interaction in electron ionisation at large values of T/B [56].

The term df/dE is used for the ejection of electron by photoionisation in each atomic orbital which is the total cross-section, from which the differential cross-section can be calculated. The BED model helps in the calculation of both the differential and the total ionisation cross-section in each atomic orbital, and hence df/dE is used in the model. According to the BED model, the ionisation cross-section of an atomic orbital with a binding energy B, the average kinetic energy $U_i = \langle p^2/2m \rangle$, where p and m are the momentum and electron mass, respectively, is given by

$$\sigma_{BED}(t_n) = \frac{S}{t_n + u + 1} \left[D(t_n) \ln t_n + \left(2 - \frac{N_i}{N} \right) \left(\frac{t_n - 1}{t} - \frac{\ln t_n}{t_n + 1} \right) \right] \qquad (6.39)$$

where

$$t_n = \frac{T}{B}$$

$$u = \frac{U_i}{B}$$

$$S = \frac{4\pi a_0^2 N R^2}{B^2}$$

$$D(t) \equiv N^{-1} \int_0^{(t_n-1)/2} \frac{1}{w+1} \frac{df(w)}{dw} dw \qquad (6.40)$$

with $w = W/B$.

103

$$N_i \equiv \int_0^\infty \frac{df(w)}{dw} dw \qquad (6.41)$$

In the equation (6.39), the first logarithmic term gives the dipole interaction predicted by the Bethe theory, the last logarithmic term represents the interference between the direct and exchange interactions described by the Mott cross-section, and the term $(t_n - 1)/t$ arises from close collisions with large momentum transfers between the incident and ejected electrons.

6.3 Binary-Encounter-Bethe model

The *BEB* model is a simplified version of the *BED* model. The *BEB* theory is specifically designed for electron ionisation which occurs in an *EI* ion source used in a *QMS*.

The "DM formalism" [28] [96] is the most successful semi-empirical procedure for calculating *EI* cross-sections as a function of incident electron energy. A model built without any empirical parameters is the *BEB* model [63].

The *BED* model developed above requires explicit knowledge of dipole oscillator strength df/dE for ejection of each target electron. By using a simple approximation for dipole oscillator strength, the *BEB* model was developed with a modest accuracy (10%) [55] [61] [9].

$$\frac{df}{dw} = \frac{N}{(w+1)^2} \qquad (6.42)$$

Where N is the electron occupation number. Substituting this approximation into the integrated cross-section equation (6.39) of the Binary encounter dipole model gives the following equation

$$\sigma_{BEB}(t_n) = \frac{S}{t_n + u + 1} \left[\frac{\ln t_n}{2} \left(1 - \frac{1}{t_n^2} \right) + 1 - \frac{1}{t_n} - \frac{\ln t_n}{t_n + 1} \right] \qquad (6.43)$$

The above equation represents the *BEB* model and is a function of the kinetic energy of the incident electron, where

$$t_n = \frac{T}{B} \qquad (6.44)$$

$$u = \frac{U_i}{B} \qquad (6.45)$$

$$S = 4\pi a_0^2 \left(\frac{R}{B_i}\right)^2 \qquad (6.46)$$

Here B is the binding energy, U_i is the kinetic energy, and N is the electron occupation number.

The total ionisation cross-section values calculated using BEB theory show a good agreement with the experiments over the entire range of T from the ionisation threshold to a few keV [64] [60], [62], [88], [7], [8], [58], and [68]

6.4 Development of the $QMS2 - EI$ ion source model

When an energetic electron beam passes through a gas containing atoms of cross-sectional area, due to the collisions with the gas loses its intensity and the ionic current i^+ thus generated in the EI ion source can be expressed as [80]

$$i^+ = \beta n_0 Q_i s_l i_e \qquad (6.47)$$

where i_e is the electron (emission) current (A), s_l is effective electron path length (m), Q_i is ionisation cross-section (Å), n_0 is density of molecules in the ionisation chamber (1/cubic meter) and β is ion-extraction efficiency.

6.4.1 Electron (emission) current (i_e)

In an EI ion source, electron emission currents are generally produced through thermionic processes on a heated metal filament surface. Electron emission from metals can be obtained by several methods. Electrons can be obtained from a hot metal cathode with a wide range of energies and from a cold cathode by the application of electric fields. Therefore the emission of an electron current from a metal surface depends on the tem-

perature of the metal and the applied field strength [85] [45] [30]. At high temperature, all substances leak electrical charge from the surfaces which then become conductors of electricity. Generally this type of conductivity happens when bodies are in a vacuum, as well as surrounded by a gaseous atmosphere and the effect is called thermionic electron emission. In the $QMS2 - EI$ ion Source model, the electron (emission) current is an input parameter.

6.4.2 Effective electron path length (s_l)

The determination of the effective electron path length in the ionisation chamber is necessary for the evaluation of the ionic current of a given gas component. If there is no axial magnetic field then the electron traverses through a straight line across the ionisation chamber and the length of the ionisation chamber can be taken as the effective electron path length. In the presence of an axial magnetic field electrons move in a helix and the electron path length depends on the size (radius) of the helix. This helical path is due to the component of electron velocity normal to the field direction.

For electron motion along a helix of diameter d_a mm, the corresponding maximum possible electron path length is given by [78]

$$L_{max} \quad = \quad s_l\left(1 + 1.10 \times \frac{10^{-4}d_a{}^2H^2}{E_n}\right) \tag{6.48}$$

where E_n is the energy of the electrons and H the magnetic field strength.

The magnetic field strength (H) is given by

$$H \quad = \quad \mu n I \tag{6.49}$$

where μ is the permeability, n the turn density in turns/m and, I the current flowing through the filament in A
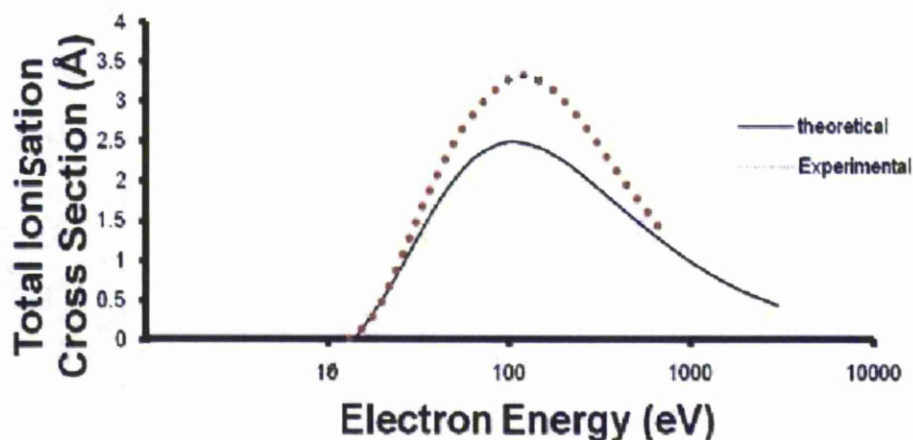
Figure 6.2: Total ionisation cross-section curve of oxygen gas

6.4.3 Ionisation cross-section (Q_i)

The total ionisation cross-section in the ionic current expression (Equation (6.47)) can be calculated using *BEB* theory as described earlier (Section 6.3) [65], [68]. The total ionisation cross-section can be obtained by integrating the differential cross-section over the electron energy. The *BEB* theory however uses the orbital binding energy B, the orbital kinetic energy $U = (p^2/2m)$, and the orbital electron occupation number N for the calculation of total ionisation cross-section for each orbital in the target atom or molecule.

The *BEB* cross-section as a function of the kinetic energy of the incident electrons, T can be calculated as a sum over all the molecular orbitals, as given in the equations (6.43) to (6.46), where B is the binding energy, U is the orbital kinetic energy, N is the electron occupation number, and Q is the dipole constant. B, U, N and Q are the four orbital constants needed for each orbital.

Figure 6.2 shows total ionisation cross-section curve of oxygen gas calculated using *BEB* theory. The theoretical results show good agreement with the published experimental values [92] in the electron energy range to 80 eV.

107

6.4.4 Density of molecules (n_0)

In the ionic current equation, the density of molecules in the ionisation chamber can be calculated by using ideal gas law using the specific gas constant (R_s), and is given by

$$P \; = \; DR_s T \qquad (6.50)$$

where D = density = mass / volume,

Therefore,

$$D \; = \; \frac{P}{R_s T} \qquad (6.51)$$

By dividing the mass (g) by the mass of one mole of the given gas component (g/mol), the mass of the given gas component in moles can be obtained. The number of molecules, i.e. molecular density in the ionisation chamber (n_0) for a given gas can be calculated by multiplying the calculated gas moles by Avogadro's number.

6.4.5 Ion extraction efficiency (β)

The ion extraction efficiency (β) in the ionic current equation (6.47) can vary from 2% to 100% for high sensitivity source. β depends on a number of factors such as energy homogeneity, beam width, and the mass of the ion [80].

6.5 Instrument description

A commercial *QMS* residual gas analyzer, MKS MicroVision Plus was used for the experiments. This is a single filter analyzer with rod electrodes of length 100 mm, diameter 6.35 mm, and r_0 is 2.76 mm. It is excited with a radio frequency of 1.8432 MHz, and the exit hole diameter in the *EI* ion source is 1.1 mm.

6.5.1 MKS MicroVision Plus *RGA* analyzer

The MKS MicroVision Plus *RGA* provides following features and benefits [2]:

High stability *RF* and data acquisition electronics, fast wide dynamic range scanning, a pre-filtered analyzer as standard for improved resistance to contamination and enhanced high-mass sensitivity.

The MKS Microvision Plus *RGA* software (Process Eye) is compatible with a windows environment and easy to use.

MKS Microvision Plus consists of an open *EI* ion source and quadrupole analyzer made of stainless steel and high-purity alumina ceramics. The source has independently replaceable twin filaments to provide built-in back-up for longer operation without vacuum interruptions [2].

6.6 Results and discussion

6.6.1 Experimental results

Reported here is the experimental analysis of argon gas using a commercial *QMS* residual gas analyzer described earlier (Section 6.5). During the experiment, argon gas was introduced into the vacuum chamber, which is maintained at a base pressure of 6×10^{-6} Torr. The electron emission current in the ion source was varied in the range from 0.35 mA to 1 mA and the electron energy was set to 70 eV.

Figure 6.3 shows typical argon experimental mass spectra for an electron current of 0.4 mA with a pressure of 7×10^{-5} Torr. Ion energy was set to 8.8 eV. Due to the *EI*, the parent atom breaks apart which is commonly known as the cracking/fragmentation pattern. This fragmentation pattern forms the mass spectrum, which aids identification of the gas atom. According to the cracking patterns for argon gas, there will be two peaks displayed on the mass-to-charge ratio scale, one at $m/z = 40$ and another peak at $m/z = 20$ with a theoretical percentage peak height ratio of (100:16) [3], [4]. This
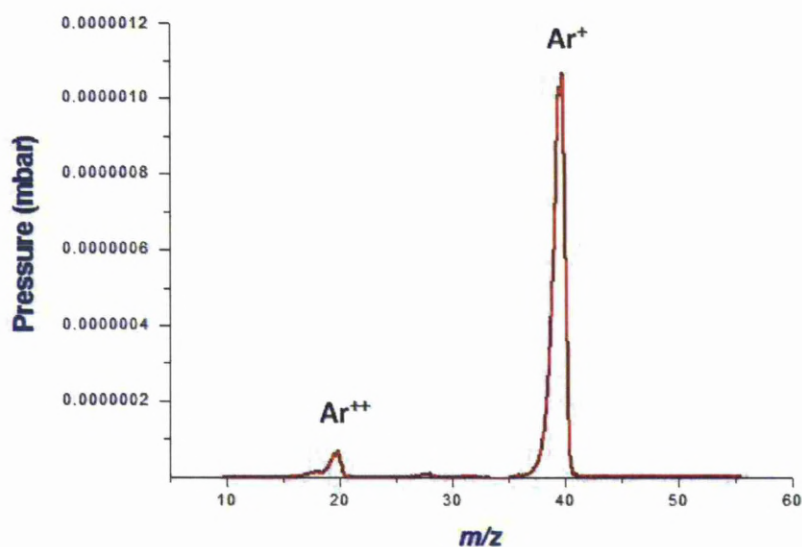
Figure 6.3: Typical mass spectra obtained using the commercial *QMS* residual gas analyzer for Argon gas

is because, during *EI* a majority of single ionized parent argon gas atoms (Ar$^+$) are created and there is a lower chance of doubly charged Ar atoms (Ar^{++}) being created. Thus, Ar$^+$ and Ar^{++} form the mass spectrum of argon gas. In the mass spectrum shown in Figure 6.3, the x-axis displays mass-to-charge ratio. Ar$^+$ is displayed at a mass-to-charge ratio of $40/+1 = 40$ and Ar^{++} is displayed at a mass-to-charge ratio of $40/+2 = 20$.

Figure 6.4 shows experimental mass peaks of argon gas of mass 40 for an emission current of 0.35 mA, electron energy of 70 eV, and ion energy of 8.8 eV showing the variation in peak height with the applied pressure in the vacuum chamber. The peak height in a mass spectrum is related to the partial pressure of the gas. The pressure of a designated component in a gas mixture forms the partial pressure. In Figure 6.4, the mass spectrum shows an increase in the peak height as the total pressure is maintained in the system between the pressure ranges 2×10^{-5} and 1×10^{-4} Torr. As expected the peak height in the mass spectrum increases with the partial pressure of ions. Figure 6.5 shows the graphical representation of the experimental mass peak heights of ^{40}Ar$^+$

110
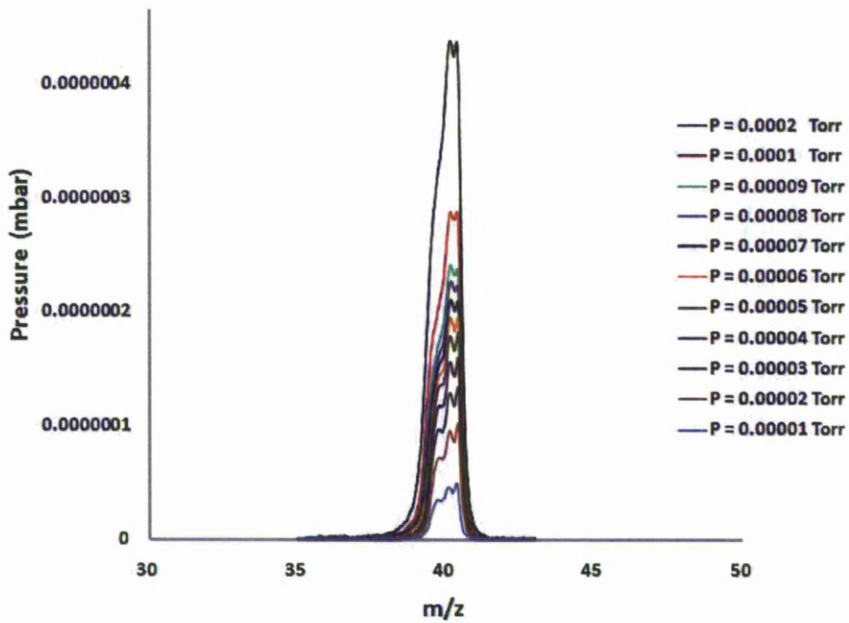
Figure 6.4: Experimental mass spectrum of ^{40}Ar$^+$
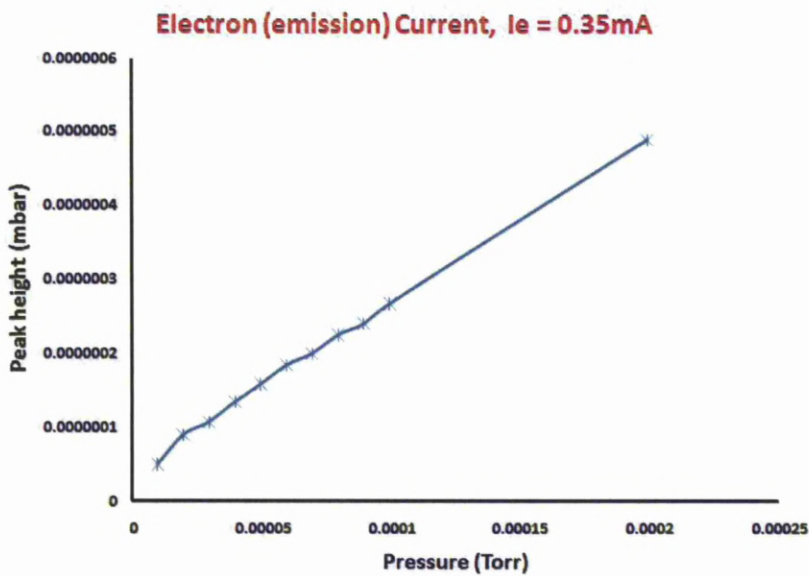
Figure 6.5: Graphical representation of the variation of peak heights with the total pressure in the range from 1×10^{-5} to 2×10^{-4} Torr for emission current of 0.35 mA
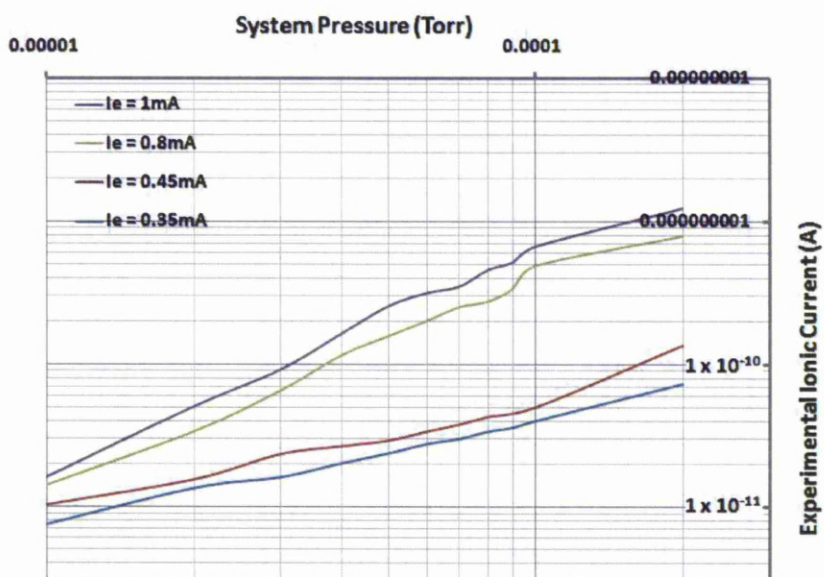
Figure 6.6: Experimental argon ionic current with increasing pressure for different electron emission currents

shown in figure 6.4 for the pressure ranges between 1×10^{-5} and 2×10^{-4} Torr.

Figure 6.6 shows the total pressure versus experimental total ionic current for $^{40}Ar^+$ with the total pressure in the range from 1×10^{-5} to 2×10^{-4} Torr for different emission currents of 0.35, 0.45, 0.8 and, 1.0 mA. As seen in Figure 6.6 the results show that increasing the total pressure in the chamber results in an increasing ionic current. The sample pressure correlates directly with the resulting ionic current [7]. Increase in the electron emission current at high pressure results in an increase in the ionisation of the neutral species to radical cations. As expected, the results show that increasing the emission current produces a higher ionic current. As seen in Figure 6.3 the system displays the mass spectrum by the displayed pressure (mbar) on the y-axis scale. The ionic current generated by the EI ion source in the MKS-RGA analyzer was calculated by multiplying the sensitivity of the system (taken from MKS MicroVision Plus RGA system manual) which is 1.5×10^{-4} A/mbar ($\equiv 2 \times 10^{-7}$ A/mTorr) by the displayed pressure (mbar) on the y-axis scale for the corresponding experimental argon peak.
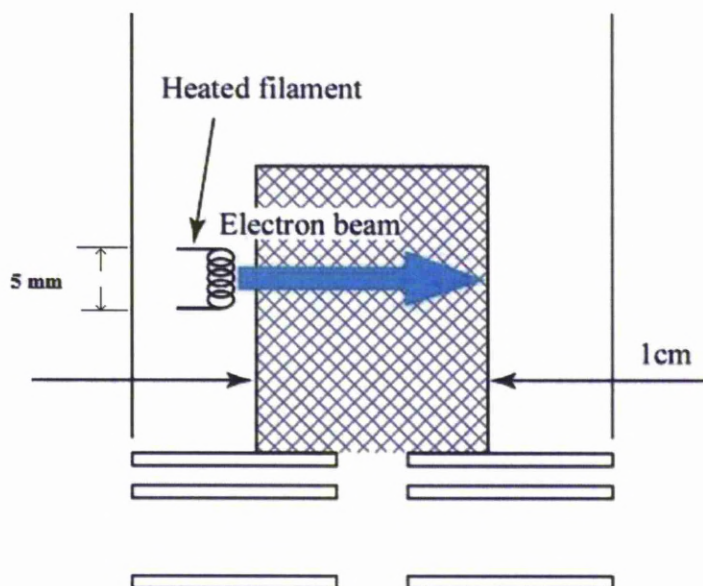
Figure 6.7: Typical *EI*-ion source of MKS MicroVision plus *RGA* analyzer

6.6.2 Theoretical results

Reported here is the theoretical analysis of argon gas using a basic equation for calculating ionic current[80] as described earlier (Section 6.4).

Figure 6.7 shows the typical *EI*-ion source of MKS MicroVision Plus *RGA* analyzer. The electron beam emitted from the heated filament is directed into the meshed ionisation cage where it is allowed to interact with the argon gas atoms. Upon interaction between the argon neutral atoms and e-beam, the neutral argon atoms ionize to radical cations as described earlier in the Chapter 3 (Section 3.2.1). The ionic current thus generated is calculated using the ionic current expression (Equation (6.47)) [80] as described in the Section 6.4.

For a filament length of 5mm, the turn density of 1000turns/m and the filament current of 1.6mA, the magnetic field strength produced by the heated filament is calculated to be 0.02 gauss. The maximum possible electron length that an electron can achieve due to the application of magnetic field strength is therefore calculated (equation (6.47)) [78] to be $(1 + 1.54 \times 10^{-8})$ cm which is a negligible increase in path

length compared to the collision chamber length. Because the axial magnetic field produced by the heated filament is quite small, the change in electron path length due to the magnetic field strength is deemed negligible. Because the magnetic field effect is neglected, the electron path length was taken as length of the collision chamber [13] . The total ionic current for argon gas was calculated by taking the effective electron path length (S) as length of the collision chamber which is 1 cm in the EI ion source of MKS MicroVision Plus RGA analyzer.

Figure 6.8 shows the theoretical total ionic current for $^{40}Ar^+$ as a function of the total pressure in the range from 1×10^{-5} to 2×10^{-4} Torr for different emission currents of 0.35, 0.45, 0.80, and 1.00 mA. The total ionic current was calculated by solving the ionic current expression and the value of the differential ionisation of a gas component was taken from the values generated using the BEB theory for different electron energies. In the calculation of ionic current of argon gas, the differential ionisation of a gas component value was taken from published values [10]. From the graph, it is very clear that the model predicts that the sample pressure correlates directly with the ionic current generated as found in the previous section (Figure 6.6).

The ionisation efficiency for an EI ion source is the ratio of ionic current formed to the electron emission current. In a vacuum system, an increase in partial pressure of the system results in an increase in the ratio of total number of ions formed to the molecules present. Figure 6.9 shows the calculated ionisation efficiency of argon gas for an emission current of 0.35 mA as a function of gas pressure.

6.6.3 Comparison of calculated and experimental total ionic current for argon gas

Figure 6.10 shows the comparison of the calculated and experimental total ionic current for argon gas of m/z 40 with the total pressure in the range from 1×10^{-5} to 2×10^{-4} Torr for emission currents of 0.35 mA and 0.45 mA. The ionic current was
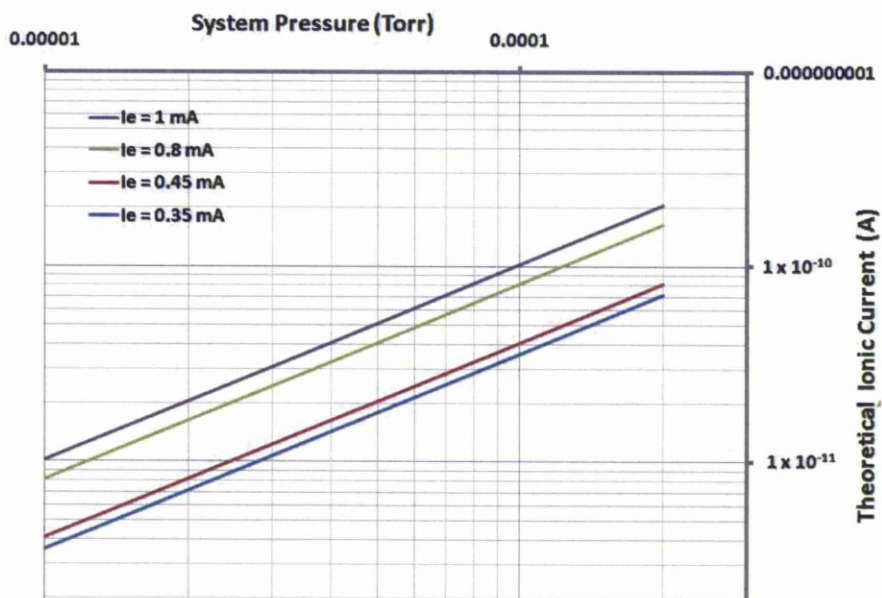
Figure 6.8: Predicted argon ionic current with pressure for different values of the electron emission current
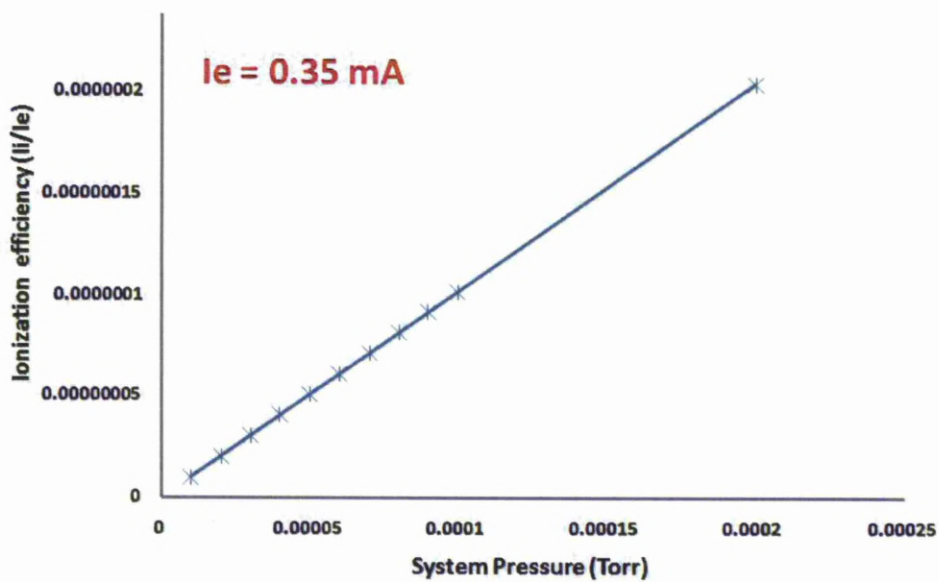
Figure 6.9: Calculated ionisation efficiency of argon gas as a function of gas pressure
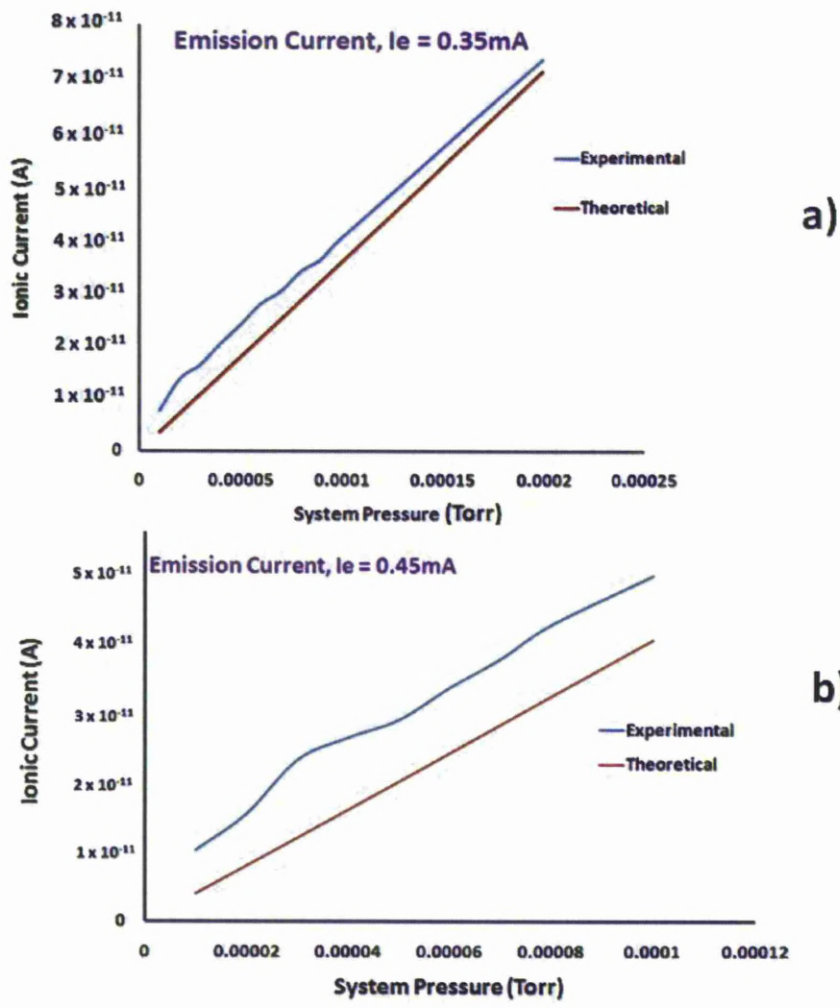
Figure 6.10: Comparison of calculated and experimental total ionic current for $^{40}Ar^+$ as a function of system pressure

calculated neglecting the axial magnetic field experienced by the heated coil as previously discussed.

The theoretical results show reasonable agreement with the experimental values. In an *EI* ion source, electron emission currents are generally produced through thermionic reactions on the heated metal filament surface. The hot filament applies thermal radiation to the environment which may lead to the development of thin layer of molecules onto the system surface. When the electrons emitted from the hot filament come in contact with the system surface leads to the release of gas which effects other instru-

116

ment used for system pressure calibration. Therefore the pressure gauge used may not determine the exact partial pressures of the vacuum system. Taking this into account and the effect of certain parameters like outgassing rate, a good agreement between the theoretical and experimental values can be seen.

6.7 *GUI* of pressure dependence $QMS2 - EI$ ion source model

Using the theoretical approach described an *EI* ion source model has been developed which allows simulated mass spectra to be determined. Input parameters include electron emission current, electron energy, and pressure. Figure 6.11 shows the graphical user interface of pressure dependence $QMS2 - EI$ ion source model.

The model has been developed in the Visual C++ environment to allow better prediction of instrument performance. Previous versions of the $QMS2$-Ion source model do not support the calculation of ionic current, which has a pressure dependence. The new model calculates the ionic current of the given gas component and takes the value of ionisation cross-section of a gas component from the values generated using the *BEB* theory for different electron energies. From the ionic current calculated, the model generates the total number of ions required to simulate at each mass scan point.

Figure 6.12 shows simulated mass peaks of argon gas of m/z 40 calculated using the $QMS2$-Hyperbolic and $QMS2 - EI$ ion Source pressure dependence programs operated at Stability Zone 1 ($a = 0.237$ and $q = 0.706$). The computer simulation test conditions are given in Table 6.1. The figure shows an increase in the peak height, and consequently by an increase in the peak width as the total pressure is maintained in the system over the pressure range 1×10^{-5} to 2×10^{-4} Torr.

Figure 6.13 shows the comparison of simulated and experimental mass peaks for $^{40}Ar^{+}$. The simulated ionic current is input into the QMF simulator and the mass

117
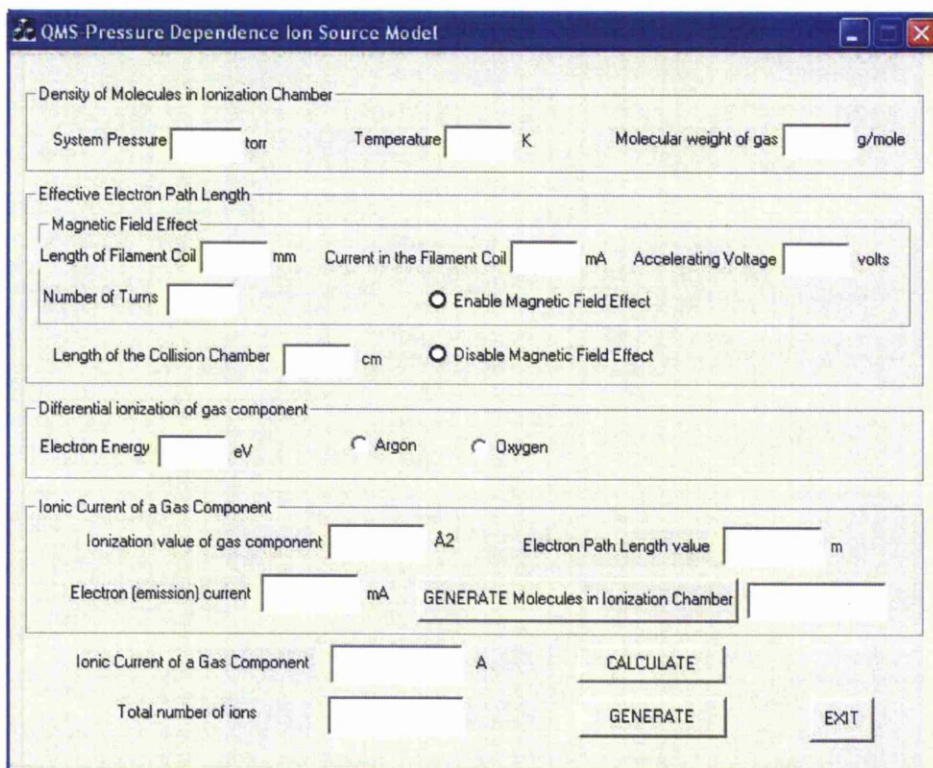
Figure 6.11: Graphical user interface of pressure dependence $QMS2 - EI$ ion source model

Table 6.1: $QMS2$ computer simulation test conditions

QMF PARAMETER	CONDITION
Length	100 mm
r_0	2.76 mm
Frequency	1.8432 MHz
U/V	100
Detector radius	10 mm
Ion Source	
Ion energy	8.8 eV
Ion source radius	0.55 mm
Ion energy spread	0
Ion angular spread	0
Ion species	40 m/z
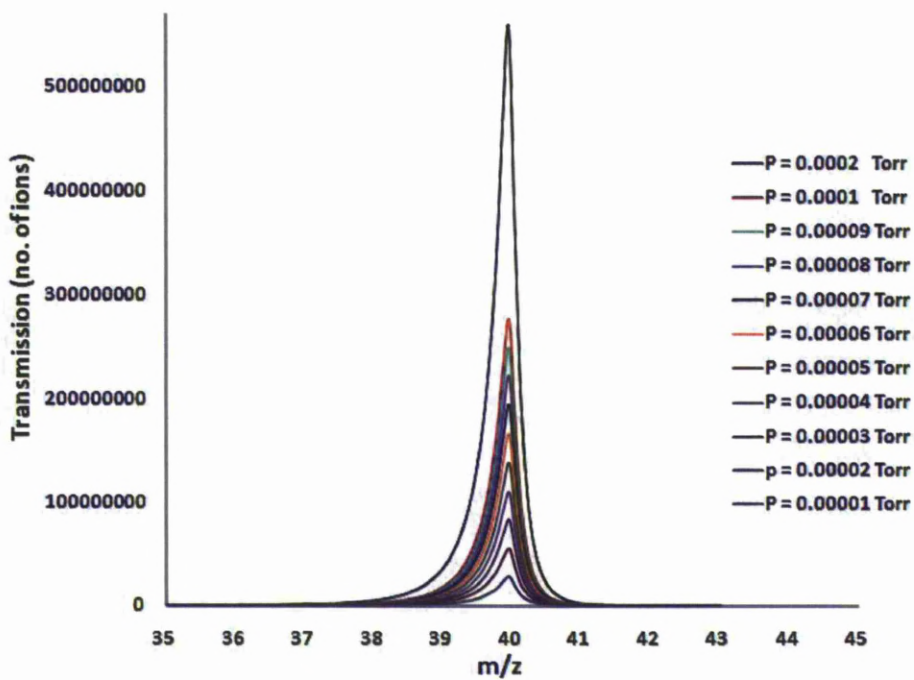
Figure 6.12: Simulated mass spectrum of $^{40}\text{Ar}^+$
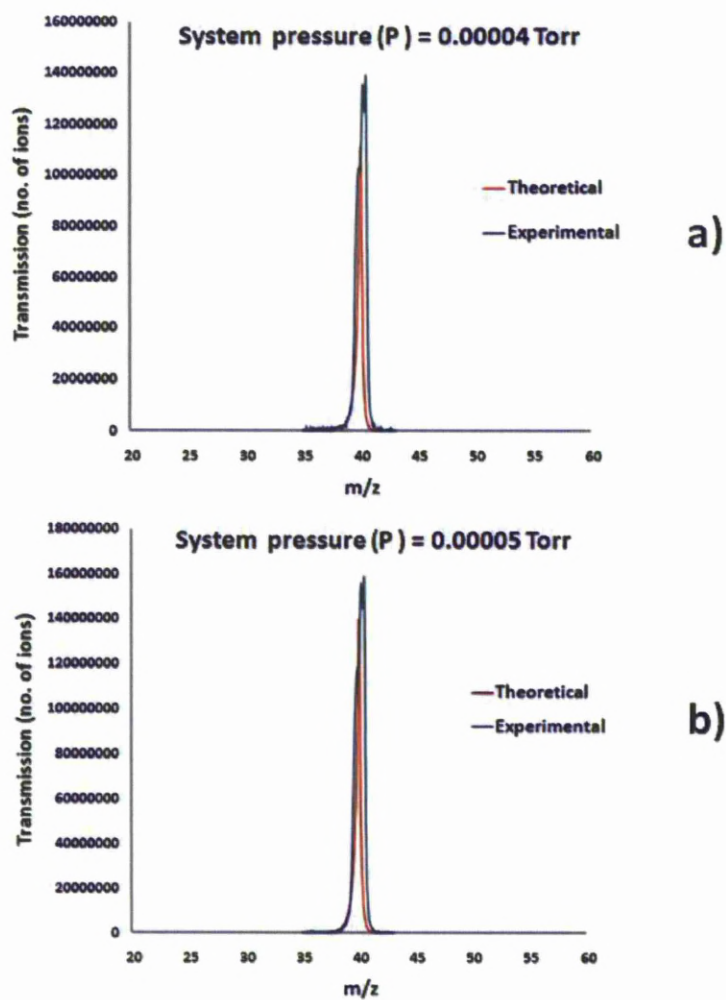
Figure 6.13: Comparison of simulated and experimental mass spectrum of $^{40}Ar^+$

spectral peak (partial pressure) for a particular gas determined and compared with experiment. The input parameters for the ion source and the QMF are the same as in the experiment as described above. The simulated mass peaks of $^{40}Ar^+$ show reasonable match with the experimental mass peaks. Taking into consideration the effect of certain parameters like outgassing rate, a good match between the simulated and experimental mass peaks can be seen.

6.8 Conclusions

The developed $QMS2 - EI$ ion source pressure-dependence model allows simulated mass spectra to be determined which include the effects of electron emission current, electron energy and pressure. Thus, in this work the previous version of QMS2-ion source model has been upgraded to include these effects.

Chapter 7

MEDICAL APPLICATION OF PORTABLE QMS

7.1 *Helicobacterpylori*

Helicobacterpylori (*H.pylori*) is a unicellular microorganism with no nucleus and also no membrane bound organelles. It has a single strand of circular chromosome which holds its genetic information. As seen in the Figure 7.1, *H.pylori* has flagella that aids its movement. It is a unicellular organism and can change its shape. Its outer membrane consists of lipopolysaccharides and hence it stays pink, indicating that it is a gram-negative bacterium. It is a parasite and always inhabits and affects the intestinal tract of the host. The Health Organization's International Agency for Research on Cancer (*IARC*) classified the bacterium as a grade 1 carcinogen on a par with hepatitis B virus [107] [76].

7.2 Ulcer formation in the human stomach

The body of the stomach has the glandular epithelium cells which are the acid-secreting tissues. The epithelial cells are comprised of G and D cells which manufacture hy-
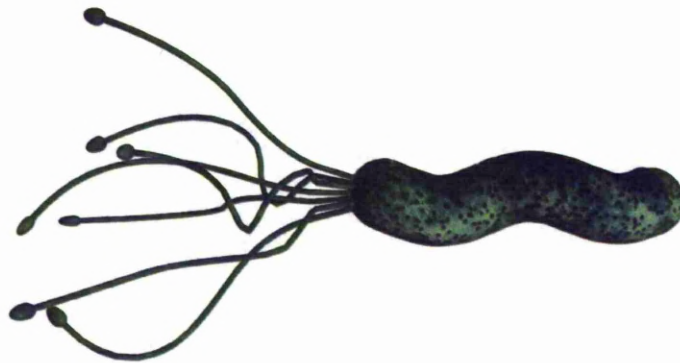
Figure 7.1: *Helicobacter pylori*
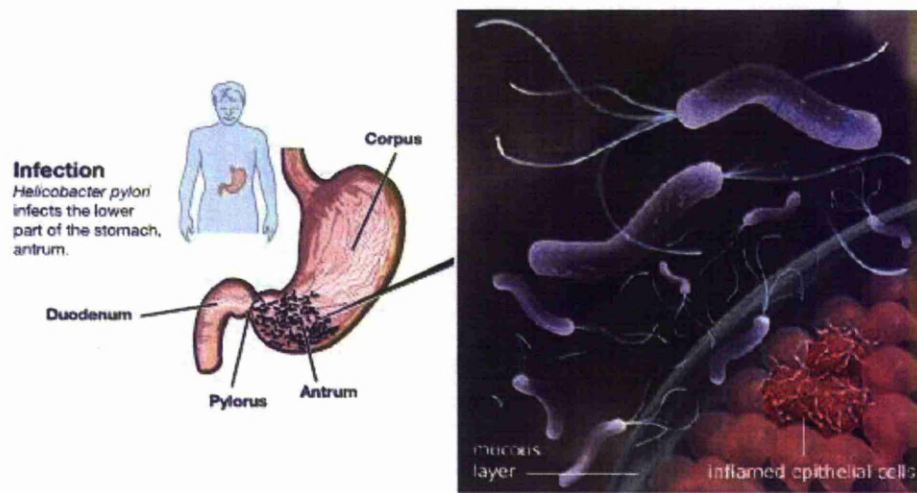
Figure 7.2: *H.pylori* invading epithelial cells [1]

drochloric acid and pump it into the lumen. The pyloric antrum of the stomach is the area of the gastric mucus lining to the pylorus. The circular opening of the stomach leads to the duodenum [66].

7.2.1 *Helicobacter pylori* attachment

H.pylori are attached to the protective mucus lining of the stomach wall and because they are inside the mucus lining, the bacteria can be protected by the body immune system. The bacteria secrete the enzyme urease, which neutralizes the acid secreted by the stomach cells by converting urea into the basic ammonia and buffer bicarbonate
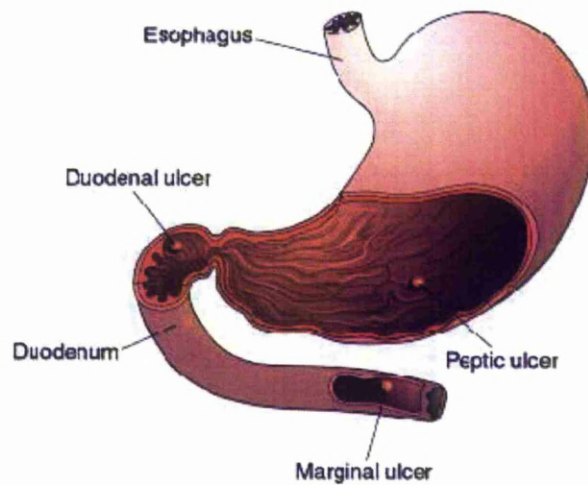
Figure 7.3: Ulcer-infected stomach [77]

and thus enabling them to survive in the acid environment of the stomach. The bacteria produce vaculating cytotaxin A that damage the lining cells of the stomach, and this allows the bacteria to absorbs the nutrients that have been sent to stomach lining cells. Figure 7.2 shows *H.pylori* invading epithelial cells.

7.2.2   Cell infection

Bacterial damage to the cellular lining of the stomach creates holes in the mucus layer, causing the formation of ulcers; if left untreated then may lead to cancer. *H.pylori* is generally accepted as the cause of most gastroduodenal diseases including peptic ulcers and gastric cancer [77]. Figure 7.3 shows an ulcer-infected stomach.

Figure 7.4 shows photographs of peptic ulcers taken by endoscopy [77]. The first photograph shows the most common type of peptic ulcer which is located in the duodenum, a few centimeters past the pyloric sphincter which controls the outlet from the stomach, and the second photograph shows the gastric or stomach ulcer [77].
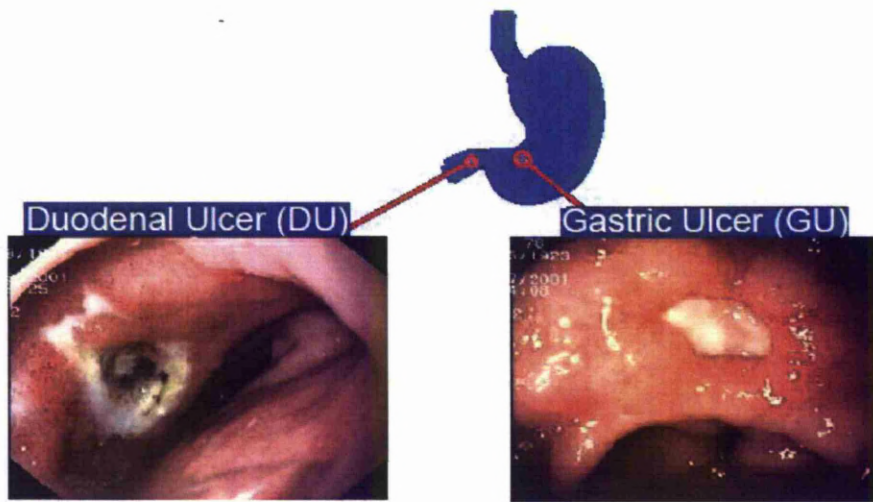
Figure 7.4: Typical appearance of peptic ulcer [77]

7.3 Diagnostic procedure for *Helicobacter pylori* detection

H.pylori may be classified by using both invasive and non-invasive tests.

7.3.1 Invasive tests

Invasive tests are also called indirect tests, based on antibodies, which are very accurate for initial diagnosis but are difficult to interpret in a previously treated patient.

7.3.2 Non-invasive tests

Non-invasive tests are also called direct tests, which include biopsy for gram stain, culture, rapid urease test and histology, urea breath test, stool antigen test and various molecular methods on gastric material. A recent study shows that the urea breath test is more accurate than serology in diagnosing *H.pylori*. Molecular methods such as polymerase chain reaction (*PCR*) yield quicker results but have been difficult to introduce in the laboratory.

7.4 Urea breath test

The carbon-13 and carbon-14 urea breath tests are a well established non-invasive type of test used to diagnose *H.pylori* infection [91], [70]. These tests have excellent sensitivity and specificity. The great advantage of urea breath test (UBT) is that they are non-invasive and rapid. Both the carbon-13 and carbon-14 urea breath tests have the same fundamental principle, the single difference is being the use of different isotopes of carbon. *H.pylori* produces a significant quantity of urease in the gastric mucosa of an infected individual. The injected ^{14}C or ^{13}C labeled urea is enzymatically hydrolysed by the urease secreted by the *H.pylori* on contact with the gastric mucosa. The resultant products are ammonia and carbon dioxide, which diffuse into the blood and are excreted by the lungs. Isotopically labeled carbon dioxide can therefore be detected in breath [32]. Figure 7.5 shows the principle of the carbon-14 urea breath test. The carbon-14 urea breath test is carried out by scintillation scotoma to detect radiolabelled carbon dioxide.
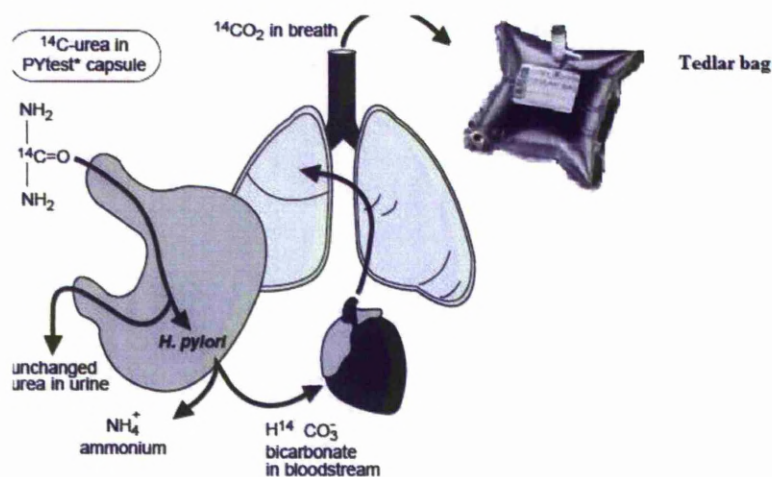
Figure 7.5: The principle of the carbon-14 urea breath test

7.5 Tedlar Bag

To test the gas samples taken from hospital patients, breath samples need to be captured and transported in a gas detection system. Costs, re-usability, durability, size and versatility are the important issues when choosing a sample holder. Tedlar is tough, durable, and considered chemically inert to a wide range of compounds. Tedlar bags can be used for indoor air sampling, calibration test standards, leaking underground storage tanks, hazardous waste sites, stack sampling, soil gas sampling, gas blending, and most other gas sampling needs. Tedlar bags are well suitable for the breath sample analysis in medical studies. Figure 7.6 shows a Tedlar gas sampling bag of size 25 x 22.5 cm, used in this study.

Figure 7.6: Tedlar gas sampling bag

7.6 Experimental analysis

A portable quadrupole mass spectrometer (QMS) system with a triple filter, closed ion source and heated capillary inlet (MKS Cirrus [5]) was used to identify patients with $H.pylori$ using the non-invasive carbon-13 Urea breath test. The following tests were

conducted upon a number of patients at the Royal Liverpool University Hospital over a period of 8 months from August 2007.

7.6.1 Measures followed at Royal Liverpool University Hospital for samples collection

The Royal Liverpool University Hospital uses a simple procedure to take samples from patient for testing. Patient drinks a solution of urea or carbamide, an organic compound with the chemical formula $(NH_2)_2CO$. The molecule has two amine groups joined by a carbonyl functional group. Orally administered urea is hydrolysed to ammonia and carbon dioxide which is diffused into the blood and is excreted by the lungs. This isotopically labelled carbon dioxide can be detected in the breath. Pre-drink and post-drink samples of breath are taken per patient. The timing gap between pre-drink and post-drink samples should be thirty minutes. The air is exhaled into a tedlar gas sampling bag as shown in the Figure 7.6.

7.6.2 Testing samples in the departmental QMS laboratory

The quadrupole analyzer is used to measure the carbon-13 in the air sample. The pre-drink breath bag sample is connected to the open valve of QMS and kept for ten seconds because the flow should be uniform. QMS sampling program installed is started where it takes six consecutive scans. The same procedure is repeated for the post-drink breath bag sample and the graphs obtained are recorded. Figure 7.7 shows the QMS output from a patient's breath using a linear scale. Figure 7.8 gives the same output with a log scale which shows spectral peaks at m/z 44 and 45 corresponding to $^{12}CO_2^+$ and $^{13}CO_2^+$

The comparison of pre-drink and post-drink urea measurements is used to determine infection. According to the results, if [Post-ratio/Pre-Ratio] is greater than 0.03 then a positive diagnosis is assumed ($H - Pylori$ present) or if [Post-ratio/Pre-Ratio] is
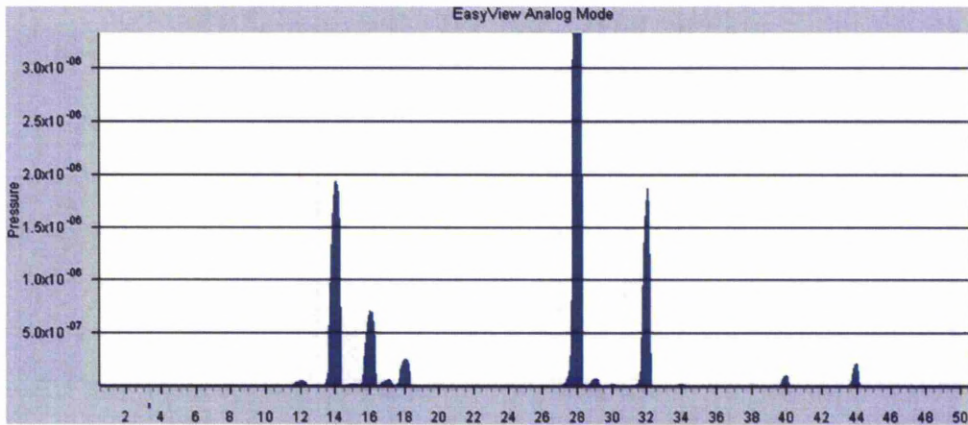
Figure 7.7: *QMS* output from patient breath using a linear scale
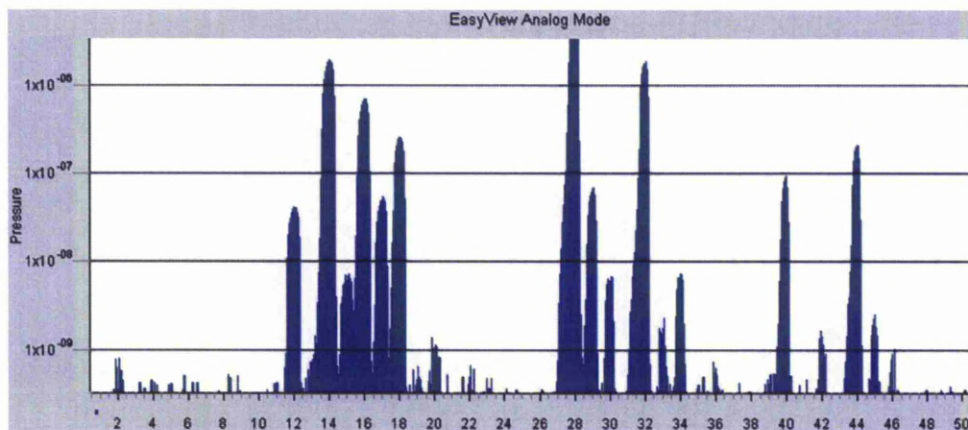
Figure 7.8: *QMS* output from patient breath with a log scale shows spectral peaks at m/z 44 and 45 corresponding to $^{12}CO_2^+$ and $^{13}CO_2^+$

less than 0.03 then a negative diagnosis is assumed ($H - Pylori$ absent).

7.7   Results and discussion

7.7.1   Experimental (positive results)

Figures 7.9 and 7.10 show the Patient 4: pre-drink breath sample before taking the urea

tablet and Patient 4: post-drink breath sample, 30 minutes after taking the urea tablet.

Figure 7.11 shows the pre-drink and post-drink breath samples superimposed.
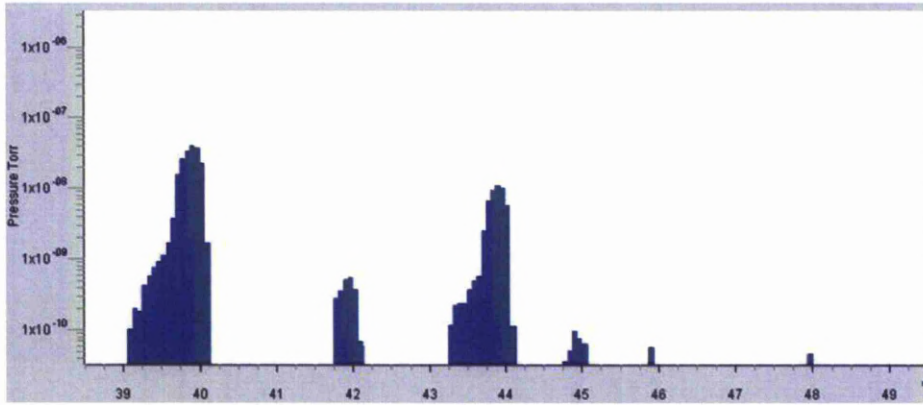
Figure 7.9: Patient 4: pre-drink breath sample before taking urea tablet
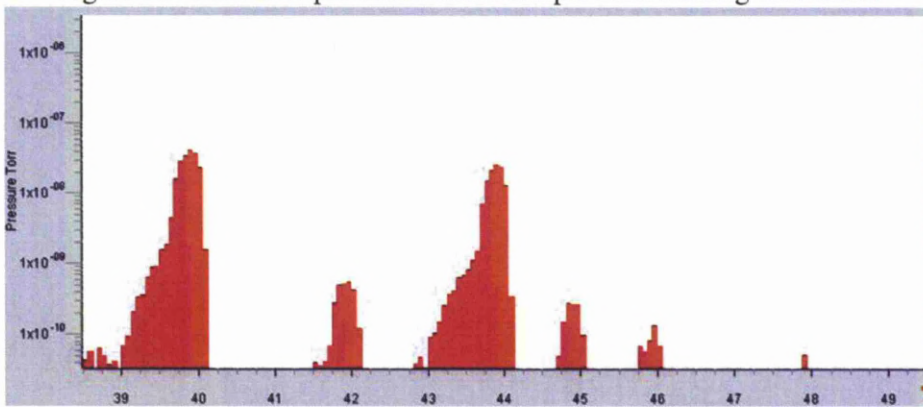
Figure 7.10: Patient 4: post-drink breath sample, 30 minutes after taking urea tablet
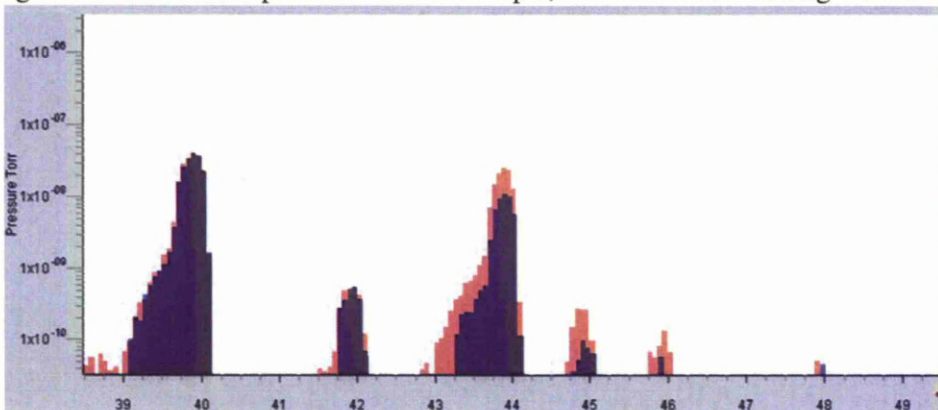
Figure 7.11: The pre-drink and post-drink breath samples superimposed

In Figure 7.11, a comparative study between the pre-drink breath sample and the post-drink breath sample and also a mass 44 and mass 45 concentration study has been made. In this case, it is very clear that the ratio of the peak heights for the m/z = 44 and m/z = 45 after taking the urea tablet shows an increase of 3.3%, so it leads positive diagnosis, the presence of *H.pylori* in the stomach.

7.7.2 Experimental (negative results)

Figures 7.12 and 7.13 show the Patient 5: pre-drink breath sample before taking the urea tablet and Patient 5: post-drink breath sample, 30 minutes after taking the urea tablet. Figure 7.14 shows the pre-drink and post-drink breath samples superimposed.

In Figure 7.14, a comparative study between the pre-drink and the post-drink breath samples and also a mass 44 and mass 45 concentration study has been made. In this case, it is very clear that the ratio of the peak heights for the m/z = 44 and m/z = 45 after taking the urea tablet remains unchanged, so it leads negative diagnosis i.e. the absence of *H.pylori* in the stomach.

7.7.3 Summary of results for 45 patients

Table 7.1 gives the summary of results for 45 patients bag samples tested as they arrive from Royal Liverpool Hospital in the period from 1st August - 18th March. The results show agreement with the hospital results in 38 out of 45 cases with 3 false positives (Patients 7,9,25) and 3 false negatives (Patients 17,21,42)

Figure 7.15 shows the receiver operating characteristic (ROC) plot for the summary of results for 45 patients samples tested. ROC is a graphical plot used to evaluate the diagnostic performance/accuracy of a test to discriminate diseased cases from normal cases. In a ROC curve the true positive rate (sensitivity) is plotted in function of the false positive rate (specificity) for different cut-off points of a parameter. ROC curve shows that any increase in sensitivity will be accompanied by a decrease in specificity.
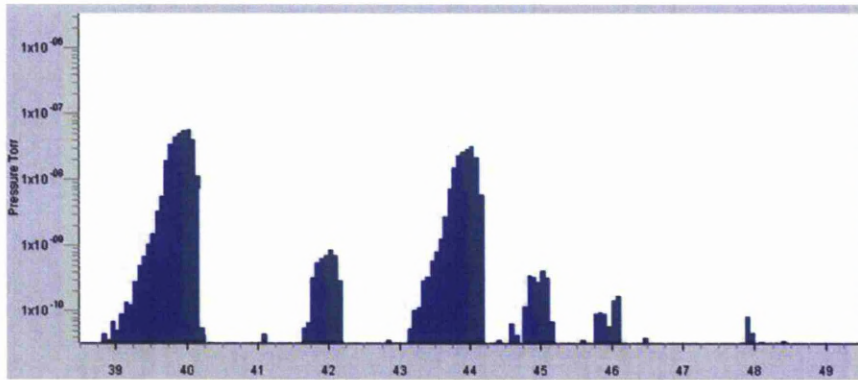
Figure 7.12: Patient 5: pre-drink breath sample before taking urea tablet
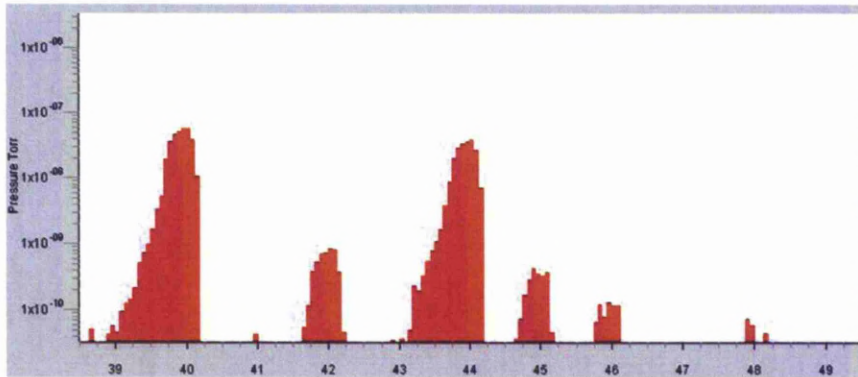
Figure 7.13: Patient 5: post-drink breath sample, 30 minutes after taking urea tablet
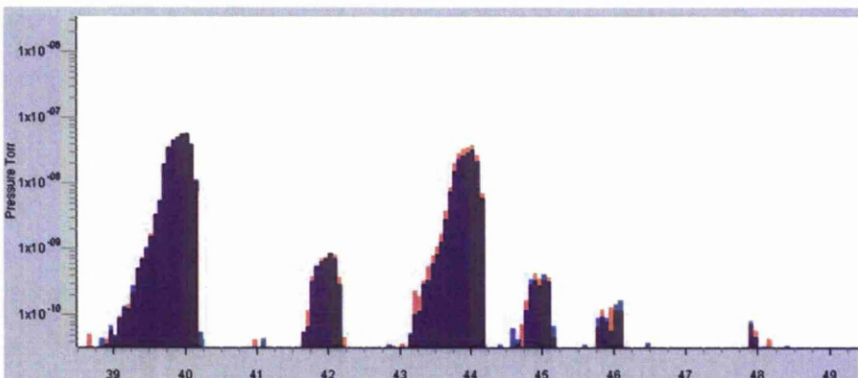
Figure 7.14: The pre-drink and post-drink breath samples superimposed

Table 7.1: Summary of results for 45 patients

Patient	Date tested – First run	Percentage change (Post-ratio/Pre-ratio)	Our result	Hospital result
1	1st August	2.3805	Negative	Negative
2	1st August	2.6119	Negative	Negative
3	4th August	-0.27153	Negative	Negative
4	4th August	3.3088	Positive	Positive
5	4th August	1.5157	Negative	Negative
6	14th August	-0.41268	Negative	Negative
7	14th August	3.2864	Positive	Negative
8	14th August	-0.6307	Negative	Negative
9	14th August	5.0282	Positive	Negative
10	14th August	-1.4281	Negative	Negative
11	23rd August	-1.3585	Negative	Negative
12	23rd August	-1.392	Negative	Negative
13	23rd August	1.7658	Negative	Negative
14	23rd August	-7.4317	Negative	Negative
15	22nd November	-5.7499	Negative	Negative
16	22nd November	-5.5067	Negative	Negative
17	22nd November	-1.7904	Negative	Positive
18	22nd November	-1.3738	Negative	Negative
19	22nd November	2.7059	Negative	Negative
20	28th November	0.90435	Negative	Negative
21	28th November	0.057905	Negative	Positive
22	28th November	-6.1336	Negative	Negative
23	28th November	1.2009	Negative	Negative
24	30th November	-0.33432	Negative	Negative
25	30th November	3.2398	Positive	Negative
26	30th November	1.4659	Negative	Negative
27	30th November	2.0393	Negative	Negative
28	30th November	-3.0747	Negative	Negative
29	30th November	-3.1673	Negative	Negative
30	8th December	0.42858	Negative	Negative
31	8th December	-0.22003	Negative	Negative
32	8th December	-0.13014	Negative	Negative
33	8th December	-1.3796	Negative	Negative
34	18th February	5.2481	Positive	Positive
35	18th February	2.4104	Negative	Negative
36	18th February	-3.2602	Negative	Negative
37	7th March	-1.4923	Negative	Negative
38	7th March	-4.7456	Negative	Negative
39	7th March	-6.1669	Negative	Negative
40	18th March	-1.4061	Negative	Negative
41	18th March	-3.7616	Negative	Negative
42	18th March	0.4252	Negative	Positive
43	18th March	-0.046	Negative	Negative
44	18th March	-5.0121	Negative	Negative
45	18th March	0	Bag empty	Positive

133

In Figure 7.15, the curves were constructed by computing the sensitivity and specificity of clinical findings in predicting *H.pylori*. The accuracy of a diagnostic test is classified based on the traditional academic point system [6]:

- .90 - 1.0 = excellent (A)

- .80 - .90 = good (B)

- .70 - .80 = fair (C)

- .60 - .70 = poor (D)

- .50 - .60 = fail (F)
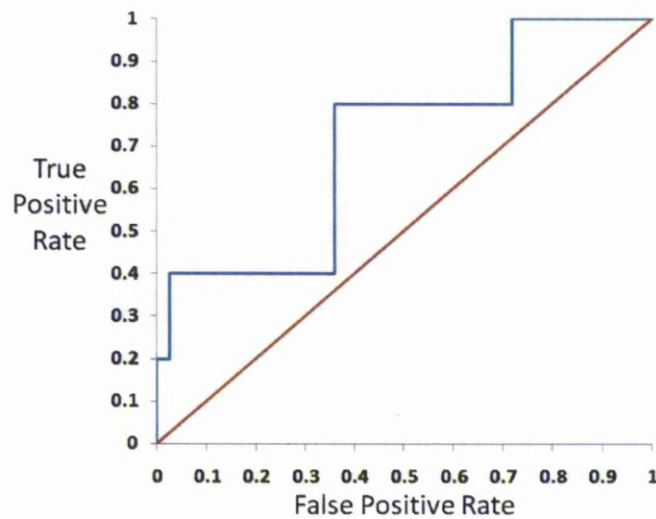
Figure 7.15: Receiver operating characteristic curve

From ROC plot, the area under the curve is .71 and therefore the accuracy of carbon-13 urea breath test used to diagnosis *H.pylori* infection would be considered to be "fair".

7.8 Conclusions

From the summary of results obtained it reveals that there is a good agreement between the hospital results and laboratory results. This treatment can be simply and non-invasively performed . This method reduces the time spent in the visits to the clinic, and a fairly accurate result can be obtained in a short time (under 30 minutes). The results show the feasibility of using a portable *QMS*-based system for in-situ *helicobacterpylori* detection.

Chapter 8

CONCLUSIONS AND FUTURE WORK

In monitoring a complex vacuum system, such as is used in particle accelerators and in many other applications, e.g. equipment for medical diagnosis, environmental monitoring, explosives, and oil and gas monitoring there are particular challenges; many of these can be readily met by an appropriately chosen Quadrupole Mass Spectrometer (*QMS*). Even though the quadrupole mass filter needs a very high constructional precision to achieve the highest performance level, *QMS* instruments are extremely useful due to their ease of use, size and relatively low cost. The commercially available *QMS* instruments generally provide limited characteristics and usually operate in stability Zone 1. Software modelling and simulation work plays a very important role in a study of well-defined application requirements. A software model can also help in identifying the application solution, for a process problem at a reduced cost and cycle time.

In this work, simulation studies have been carried out using the QMS2-Hyperbolic computer simulation program to show the possibilities of achieving a better resolution for the qualitative and quantitative identification of low mass iostopes in a process environment which require a resolution greater than 930. The simulation results dis-

cussed in this thesis show that the use of hyperbolic electrodes operated in stability Zone 3 is the best option to provide the resolution necessary for separation of HT in the presence of D_2 species. The closeness of the species discussed demands high resolution to take care of mass discrimination and to achieve adequate abundance sensitivity. This places tight constraints on the tolerance budget for the control electronics of the electrode drive system. The high mass tail has a greater effect than the lower mass tail on abundance sensitivity for these two species. Tighter control of the QMF to ion source alignment accuracy is required in the y-axis compared to the x-axis due to the narrower y-axis Zone 3 stability area. The results show that there is scope to optimize the choice of QMF length and drive frequency. Future work may be aimed at the design and manufacture of a prototype instrument to investigate and quantify the performance characteristics experimentally and to undertake field trials on the target process line.

A QMS2-EI ion source pressure-dependence theoretical model has been developed using the Visual C++ environment. The model calculates the electron-impact total ionization cross-sections as a function of electron energy using the Binary-Encounter-Bethe (BEB) theory . The BEB prediction for oxygen gas shows good agreement with the published experimental values in the range to 80eV. The calculated theoretical ionic currents are compared with the ionic current of the experimental results obtained form a commercial QMS residual gas analyzer and show agreement. Successful simulation tests have also been carried for argon gas in the pressure range from 10^{-6} to 10^{-4} Torr for different emission currents 0.35, 0.45, 0.80, and 1mA. The results of this newly developed model, which takes into account of the pressure dependence, have been compared with the experimental results for argon gas measured using a commercial gas analyzer.

The predicted results of argon match well with the experiments. The developed QMS2-EI Ion Source pressure-dependence model allows simulated mass spectra to be determined which include as adjustable parameters electron emission current, electron

energy, and pressure. Thus, in this work the previous version of QMS2-Ion source model has been upgraded to include these effects. Future work should be focussed upon testing the model with different gases and quantify the performance characteristics experimentally and to use the model in residual gas applications.

A successful non-invasive carbon-13 urea breath test was developed and conducted upon a number of patients at the Royal Liverpool University Hospital over a period of 8 months from August 2007 using a portable QMS system with a triple filter, closed ion source and heated capillary inlet to identify the presence of $H.Pylori$ infection. The results obtained using the QMS agreed very well with the hospital results ($86.37 \pm 2.1\%$), indicating that this approach using a portable QMS could be a viable alternative to the conventional method of using a centralised testing facility. This test can be simply performed and gives rapid diagnosis (under 30 minutes). From the summary of results obtained from the patient trials there is some controversy between the hospital results and the obtained results, but it is not unusual for new testing methods to produce slightly different results in a minority of cases. A commercially available portable QMS was used for the patient trials. It is well known that most of the commercial QMS systems utilize a Quadrupole Mass Filter (QMF) based on circular rods and operate in stability Zone 1. However, with further improvements (e.g. use of hyperbolic electrodes) QMS instrument could become highly suitable for widespread deployment in detecting H-pylori and in other medical applications.

References

[1]   URL www.nobleprize.org

[2]   URL http://www.mksinst.com/docs/UR/microv.pdf

[3]   URL http://webbook.nist.gov/chemistry/

[4]   URL http://www.hidenanalytical.com/reference/cracking.html

[5]   URL http://www.mksinst.com/docs/UR/CirrusDS.pdf

[6]   URL www.originlab.com

[7]   Ali, M.A., Irikura, K.K., Kim, Y.K.: Electron-impact total ionization cross sections of sf(x)(x = 1-5). International Journal of Mass Spectrometry 201(1-3), 187–195 (2000).

[8]   Ali, M.A., Kim, Y.K.: Total ionization cross sections of Cl and Cl2 by electron impact. Surface and Interface Analysis 37(11), 969–972 (2005).

[9]   Ali, M.A., Kim, Y.K., Hwang, W., Weinberger, N.M., Rudd, M.E.: Electronimpact total ionization cross sections of silicon and germanium hydrides. Journal of Chemical Physics 106(23), 9602–9608 (1997).

[10]   Ali, M.A., Stone, P.M.: Electron impact ionization of metastable rare gases: He, Ne and Ar. International Journal of Mass Spectrometry 271(1-3), 51–57 (2008).

[11]   Ashcroft, A.E.: Ionization Methods in Organic Mass Spectrometry. Cambridge: Royal Society of Chemistry (1997).

[12]   Aston, F.W.: Isotopes. Arnold, London (1922).

[13]   Asundi, R.K.: Electron path length in collision experiments. Proceedings of the Physical Society 82, 372–374 (1963).

[14]   Badman, E.R., Cooks, R.G.: Miniature mass analyzers. Journal of Mass Spectrometry 35(6), 659–671 (2000).

[15]   Baril, M., Le, R., Marchand, P.: An improved and accurate method for the calculation of trajectories in quadrupole mass filters and ion traps using phase space dynamics. International Journal of Mass Spectrometry and Ion Processes 98(1), 87–97 (1990).

139

[16] Batey, J.: Quadrupole gas analysers. Vacuum 37(8-9), 659–668 (1987).

[17] Bohm, D.: Quantum theory. Courier Dover Publications (1989).

[18] Bracco, G.: Comparison of quadrupole mass filters equipped with rods of different convexity: An analysis by finite element methods and trajectory simulations. International Journal of Mass Spectrometry 278(1), 75–88 (2008).

[19] Bruins, A.P.: Mass spectrometry with ion sources operating at atmospheric pressure. Mass Spectrometry Reviews 10(1), 53–77 (1991).

[20] Dawson, P.H.: The Mass Filter: Design and Performance. In Quadrupole Mass Spectrometry and Its Applications, Austin, W. E., Holmes, A. E., Leck, J. H., Eds.; Elsevier, Amsterdam, 121 - 152 (1976).

[21] Dawson, P.H., Hedman, J.W., Whetten, N.R.: A simple mass spectrometer. Review of Scientific Instruments 40(11), 1444–1450 (1969).

[22] Dawson, P.H., Whetten, N.R.: Non-linear resonances in quadrupole mass spectrometers due to imperfect fields I. The quadrupole ion trap. International Journal of Mass Spectrometry and Ion Physics 2(1), 45–59 (1969).

[23] Dawson, P.H., Whetten, N.R.: Non-linear resonances in quadrupole mass spectrometers due to imperfect fields. II. The quadrupole mass filter and the monopole mass spectrometer. International Journal of Mass Spectrometry and Ion Physics 3(1-2), 1–12 (1969).

[24] Day, C.: The use of a high-resolution quadrupole gas mass spectrometer system for selective detection of helium and deuterium. Vacuum 51(1), 21–30 (1998).

[25] Dayton, I.E., Shoemaker, F.C., Mozley, R.F.: The measurement of twodimensional fields. part ii: Study of a quadrupole magnet. Review of Scientific Instruments 25(5), 485–489 (1954).

[26] Dempster, A.J.: A new method of positive ray analysis. Physical Review 11(4), 316–325 (1918).

[27] Desiderio, D.M., Nibbering, N.M.: Mass Spectrometry: Instrumentation, Interpretation, and Applications. Wiley (2008).

[28] Deutsch, H., Becker, K., Matt, S., Märk, T.D.: Theoretical determination of absolute electron-impact ionization cross sections of molecules. International Journal of Mass Spectrometry 197(1-3), 37–69 (2000).

[29] Doherty, A.J., Ashford, S.R., Subramanya, H.S., Wigley, D.B.: Bacteriophage t7 dna ligase: Overexpression, purification, crystallization, and characterization. Journal of Biological Chemistry 271(19), 11,083–11,089 (1996).

[30] Dolan, W.W., Dyke, W.P.: Temperature and field-emission of electrons from metals. Physical Review 95(2), 327–332 (1954) 140.

[31]   Dooley, C.P., Cohen, H., Fitzgibbons, P.L., Bauer, M., Appleman, M.D., Perez-Perez, G.I., Blaser, M.J.: Prevalence of helicobacter pylori infection and histologic gastritis in asymptomatic persons. New England Journal of Medicine 321(23), 1562–1566 (1989).

[32]   Dore, S.P., Krupadas, S., Borgonha, S., Kurpad, A.V.: The 13-C urea breath test to assess helicobacter pylori infection in school children. National Medical Journal of India 10(2), 57–60 (1997).

[33]   Douglas, D.J., Konenkov, N.V.: Influence of the 6th and 10th spatial harmonics on the peak shape of a quadrupole mass filter with round rods. Rapid Communications in Mass Spectrometry 16(2), 1425–1431 (2002).

[34]   Du, Z., Douglas, D.J., Konenkov, N.: Elemental analysis with quadrupole mass filters operated in higher stability regions. Journal of Analytical Atomic Spectrometry 14(8), 1111–1119 (1999).

[35]   Dunning, F.B.: Study of low-energy electron-molecule interactions using rydberg atoms. Journal of Physical Chemistry 91(9), 2244–2249 (1987).

[36]   Ellefson, R.E., Moddeman, W.E., Dylla, H.F.: Hydrogen isotope analysis of quadrupole mass spectrometry. Journal of vacuum science & technology 18(3), 1062–1067 (1980).

[37]   Fetter, A.L., Walecka, J.D.: Theoretical Mechanics of Particles and Continua. Courier Dover Publications (2003).

[38]   Field, F.H., Franklin, J.L.: Electron Impact Phenomena and the Properties of Gaseous Ions. Academic Press, New York., vol 1, 110 (1957).

[39]   Frattolillo, A., Ninno, A.D.: A powerful tool to quantitatively detect tiny amounts of in a deuterium rich background for fusion research (2007).

[40]   Gibson, J., Taylor, S., Leck, J.H.: Detailed simulation of mass spectra for quadrupole mass spectrometer systems. Journal of Vacuum Science and Technology A: Vacuum, Surfaces and Films 18(1), 237–243 (2000).

[41]   Gibson, J.R., Evans, K.G., Taylor, S.: Modelling mass analyzer performance with fields determined using the boundary element method. Journal of Mass Spectrometry 45, 364–371 (2010).

[42]   Gibson, J.R., Taylor, S.: Prediction of quadrupole mass filter performance for hyperbolic and circular cross section electrodes. Rapid Communications in Mass Spectrometry 14(18), 1669–1673 (2000).

[43]   Gibson, J.R., Taylor, S.: Numerical investigation of the effect of electrode size on the behaviour of quadrupole mass filters. Rapid Communications in Mass Spectrometry 15(20), 1960–1964 (2001).

[44]   Gross, J.H.: Mass Spectrometry: A textbook. Springer (2004) 141.

[45] Guth, E., Mullin, C.J.: Electron emission of metals in electric fields iii. The transition from thermionic to cold emission. Physical Review 61(5-6), 339–348 (1942).

[46] Herbert, C.G., Johnstone, R.A.: Mass Spectrometry Basics. Boca Raton ; London: CRC Press (c2003).

[47] Herman, J.A., Harrison, A.G.: Effect of reaction exothermicity on the proton transfer chemical ionization mass spectra of isomeric C5 and C6 alkanols. Canadian Journal of Chemistry 59, 2125–2132 ((1981).

[48] Hiroki, S., Abe, T., Murakami, Y.: Development of a quadrupole mass spectrometer using the second stable zone in Mathieu's stability diagram. Review of Scientific Instruments 62(9), 2121–2124 (1991).

[49] Hiroki, S., Abe, T., Murakami, Y.: Separation of helium and deuterium peaks with a quadrupole mass spectrometer by using the second stability zone in the mathieu diagram. Review of Scientific Instruments 63(8), 3874–3876 (1992).

[50] Hiroki, S., Abe, T., Murakami, Y.: Detection of a 10-4 helium peak in a deuterium atmosphere using a modified high-resolution quadrupole mass spectrometer. Review of Scientific Instruments 65(6), 1912–1917 (1994).

[51] Hiroki, S., Abe, T., Murakami, Y.: Sensitive helium leak detection in a deuterium atmosphere using a high-resolution quadrupole mass spectrometer. Vacuum 47(6-8), 767–769 (1996).

[52] Hogan, T.J., Taylor, S.: Effects of mechanical tolerances on QMF performance for operation in the third stability zone. IEEE Transactions on Instrumentation and Measurement., submitted Sept., 2008, accepted June, 2009.

[53] Hogan, T.J., Taylor, S.: Performance simulation of a quadrupole mass filter operating in the first and third stability zones. IEEE Transactions on Instrumentation and Measurement 57(3), 498–508 (2008).

[54] Hu, Q., Noll, R.J., Li, H., Makarov, A., Hardman, M., Cooks, R.G.: The orbitrap: A new mass spectrometer. Journal of Mass Spectrometry 40(4), 430–443 (2005).

[55] Hwang, W., Kim, Y.K., Rudd, M.E.: New model for electron-impact ionization cross sections of molecules. Journal of Chemical Physics 104(8), 2956–2966 (1996).

[56] Inokuti, M.: Inelastic collisions of fast charged particles with atoms and molecules-the bethe theory revisited. Reviews of Modern Physics 43(3), 297–347 (1971).

[57] Inokuti, M., Itikawa, Y., Turner, J.E.: Addenda: Inelastic collisions of fast charged particles with atoms and molecules-the bethe theory revisited. Reviews of Modern Physics 50(1), 23–35 (1978) 142.

142

[58] Irikura, K.K., Ali, M.A., Kim, Y.K.: Electron-impact total ionization crosssections of the chlorofluoromethanes. International Journal of Mass Spectrometry 222(1-3), 189–200 (2003).

[59] Kaye, G.W.C., Laby, T.H.: Tables of Physical and Chemical constants and some Mathematical Functions. London and New York: Longman (1986).

[60] Kim, Y.K., Ali, M.A., Rudd, M.E.: Electron-impact total ionization cross sections of ch and c2h2. Journal of Research of the National Institute of Standards and Technology 102(6), 693–695 (1997).

[61] Kim, Y.K., Hwang, W., Weinberger, N.M., Ali, M.A., Rudd, M.E.: Electronimpact ionization cross sections of atmospheric molecules. Journal of Chemical Physics 106(3), 1026–1033 (1997).

[62] Kim, Y.K., Johnson, W.R., Rudd, M.E.: Cross sections for singly differential and total ionization of helium by electron impact. Physical Review A - Atomic, Molecular, and Optical Physics 61(3), 347,021–347,024 (2000).

[63] Kim, Y.K., Rudd, M.E.: Binary-encounter-dipole model for electron-impact ionization. Physical Review A 50(5), 3954–3967 (1994).

[64] Kim, Y.K., Rudd, M.E.: Comments on 'electron impact ionization of methane'. Journal of Physics B: Atomic, Molecular and Optical Physics 33(10), 1981–1984 (2000).

[65] Kim, Y.K., Santos, J.P., Parente, F.: Extension of the binary-encounter-dipole model to relativistic incident electrons. Physical Review A - Atomic, Molecular, and Optical Physics 62(5), 052,710–052,711 (2000).

[66] Kolesnikov, T., Lee, A.: Helicobacter pylori. Bailliere Tindall (1998).

[67] Kujawinski, E.B., Hatcher, P.G., Freitas, M.A.: High-resolution fourier transform ion cyclotron resonance mass spectrometry of humic and fulvic acids: Improvements and comparisons. Analytical Chemistry 74(2), 413–419 (2002).

[68] Kwon, D.H., Rhee, Y.J., Kim, Y.K.: Cross sections for ionization of mo and mo+ by electron impact. International Journal of Mass Spectrometry 245(1-3), 26–35 (2005).

[69] Landau, L.D., Lifshitz, E.M.: Quantum mechanics: non-relativistic theory. Butterworth-Heinemann (1991).

[70] Logan, R.P.H.: Urea breath tests in the management of helicobacter pylori infection. Gut 43(SUPPL. 1), S47–S50 (1998).

[71] Ma, F.M., Taylor, S.: Simulation of ion trajectories through the mass filter of a quadrupole mass spectrometer. IEE Proceedings: Science, Measurement and Technology 143(1), 71–76 (1996) 143.

[72] Mamyrin, B.A.: Time-of-flight mass spectrometry (concepts, achievements, and prospects). International Journal of Mass Spectrometry 206(3), 251–266 (2001).

[73] March, R.E.: An introduction to quadrupole ion trap mass spectrometry. Journal of Mass Spectrometry 32(4), 351–369 (1997).

[74] March, R.E., Todd, J.F.J.: Quadrupole ion trap mass spectrometry. John Wiley and Sons, 1 - 23 (2005).

[75] Marshall, A.G., Hendrickson, C.L., Jackson, G.S.: Fourier transform ion cyclotron resonance mass spectrometry: A primer. Mass spectrometry reviews 17(1), 1–35 (1998).

[76] Marshall, B.: Helicobacter pylori: Past, present and future. Keio Journal of Medicine 52(2), 80–85 (2003).

[77] Marshall, B.: Helicobacter connections. ChemMedChem 1(8), 783–802 (2006).

[78] Massey, H.S.W., Burhop, E.H.S.: Electronic and Ionic Impact Phenomena. Oxford University Press, London (London) vol 1, 558 (1952).

[79] Masson, J.: The Atomic Theory of Lucretius. Contrasted with modern doctrines of atoms and evolution. Adegi Graphics LLC (2005).

[80] McDowell, C.A.: Mass spectrometry. Krieger, Huntington (N.Y.) (1979).

[81] McLachlan, N.W.: Theory and application of mathieu functions. New York : Dover (1964).

[82] Meldrum, A.N.: The development of the atomic theory. H. Milford, Oxford University Press (1920).

[83] Munson, M.S.B., Field, F.H.: Chemical ionization mass spectrometry. i. General introduction. Journal of the American Chemical Society 88(12), 2621–2630 (1966).

[84] Nachamkin, I., Skirrow, M.B.: Campylobacter, arcobacter and helicobacter. Systematic Bacteriology 9th Ed.V 2, 106-114 (1998).

[85] Nemchinsky, V.: Simple algorithm to calculate t-f electron emission current density. IEEE Transactions on Dielectrics and Electrical Insulation 11, 551–553 (2004).

[86] Nier, A.O.: Evidence for the existence of an isotope of potassium of mass 40[1]. Physical Review 48(3), 283–284 (1935).

[87] Nier, A.O.: A mass spectrometer for isotope and gas analysis. Review of Scientific Instruments 18(6), 398–411 (1947).

[88] Nishimura, H., Huo, W.M., Ali, M.A., Kim, Y.K.: Electron-impact total ionization cross sections of cf4, c2f6, and c3f8. Journal of Chemical Physics 110(8), 3811–3822 (1999) 144.

[89]   Paul, W.: Electromagnetic traps for charged and neutral particles. Reviews of Modern Physics 62(3), 531-540 (1990).

[90]   Pearce, C.G., Halsall, D.: A quadrupole mass filter with flat electrodes. International Journal of Mass Spectrometry and Ion Physics 27(1), 31–41 (1978).

[91]   Peeters, M.: Urea breath test: A diagnostic tool in the management of helicobacter pylori-related gastrointestinal diseases. Acta Gastro-Enterologica Belgica 61(3), 332–335 (1998).

[92]   Peter, G.J., Mller, N.: Partial Pressure Gauges. Inficon AG, LI 9496 Balzers, Liechtenstein.

[93]   Peterson, W.L.: Helicobacter pylori and peptic ulcer disease. New England Journal of Medicine 324(15), 1043–1048 (1991).

[94]   Povh, B., Rith, K., Scholz, C., Zetsche, F.: Particles and Nuclei: An Introduction to the Physical Concepts. Springer (2008).

[95]   Price, D.: Dynamic mass spectrometry, vols. I and III. Heyden, London (1970-1971).

[96]   Probst, M., Deutsch, H., Becker, K., Märk, T.D.: Calculations of absolute electron-impact ionization cross sections for molecules of technological relevance using the dm formalism. International Journal of Mass Spectrometry 206(1-2), 13–25 (2001).

[97]   Pullman, B.: The Atom in the History of Human Thought. Oxford University Press Inc (Dec 2001).

[98]   Richards, J.A., Huey, R.M., Hiller, J.: A new operating mode for the quadrupole mass filter. International Journal of Mass Spectrometry and Ion Physics 12(4), 317–339 (1973).

[99]   Richardson, O.W.: Thermionic Emission from Hot Bodies. Watchmaker Publishing (2003).

[100]   Rose, M., Johnstone, R.A.W.: Mass spectrometry for chemists and biochemists. Cambridge University Press, Cambridge (1982).

[101]   Schwartz, J.C., Senko, M.W., Syka, J.E.P.: A two-dimensional quadrupole ion trap mass spectrometer. Journal of the American Society for Mass Spectrometry 13(6), 659–669 (2002).

[102]   Siuzdak, G.: Mass Spectrometry for Biotechnology. Academic Press, San Diego (1996).

[103]   Spencer, N.D., Moore, J.H.: Encyclopedia of Chemical Physics and Physical Chemistry. Taylor & Francis (2001) 145.

[104] Srigengan, B., Gibson, J.R., Taylor, S.: Ion trajectories in quadrupole mass spectrometer with a static transverse magnetic field applied to mass filter. IEE Proceedings: Science, Measurement and Technology 147(6), 274–278 (2000).

[105] Stafford., G.C., Kelley, P.E., Syka, J.E.P., Reynolds, W.E., Todd, J.F.J.: Recent improvements in and analytical applications of advanced ion trap technology. International Journal of Mass Spectrometry and Ion Processes 60(1), 85–98 (1984).

[106] Stock, R.: Encyclopedia of Applied High Energy and Particle Physics. Wiley- VCH (2009).

[107] Stratton, K.R., Durch, J.S., Lawrence, R.S.: Vaccines for the 21st century : a tool for decisionmaking. Washington, D.C. : National Academy Press (2000).

[108] Syms, R.R.A., Tate, T.J., Ahmad, M.M., Taylor, S.: Design of a microengineered electrostatic quadrupole lens. IEEE Transactions on Electron Devices 45(11), 2304–2311 (1998).

[109] Taylor, S., Gibson, J.R.: Prediction of the effects of imperfect construction of a qms filter. Journal of Mass Spectrometry 43(5), 609–616 (2008).

[110] Thomson, J.J.: Rays of Positive Electricity and Their Application to Chemical Analysis. Longmans, Green & Co., Ltd., London (1913).

[111] Titov, V.V.: Isotopic quadrupole mass spectrometry of hydrogen and helium. Journal of Radioanalytical and Nuclear Chemistry 174(2), 205–222 (1993).

[112] T.J.Hogan: QMS2- Hyperbolic User Guide, 1 edn. (2006).

[113] T.J.Hogan: QMS2- Field User Guide, 1 edn. (2007).

[114] Todd, J.F.J.: Recommendations for nomenclature and symbolism for mass spectroscopy. International Journal of Mass Spectrometry and Ion Processes 142(3), 209–240 (1995).

[115] Tunstall, J.J., Voo, A.C.C., Taylor, S.: Computer simulation of the mass filter for a finite length quadrupole. Rapid Communications in Mass Spectrometry 11(2), 184–188 (1997).

[116] Versalovic, J., Fox, J.G.: Helicobacter. Manual of Clinical Microbiology pp.727–738 (1999).

[117] Voo, A.C.C., Ng, R., Tunstall, J.J., Taylor, S.: Transmission through the quadrupole mass spectrometer mass filter: The effect of aperture and harmonics. Journal of Vacuum Science and Technology A: Vacuum, Surfaces and Films 15(4), 2276–2281 (1997).

[118] Vriens, L.: Binary-encounter electron-atom collision theory. Physical Review 141(1), 88–92 (1966) 146.

[119] Wollnik, H.: Time-of-flight mass analyzers. Mass spectrometry reviews 12(2), 89–114 (1993).

Appendix A

Pressure Dependence QMS2- *EI* Ion Source Model Source Code

```cpp
// pressure_dependenceDlg.cpp : implementation file
    #include "stdafx.h"
    #include "pressure_dependence.h"
    #include "pressure_dependenceDlg.h"
    #include "math.h"
    #ifdef _DEBUG
    #define new DEBUG_NEW
    #undef THIS_FILE
    static char THIS_FILE[] = __FILE__;
    #endif
    /////////////////////////////////////////////////////////////
    // CAboutDlg dialog used for App About
    class CAboutDlg : public CDialog
    {
    public:
    CAboutDlg();
    // Dialog Data
    //{{AFX_DATA(CAboutDlg)
    enum { IDD = IDD_ABOUTBOX };
    //}}AFX_DATA
    // ClassWizard generated virtual function overrides
    //{{AFX_VIRTUAL(CAboutDlg)
    protected:
    virtual void DoDataExchange(CDataExchange* pDX);
    //}}AFX_VIRTUAL
    // Implementation
    protected:
    //{{AFX_MSG(CAboutDlg)
    //}}AFX_MSG
    DECLARE_MESSAGE_MAP()
    };
```

```
CAboutDlg::CAboutDlg() : CDialog(CAboutDlg::IDD)
{
//{{AFX_DATA_INIT(CAboutDlg)
//}}AFX_DATA_INIT
}
void CAboutDlg::DoDataExchange(CDataExchange* pDX)
{
CDialog::DoDataExchange(pDX);
//{{AFX_DATA_MAP(CAboutDlg)
//}}AFX_DATA_MAP
}
BEGIN_MESSAGE_MAP(CAboutDlg, CDialog)
//{{AFX_MSG_MAP(CAboutDlg)
// No message handlers
//}}AFX_MSG_MAP
END_MESSAGE_MAP()
////////////////////////////////////////////////////////
// CPressure_dependenceDlg dialog
CPressure_dependenceDlg::CPressure_dependenceDlg(CWnd*
    pParent /*=NULL*/)
: CDialog(CPressure_dependenceDlg::IDD, pParent)
{
//{{AFX_DATA_INIT(CPressure_dependenceDlg)
m_pressurea = _T("");
m_temperature = _T("");
m_molecular = _T("");
m_moleculesnumber = _T("");
m_filament = _T("");
m_coilcurrent = _T("");
m_accelerating = _T("");
m_turns = _T("");
m_chamberlength = _T("");
m_pathlength = _T("");
m_operation = -1;
m_electron = _T("");
m_calc = _T("");
m_selection = -1;
m_emission = _T("");
m_ioniccurrent = _T("");
//}}AFX_DATA_INIT
// Note that LoadIcon does not require a subsequent
    //DestroyIcon in Win32
m_hIcon = AfxGetApp()->LoadIcon(IDR_MAINFRAME);
}
void CPressure_dependenceDlg::DoDataExchange(CDataExchange* pDX)
{
```

```
CDialog::DoDataExchange(pDX);
//{{AFX_DATA_MAP(CPressure_dependenceDlg)
DDX_Control(pDX, IDC_EDIT14, m_ioniccurrent1);
DDX_Control(pDX, IDC_EDIT13, m_emission1);
DDX_Control(pDX, IDC_EDIT12, m_calc1);
DDX_Control(pDX, IDC_EDIT11, m_electron1);
DDX_Control(pDX, IDC_EDIT10, m_pathlength1);
DDX_Control(pDX, IDC_EDIT9, m_chamberlength1);
DDX_Control(pDX, IDC_EDIT8, m_turns1);
DDX_Control(pDX, IDC_EDIT7, m_accelerating1);
DDX_Control(pDX, IDC_EDIT6, m_coilcurrent1);
DDX_Control(pDX, IDC_EDIT5, m_filament1);
DDX_Control(pDX, IDC_EDIT4, m_moleculesnumber1);
DDX_Control(pDX, IDC_EDIT3, m_molecular1);
DDX_Control(pDX, IDC_EDIT2, m_temperature1);
DDX_Control(pDX, IDC_EDIT1, m_pressurea1);
DDX_Text(pDX, IDC_EDIT1, m_pressurea);
DDX_Text(pDX, IDC_EDIT2, m_temperature);
DDX_Text(pDX, IDC_EDIT3, m_molecular);
DDX_Text(pDX, IDC_EDIT4, m_moleculesnumber);
DDX_Text(pDX, IDC_EDIT5, m_filament);
DDX_Text(pDX, IDC_EDIT6, m_coilcurrent);
DDX_Text(pDX, IDC_EDIT7, m_accelerating);
DDX_Text(pDX, IDC_EDIT8, m_turns);
DDX_Text(pDX, IDC_EDIT9, m_chamberlength);
DDX_Text(pDX, IDC_EDIT10, m_pathlength);
DDX_Radio(pDX, IDC_RADIO1, m_operation);
DDX_Text(pDX, IDC_EDIT11, m_electron);
DDX_Text(pDX, IDC_EDIT12, m_calc);
DDX_Radio(pDX, IDC_RADIO3, m_selection);
DDX_Text(pDX, IDC_EDIT13, m_emission);
DDX_Text(pDX, IDC_EDIT14, m_ioniccurrent);
//}}AFX_DATA_MAP
}
BEGIN_MESSAGE_MAP(CPressure_dependenceDlg, CDialog)
//{{AFX_MSG_MAP(CPressure_dependenceDlg)
ON_WM_SYSCOMMAND()
ON_WM_PAINT()
ON_WM_QUERYDRAGICON()
ON_BN_CLICKED(IDC_BUTTON1, OnButton1)
ON_BN_CLICKED(IDC_RADIO1, OnRadio1)
ON_BN_CLICKED(IDC_RADIO2, OnRadio2)
ON_BN_CLICKED(IDC_RADIO3, OnRadio3)
ON_BN_CLICKED(IDC_RADIO4, OnRadio4)
ON_BN_CLICKED(IDC_BUTTON2, OnButton2)
//}}AFX_MSG_MAP
```

```
END_MESSAGE_MAP()
//////////////////////////////////////////////////////////
// CPressure_dependenceDlg message handlers
BOOL CPressure_dependenceDlg::OnInitDialog()
{
CDialog::OnInitDialog();
// Add "About..." menu item to system menu.
// IDM_ABOUTBOX must be in the system command range.
ASSERT((IDM_ABOUTBOX & 0xFFF0) == IDM_ABOUTBOX);
ASSERT(IDM_ABOUTBOX < 0xF000);
CMenu* pSysMenu = GetSystemMenu(FALSE);
if (pSysMenu != NULL)
{
  CString strAboutMenu;
      strAboutMenu.LoadString(IDS_ABOUTBOX);
      if (!strAboutMenu.IsEmpty())
      {
      pSysMenu->AppendMenu(MF_SEPARATOR);
      pSysMenu->AppendMenu(MF_STRING,IDM_ABOUTBOX,strAboutMenu);
  }
}
// Set the icon for this dialog.
    // The framework does this automatically
// when the application's main window is not a dialog
SetIcon(m_hIcon, TRUE); // Set big icon
SetIcon(m_hIcon, FALSE); // Set small icon
// TODO: Add extra initialization here
return TRUE; //return TRUE unless you set focus to a control
}
void CPressure_dependenceDlg::OnSysCommand(UINT nID,LPARAM lParam)
{
if ((nID & 0xFFF0) == IDM_ABOUTBOX)
{
CAboutDlg dlgAbout;
dlgAbout.DoModal();
}
else
{
CDialog::OnSysCommand(nID, lParam);
}
}
/* If you add a minimize button to your dialog,
   you will need the code below
   to draw the icon.  For MFC applications using the
   document/view model, this is automatically done for
   you by the framework. */
```

```
void CPressure_dependenceDlg::OnPaint()
{
if (IsIconic())
{
CPaintDC dc(this); // device context for painting
SendMessage(WM_ICONERASEBKGND,(WPARAM)dc.GetSafeHdc(),0);
// Center icon in client rectangle
int cxIcon = GetSystemMetrics(SM_CXICON);
int cyIcon = GetSystemMetrics(SM_CYICON);
CRect rect;
GetClientRect(&rect);
int x = (rect.Width() - cxIcon + 1) / 2;
int y = (rect.Height() - cyIcon + 1) / 2;
// Draw the icon
dc.DrawIcon(x, y, m_hIcon);
}
else
{
CDialog::OnPaint();
}
}
// The system calls this to obtain the cursor to display
// while the user drags the minimized window.
HCURSOR CPressure_dependenceDlg::OnQueryDragIcon()
{
return (HCURSOR) m_hIcon;
}
void CPressure_dependenceDlg::OnButton1()
{
    CString st;
    float d,sp,t,mw,spa,r,mwa,den,den1,den2,av;
    char buffer1[10];
    r = 0.08206;
    av = 6.0221415 * pow(10,(23));
    m_pressure1.GetWindowText(st);
    sp = (float)atof(st);
    m_temperature1.GetWindowText(st);
    t = (float)atof(st);
    m_molecular1.GetWindowText(st);
    mw = (float)atof(st);
    spa = sp * 1.3158 * pow(10,(-3));
    mwa = r / mw;
    den = (spa) / (mwa * t);
    den1 = den / mw;
    den2 = den1 / 0.001;
    d = den2 * av; //expression to calculate
```

```
        _gcvt(d,8,buffer1); //calculated mc1 is stored in buffer
        m_moleculesnumber1.SetWindowText(buffer1);
        //displays buffer in the third text box
FILE *jey1;
jey1 = fopen("jey1.txt","w");
fprintf(jey1,"QMS-Pressure Dependence Ion Source Model Results\n");
fprintf(jey1,"-------------------------------------------------\n");
fprintf(jey1,"\n");
fprintf(jey1,"\n");
fprintf(jey1,"Density of Molecules in ionization Chamber=%f\n",d);
fclose(jey1); //close the file
fclose(jey1); //close the file
}
void CPressure_dependenceDlg::calculate()
{
float lf,nt,fc,dfa,av,b,lmax,pi,cl,f;
double len;
        pi = 3.14159265;
        UpdateData();
        if( m_filament.IsEmpty() )
    lf = 0;
else
lf = atof(m_filament);
        if( m_turns.IsEmpty() )
nt = 0;
else
nt = atof(m_turns);
        if( m_coilcurrent.IsEmpty() )
fc = 0;
else
fc = atof(m_coilcurrent);
        if( m_accelerating.IsEmpty() )
av = 0;
else
av = atof(m_accelerating);
        if( m_chamberlength.IsEmpty() )
cl = 0;
else
cl = atof(m_chamberlength);
switch(m_operation)
{
case 0:
        b = (4*pi*pow(10,(-7))*fc*pow(10,(-3))*nt)/
            (lf*pow(10,(-3)));
        f = b*pow(10,(4));
        lmax = (cl*(1+(1.1*pow(10,(-4))*lf*lf*f*f)/av))*
```

```
                   pow(10,(-2));
          len = lmax;
          break;
case 1:
          len = cl * pow(10,(-2));
          break;
}
m_pathlength.Format("%.2f", len);
UpdateData(FALSE);
}
void CPressure_dependenceDlg::OnRadio1()
{
calculate();
}
void CPressure_dependenceDlg::OnRadio2()
{
calculate();
}
void CPressure_dependenceDlg::calculategas()
{
    double orbi,orbia,orbib,orbic,orbid;
    double sx,nx,bx,a,r,tx,e,ux,kx,lx,mx,orbi1a,jx;
    double sy,ny,by,ty,uy,ky,ly,my,orbi2a,jy;
    double sz,nz,bz,tz,uz,kz,lz,mz,orbi3a,jz;
    double sxb,nxb,bxb,txb,uxb,kxb,lxb,mxb,orbi1b,jxb;
    double syb,nyb,byb,tyb,uyb,kyb,lyb,myb,orbi2b,jyb;
    double szb,nzb,bzb,tzb,uzb,kzb,lzb,mzb,orbi3b,jzb;
    double sxc,nxc,bxc,txc,uxc,kxc,lxc,mxc,orbi1c,jxc;
    double syc,nyc,byc,tyc,uyc,kyc,lyc,myc,orbi2c,jyc;
    double szc,nzc,bzc,tzc,uzc,kzc,lzc,mzc,orbi3c,jzc;
    double sxd,nxd,bxd,txd,uxd,kxd,lxd,mxd,orbi1d,jxd;
    double syd,nyd,byd,tyd,uyd,kyd,lyd,myd,orbi2d,jyd;
    double szd,nzd,bzd,tzd,uzd,kzd,lzd,mzd,orbi3d,jzd;
    a = 0.5293;
    r = 13.61;
    // orbit 3p2
    nx = 2;
    bx = 22.7356;
    kx = 87.4876;
    mx = 3;
    ny = 3;
    by = 22.8087;
    ky = 87.6014;
    my = 3;
    nz = 1;
    bz = 4.2113;
```

```
kz = 7.2572;
mz = 4;
// orbit 3p0
nxb = 1;
bxb = 23.6239;
kxb = 88.9012;
mxb = 3;
nyb = 4;
byb = 22.5449;
kyb = 86.6817;
myb = 3;
nzb = 1;
bzb = 4.0365;
kzb = 7.2685;
mzb = 4;
// orbit 3p1
nxc = 1.794;
bxc = 22.8887;
kxc = 88.3002;
mxc = 3;
nyc = 3.206;
byc = 22.7707;
kyc = 87.6959;
myc = 3;
nzc = 1;
bzc = 4.1360;
kzc = 6.8174;
mzc = 4;
// orbit 1p1
nxd = 1.183;
bxd = 23.4427;
kxd = 89.0905;
mxd = 3;
nyd = 3.817;
byd = 22.7206;
kyd = 87.6420;
myd = 3;
nzd = 1;
bzd = 3.9309;
kzd = 5.8443;
mzd = 4;
UpdateData();
if( m_electron.IsEmpty() )
e = 0;
else
e = atof(m_electron);
```

```
switch(m_selection)
    {
    case 0:
        sx = 4 * 3.14159265 * a * a * nx * (r / bx) * (r / bx);
        tx = e / bx;
        ux = kx / bx;
        lx = (sx) / (tx + ((ux + 1) / mx));
        jx = (((log(tx))/2)*(1-(1/(tx*tx))))+1-
            (1/tx)-((log(tx))/(tx+1));
        orbi1a = lx * jx;
        sy = 4 * 3.14159265 * a * a * ny * (r / by) * (r / by);
        ty = e / by;
        uy = ky / by;
        ly = (sy) / (ty + ((uy + 1) / my));
        jy = (((log(ty))/2)*(1-(1/(ty*ty))))+1-(1/ty)-
            ((log(ty))/(ty+1));
        orbi2a = ly * jy;
        sz = 4 * 3.14159265 * a * a * nz * (r / bz) * (r / bz);
        tz = e / bz;
        uz = kz / bz;
        lz = (sz) / (tz + ((uz + 1) / mz));
        jz = (((log(tz))/2)*(1-(1/(tz*tz))))+1-
            (1/tz)-((log(tz))/(tz+1));
        orbi3a = lz * jz;
        // orbit 3p0
        sxb = 4 * 3.14159265 *a*a*nxb* (r/bxb) * (r/bxb);
        txb = e / bxb;
        uxb = kxb / bxb;
        lxb = (sxb) / (txb + ((uxb + 1) / mxb));
        jxb = (((log(txb))/2)*(1-(1/(txb*txb))))+1-
                (1 / txb) - ((log (txb)) / (txb + 1));
        orbi1b = lxb * jxb;
        syb = 4 * 3.14159265 *a*a*nyb* (r/byb)*(r/byb);
        tyb = e / byb;
        uyb = kyb / byb;
        lyb = (syb) / (tyb + ((uyb + 1) / myb));
        jyb = (((log (tyb)) / 2) * (1 - (1 / (tyb * tyb)))) +
            1 - (1 / tyb) - ((log (tyb)) / (tyb + 1));
        orbi2b = lyb * jyb;
        szb = 4 * 3.14159265 *a*a*nzb*(r/bzb)*(r/bzb);
        tzb = e / bzb;
        uzb = kzb / bzb;
        lzb = (szb) / (tzb + ((uzb + 1) / mzb));
        jzb = (((log (tzb)) / 2) * (1 - (1 / (tzb * tzb)))) +
            1 - (1 / tzb) - ((log (tzb)) / (tzb + 1));
        orbi3b = lzb * jzb;
```

156

```
// orbit 3p1
sxc = 4 * 3.14159265 * a * a * nxc * (r / bxc) * (r / bxc);
txc = e / bxc;
uxc = kxc / bxc;
lxc = (sxc) / (txc + ((uxc + 1) / mxc));
jxc = (((log (txc)) / 2) * (1 - (1 / (txc * txc)))) +
    1 - (1 / txc) - ((log (txc)) / (txc + 1));
orbi1c = lxc * jxc;
syc = 4 * 3.14159265 * a * a * nyc * (r / byc) * (r / byc);
tyc = e / byc;
uyc = kyc / byc;
lyc = (syc) / (tyc + ((uyc + 1) / myc));
jyc = (((log (tyc)) / 2) * (1 - (1 / (tyc * tyc)))) +
        1 - (1 / tyc) - ((log (tyc)) / (tyc + 1));
orbi2c = lyc * jyc;
szc = 4 * 3.14159265 * a * a * nzc * (r / bzc) * (r / bzc);
tzc = e / bzc;
uzc = kzc / bzc;
lzc = (szc) / (tzc + ((uzc + 1) / mzc));
jzc = (((log (tzc)) / 2) * (1 - (1 / (tzc * tzc)))) + 1 -
    (1 / tzc) - ((log (tzc)) / (tzc + 1));
orbi3c = lzc * jzc;
// orbit 1p1
sxd = 4 * 3.14159265 * a * a * nxd * (r / bxd) * (r / bxd);
txd = e / bxd;
uxd = kxd / bxd;
lxd = (sxd) / (txd + ((uxd + 1) / mxd));
jxd = (((log (txd)) / 2) * (1 - (1 / (txd * txd)))) + 1 -
    (1 / txd) - ((log (txd)) / (txd + 1));
orbi1d = lxd * jxd;
syd = 4 * 3.14159265 * a * a * nyd * (r / byd) * (r / byd);
tyd = e / byd;
uyd = kyd / byd;
lyd = (syd) / (tyd + ((uyd + 1) / myd));
jyd = (((log (tyd)) / 2) * (1 - (1 / (tyd * tyd)))) + 1 -
    (1 / tyd) - ((log (tyd)) / (tyd + 1));
orbi2d = lyd * jyd;
szd = 4 * 3.14159265 * a * a * nzd * (r / bzd) * (r / bzd);
tzd = e / bzd;
uzd = kzd / bzd;
lzd = (szd) / (tzd + ((uzd + 1) / mzd));
jzd = (((log (tzd)) / 2) * (1 - (1 / (tzd * tzd)))) + 1 -
    (1 / tzd) - ((log (tzd)) / (tzd + 1));
orbi3d = lzd * jzd;
orbia = orbi1a + orbi2a + orbi3a;
orbib = orbi1b + orbi2b + orbi3b;
```

```
            orbic = orbi1c + orbi2c + orbi3c;
            orbid = orbi1d + orbi2d + orbi3d;
            orbi = (orbia + orbib + orbic + orbid) / 4;
            break;
        case 1:
            orbi = e * 0;
            break;
}
m_calc.Format("%.2f", orbi);
UpdateData(FALSE);
}
void CPressure_dependenceDlg::OnRadio3()
{
calculategas();
}
void CPressure_dependenceDlg::OnRadio4()
{
calculategas();
}
void CPressure_dependenceDlg::OnButton2()
{
CString st;
        float em,mo,pa,ca,ion;
        char buffer1[10];
        m_emission1.GetWindowText(st);
        em = (float)atof(st);
        m_moleculesnumber1.GetWindowText(st);
        mo = (float)atof(st);
        m_pathlength1.GetWindowText(st);
        pa = (float)atof(st);
        m_calc1.GetWindowText(st);
        ca = (float)atof(st);
        ion = em * pow(10,(-3)) * mo * pa * ca * pow(10,(-20)) * 0.0001;
        _gcvt(ion,8,buffer1);
        m_ioniccurrent1.SetWindowText(buffer1);
}
```

Appendix B

Curriculum Vitae

Educational Qualifications

Ph.D. – September 2010
Title of the Thesis : Portable Mass Spectrometry for Residual Gas Analysis
University Of Liverpool
Liverpool, United Kingdom

M.Sc.(Eng) Micro and Nano Technology
September 2007 – First class
University Of Liverpool
Liverpool, United Kingdom

B.E.(Electrical and Electronics Engineering)
 May 2006 – First class with Distinction
R.M.D. Engineering College, Affiliated to Anna University (AU)
Tamil Nadu, India

HSC
March 2002 – First class with Distinction
G.K.Shetty Hindu Vidyalaya
State Board of School Examinations, Tamil Nadu, India

SSLC
March 2000 –First class with Distinction
G.K.Shetty Hindu Vidyalaya, State Board of Matriculation Examination
Tamil Nadu, India
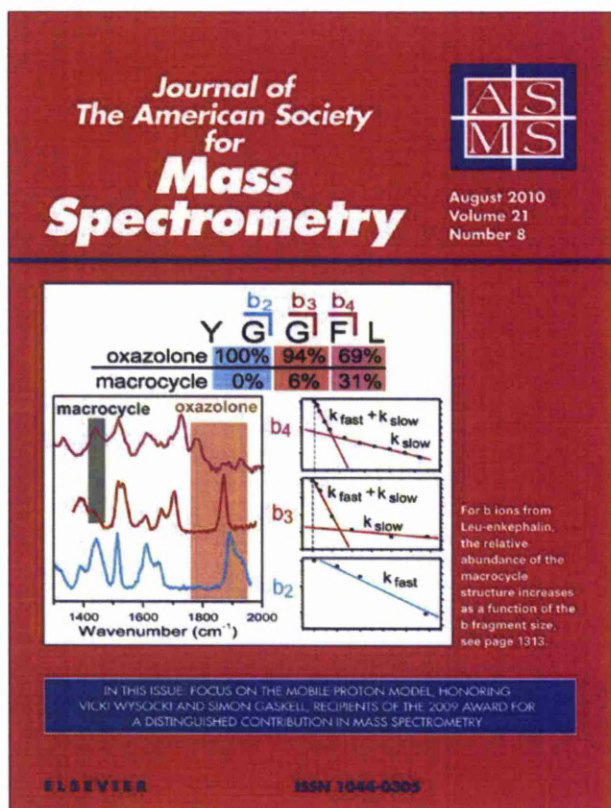
Appendix C

Publications

1. **J. Sreekumar**, T.J.Hogan, S.Taylor, P. Turner, and C. Knott, "A quadrupole mass spectrometer for resolution of low mass Isotopes", J Am Soc Mass Spectrom 2010, 21, 1364 –1370.

2. S.U.A.H. Syed, **J. Sreekumar**, B. Brkic, J. R. Gibson, and S.Taylor, "Effect of an axial magnetic field on the performance of a Quadrupole Mass Spectrometer", J Am Soc Mass Spectrom (2010).

3. **J. Sreekumar**, T.J.Hogan, and S.Taylor, "Simulation of a QMS including the effects of pressure in an electron impact ion source", J Am Soc Mass Spectrom (submitted).

4. S.U.A.H. Syed, **J. Sreekumar**, J. R. Gibson, and S.Taylor, "Behaviour of a QMS in the third stability zone with a transverse magnetic field applied", J Am Soc Mass Spectrom (submitted).

5. **J. Sreekumar**, B.Brkic, N.France, T.J.Hogan, J.R.Gibson, and S.Taylor, "Simulation of a QMS with an electron impact ion source including pressure dependence", British Mass Spectrometry Society (BMSS) Conference, York (2008).

6. **J. Sreekumar** and S.Taylor, "Modelling of a pressure dependence Electron Impact Ion Source QMS for Residual Gas Analysis", University research day, University of Liverpool, Liverpool (2009).

7. **J. Sreekumar**, T.J.Hogan, S.Taylor, P. Turner, and C. Knott, "Point of sample Quadrupole Mass Spectrometer (QMS) for the identification of low mass Isotopes", American Mass Spectrometry Society (ASMS) Conference, Philadelphia (2009).

8. **J. Sreekumar**, N. France, S. Taylor, T. Mathews, P. Turner, and A. Watson, "A portable mass spectrometer for *Helicobacterpylori* detection using a non-invasive carbon-13 urea breath test", Postgraduate Researchers In Science Medicine (PRISM) conference, Lancaster (2010).

9. **J. Sreekumar**, T.J.Hogan, and S.Taylor, "Modelling the effect of pressure in an electron impact ion source QMS for residual gas analysis", Mass Spectrometry @ Manchester Symposia, Manchester (2010).

10. S. Sarfaraz Uddin, B. Brkic, J. R. Gibson, **J. Sreekumar**, and S. Taylor, "Performance of an RGA with a transverse magnetic field applied to the mass filter, The 9th RGA Users Meeting", Daresbury Laboratory, Warrington (2010).

Award

Won best commendable research award for a paper presented at the Research in Progress Workshop, University of Liverpool (2009).

Journal of
The American Society
for
**Mass
Spectrometry**

A|S
M|S

August 2010
Volume 21
Number 8

IN THIS ISSUE: FOCUS ON THE MOBILE PROTON MODEL, HONORING
VICKI WYSOCKI AND SIMON GASKELL, RECIPIENTS OF THE 2009 AWARD FOR
A DISTINGUISHED CONTRIBUTION IN MASS SPECTROMETRY

ELSEVIER   ISSN 1044-0305

A Quadrupole Mass Spectrometer for Resolution of Low Mass Isotopes

Jeyan Sreekumar,[a] Thomas J. Hogan,[a] Stephen Taylor,[a] Phillip Turner,[b] and Christopher Knott[b]

[a] Department of Electrical Engineering and Electronics, University of Liverpool, Liverpool, United Kingdom
[b] AWE Aldermaston, Berkshire, United Kingdom

The qualitative and quantitative identification of low mass isotopes in the mass range 1–6 u poses certain difficulties when attempting to achieve the required resolution with an instrument suitable for deployment within a process environment. Certain adjacent species present in the process sample (HT and D_2) require a resolution greater than 930 to achieve an accurate measurement. We demonstrate here through simulation techniques that this level of performance required is unachievable using commercially available instruments. Using previously reported simulation techniques, this article demonstrates how the required performance for resolving the low mass isotopes can be achieved by a quadrupole mass spectrometer (QMS), which incorporates a quadrupole mass filter (QMF) constructed from hyperbolic electrodes and operated in zone 3 of the Mathieu stability diagram.   (J Am Soc Mass Spectrom 2010, 21, 1364–1370) © 2010 Published by Elsevier Inc. on behalf of American Society for Mass Spectrometry

Most commercial quadrupole mass spectrometers (QMS) utilize a quadrupole mass filter (QMF) based on circular rods and operate in stability zone 1 ($a = 0.237$, $q = 0.706$) [1]. A mass scan line that provides a mass resolution, which increases linearly with mass and commonly referred to as unit resolution, is the default mass scanning mode. There are a number of applications that require a high-resolution at the lower end of the mass range i.e., 1–6 u, where 1 atomic mass unit (u) = 1.6605×10^{-27} kg [2]. Example applications include the quantitative measurement of hydrogen isotopes in the presence of helium [3–6] and helium leak detection in a deuterium rich atmosphere [7]. For instance, to measure $^3He^+$ in the presence of HD^+ requires a minimum baseline resolution of 512 and for HT^+ in the presence of D_2^+, 930 is required. These resolutions are not readily achievable with commercial instruments suitable for deployment in a process environment. A list of the species and the resolutions to separate adjacent species is contained in Table 1.

General purpose instruments are also arranged to have relatively large mass ranges 100–300 u being common. These characteristics result in relatively coarse control of the mass step size, e.g., 64 mass steps/u is common [8]. The ability to achieve high-resolution quantitative measurements of closely spaced species requires a high number of data points or mass steps across the mass peaks. A small mass step size

imposes a reduced maximum mass due to the finite dynamic range of digital to analogue (d/a) converters in the control electronics. This relationship has been demonstrated by Day [8], who used a modified QMS to successfully baseline separate $^4He^+$ and D_2^+.

For a given length QMF the resolving power is dependent on the number of rf cycles the ion is exposed to on its passage through the QMF [9]. Typically 200 rf cycles are required in zone 1 to achieve a resolution of ≈1000, but this maximum is dependent on the overall accuracy of the QMF and the drive electronics, with any inaccuracies reducing this value [9]. For a QMF length of 300 mm, a 2 u ion with energy of 5 eV would be exposed to 75 cycles, and a 6 u ion to 120 cycles. Clearly, this is insufficient to achieve our required resolution described above, even with perfect electrode profiles, assembly, and voltage accuracies.

Stability zone 3 is a sloping rectangular area that provides two tips, one at the lower right ($a = 2.52$, $q = 2.82$), and the second at the upper left ($a = 3.16$, $q = 3.23$) corners that enable high-resolution mass scanning to be achieved.

With zone 3 the ions require exposure to a lower number of rf cycles to achieve the same resolution compared with zone 1 [9]. However, due to the higher Mathieu coefficients associated with zone 3, increased operating voltages are required. This, to some extent, is mitigated in this application by the limited maximum operating mass of 6 u that is required for hydrogen isotope measurement. Due to the much narrower stability zone the sensitivity of a zone 3 operating instrument is reduced (compared with a zone 1 QMS), with a reduction of a factor of 50 for He^+ being quoted by

Table 1. Minimum resolution required to discriminate between each of the species present

Species	Mass (Da)	Minimum resolution						
		H_2^+ 2.01565	$^3He^+$ 3.01602932	HD^+ 3.021926779	$^4He^+$ 4.002602	HT^+ 4.02387427	D_2^+ 4.0282036	T_2^+ 6.03209854
H_2^+	2.01565	NA	3.0	3.0	2.0	2.0	2.0	1.5
$^3He^+$	3.016029319	2.0	NA	512.4	4.1	4.0	4.0	2.0
HD^+	3.021926779	2.0	511.4	NA	4.1	4.0	4.0	2.0
$^4He^+$	4.002602	1.0	3.1	3.1	NA	189.2	157.3	3.0
HT^+	4.02387427	1.0	3.0	3.0	188.2	NA	930.5	3.0
D_2^+	4.028203558	1.0	3.0	3.0	156.3	929.5	NA	3.0
T_2^+	6.03209854	0.5	1.0	1.0	2.0	2.0	2.0	NA

Hiroki [10]. Hiroki also reported that the upper corner of zone 3 was the most suitable for high-resolution operation [5] but that the lower corner provided increased sensitivity.

Circular rods provide a more cost-effective route to implementing a QMF but suffer from reduced performance when compared to hyperbolic rods. Computer simulation has shown that when operating in zone 1, circular rods with $r/r_0 = 1.148$ suffer from increased peak width, lower transmission, and low mass tailing than hyperbolic rods [11]. More recent work has shown that this is also true when values of $r/r_0 = 1.125$ to 1.127 are used, which have been shown to give a better approximation to the quadrupole field than $r/r_0 = 1.148$ [12–14]. Using our simulation program QMS2, with 60 cycles of rf, a comparison of resolution at 10% peak height and transmission through QMS using filters are shown in Table 2. Performance degradation is further reduced when operating in zone 3 [15].

We have used our previously reported simulation techniques [15, 16] to investigate the factors that influence the ability of a QMS to achieve the performance necessary to separate HT^+ in the presence of D_2^+. Due to the demanding requirements of this application and for the reasons discussed above, the use of circular electrodes was felt to be inadequate for the performance required, and the results achieved in this study are based on a hyperbolic rod QMS. Our results show that frequency length product is a deciding factor in achieving the required resolution. It is also necessary for very accurate control of the mass scan line to ensure adequate abundance sensitivity. Further, we show that accurate alignment of the ion source to the QMF has to be achieved and this is more critical in the y-axis than in the x-axis due to the narrower shape of the y-stability area.

Table 2. Comparison of QMS resolution and transmission for values of $r/r0$ and hyperbolic electrodes

r/r0	R(M/ΔM)	T (%)
1.148	56.91	9.1
1.127	133	10.53
Hyperbolic	166.5	13.14

Theory

A QMF with four equally spaced electrodes of hyperbolic form produces a central electric field whose strength increases linearly with increasing displacement from the central axis and is independent in x and y (ideal quadrupole field). When driven by the correct combination of dc and ac voltages, the electrode assembly is capable of providing mass filtering action. With the voltages defined in eqs 1 and 2, the behavior of the ions as they pass through the QMF can be defined by the Mathieu eq 3 [1].

$$\Phi x = \frac{(U - V \cos \omega t)}{2} \tag{1}$$

$$\Phi y = \frac{-(U - V \cos \omega t)}{2} \tag{2}$$

$$\frac{d^2u}{d\xi^2} + (a_u - 2qu \cos (2\xi))u = 0 \tag{3}$$

where u = x or y and

$$a_u = a_x = -a_y = \frac{4eU}{m\omega^2 r_0^2} \tag{4}$$

$$q_u = q_x = -q_y = \frac{2eU}{m\omega^2 r_0^2} \tag{5}$$

Where m is the mass of the ion in kg, e is electron charge in coulombs, ω is angular frequency of the rf voltage V in MHz, r_0 is radius of the central field aperture in mm, U is dc component of the drive voltage in volts, and V is ac (rf) component of the drive voltage in volts.

Figure 1 shows the Mathieu stability diagram, which provides a graphical representation of the zones of the stable and unstable areas. This diagram shows the lowest three operating zones and for the purpose of this study we have examined zone 1 ($a = 0.237$, $q = 0.706$) and zone 3 ($a = 3.16$, $q = 3.23$).

The mass filtering action of the QMF is controlled by varying the U (dc) and V (rf) voltages. The voltage V
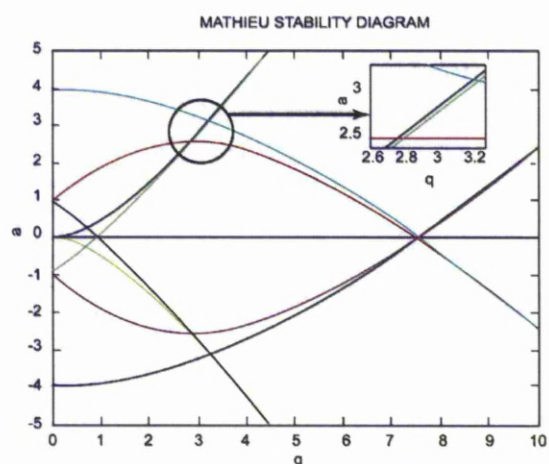
Figure 1. Mathieu stability diagram with zone 3 detail shown in the inset.

sets the position on the mass scale and the ratio of the U and V voltages controls the instrument resolution setting (η). Varying V and therefore U (while keeping the ratio of U to V constant) this changes the mass value that can successfully pass through the filter. This variation of the voltages is called the mass scan line. The ability of the QMF to provide the maximum achievable mass resolution is dependent on the number of rf cycles experienced by an ion. The number of rf cycles experienced by an ion can be defined by the following equation

$$N_c = \frac{Lf}{\sqrt{\dfrac{2eV_i}{m}}} \tag{6}$$

where N_c is the number of rf cycles experienced by an ion of mass m, L is length of the QMF in metres, f is frequency of rf excitation in MHz, e electron charge in coulombs, V_i is accelerating voltage in volts, and m is mass of ion in kg.

Method

Custom software (QMS2-Hyperbolic) was used to simulate the performance of hyperbolic electrode QMF. The program calculates ion trajectories by solving the Mathieu equations using a fourth order Runge-Kutta algorithm. Our approach has been described previously [15, 16]. Generation, display, and storage of mass spectra and individual ion trajectories, together with parametric sweep control, are provided by the QMS2-Hyperbolic program. A second program, QMS2-ION, generates the entry conditions for a large number of ions ($>10^7$), which are stored in an ion file, and these ions are transmitted along mass filter axis, i.e., ion

entrance angle is zero degrees. The number of ions (10^7) generated is simulated at each mass scan step. This file is read by QMS2-Hyperbolic providing a uniform ion distribution across the ion source radius R_s with each ion having random phase with respect to the rf at the time of entry into the QMF. Finally, MatLab was used to post process the data and for the generation of the graphical results.

Results and Discussion

Mass Spectral Studies for a HT$^+$ and D$_2^+$ Mixture

Reported here are the simulated mass spectra for a HT$^+$ and D$_2^+$ mixture using the computer simulation software described and operated at the upper left hand tip of stability zone 3 (a = 3.16 and q = 3.23). For zone 3, amplitude and length of high mass tail reduces as the frequency increases with corresponding improvement in abundance sensitivity. Increasing frequency also reduces low mass tail but the effect is minimal. As previously noted, hyperbolic electrodes provide superior performance in resolution and ion transmission for a given number of rf cycles than circular or other shaped electrodes e.g., rectangular [17, 18]. The simulated performance characteristics of a QMF constructed from hyperbolic electrodes are therefore investigated. Our tests indicate that only stability zone 3 is capable of being able to achieve the desired performance in the mass range in question (1–6 u). The mass difference between the two species is 0.004329288 u, requiring a minimum resolution of 930 for mass discrimination. Increasing the frequency improves the resolution measured at 10% of spectrum peak height (PH) and base line resolution but the 50% PH resolution only increases for a limited range of frequencies before limiting. Due to the closeness of the two species, a higher resolution is required to separate HT$^+$ and D$_2^+$ ions. A higher resolution can be achieved only in the upper half of the operational mass range. This is due to the number of rf cycles that the two species experience being very similar. As the ion mass increases the velocity through the QMF falls (for a given ion energy), this gives an increase in the number of rf cycles experienced and an increase in achievable resolution.

Figure 2a shows mass spectra for HT$^+$, at 10% PH showing a resolution of 914 at 4 MHz, increasing to 1257 at 8 MHz. The corresponding 50% PH resolution ranges from 1749 at the low-frequency end up to 1829 at 5 MHz and above. Figure 2b shows mass spectra for D$_2^+$ showing a slightly higher resolution: the 10% PH resolution ranges from 915 at the lowest frequency, up to a maximum of 1299 at 8 MHz. The 50% PH resolution was also correspondingly greater, with a minimum 1751 at 4 MHz increasing to 1918 at 6 MHz and above. As was the case for HD$^+$ the 50% PH resolution limits, with the higher mass D$_2^+$ limiting at a slightly higher value than for the lower mass HD$^+$. Both the low and

high mass tails for the two species are low, but with the high mass tail having much greater amplitude and mass range. A minimum resolution of 930 is required to separate these two species HT^+ and D_2^+. This is achievable with a length of 300 mm operating at a frequency of 5 MHz. By using the previous $L \times f$ relationship (eq 6), this should also be achievable with a length of 250 mm operating at 6 MHz. **Figure** 3 shows the mass spectra for equal abundances of HT^+ and D_2^+. As previously discussed, the high mass tail is the more dominant. Therefore the high mass tail of the HT^+ mass peak is the most likely to be the cause of inter species interference. The valley between the two peaks decreases with increasing frequency. At the lower frequency, the minimum point on the valley represents ~10% of peak height. For the highest frequency, this minimum drops to virtually zero.

Figure 4 shows typical mass spectra for D_2^+ for operation on zone 1 using the computer simulation software described. The mass peaks show both low and
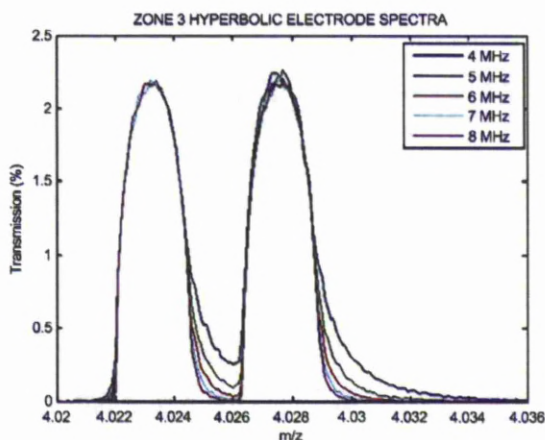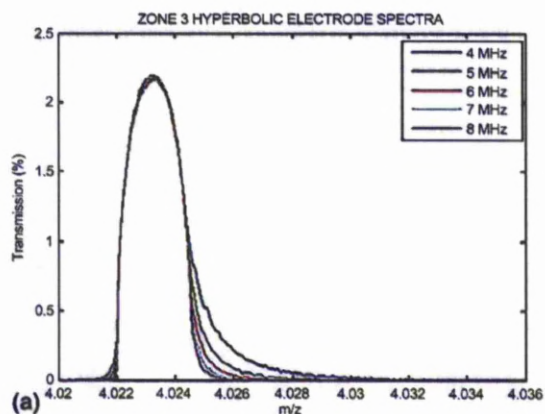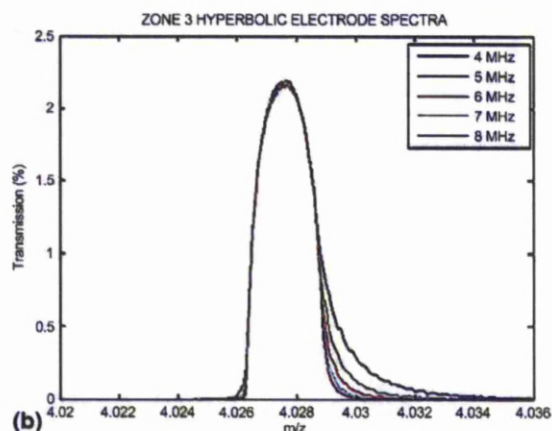

Figure 3. Variation of mass spectra with frequency for a hyperbolic electrode QMF (L = 300 mm, r_0 = 2.76 mm, Ei = 15 eV, ion source radius = 0.276 mm) for HT^+ and D_2^+ ions with equal abundance.

high mass tails, which are well formed. In this case (zone 1) the low mass tail is of greater amplitude and width than the high mass tail. The 10% PH resolution is significantly lower than obtained with zone 3 simulations. The resolution at the low-frequency end is 496, compared with 915 for zone 3. As the frequency is increased, the difference in resolution between the two zones decreases. For the two higher frequencies in this mass range, zone 1 achieves a maximum of 1751 at 8 MHz.

Effects of Drive Voltage Tolerance

Increasing the U and V drive voltages while keeping the ratio between them constant produces a constant reso-

Figure 2. Variation of HT^+ mass spectra with frequency for a hyperbolic electrode QMF (L = 300 mm, r_0 = 2.76 mm, Ei = 15eV, ion source radius = 0.276 mm) (a) and Variation of D_2^+ mass spectra with frequency for a hyperbolic electrode QMF (L = 300 mm, r_0 = 2.76 mm, Ei = 15eV, ion source radius = 0.276 mm) (b).
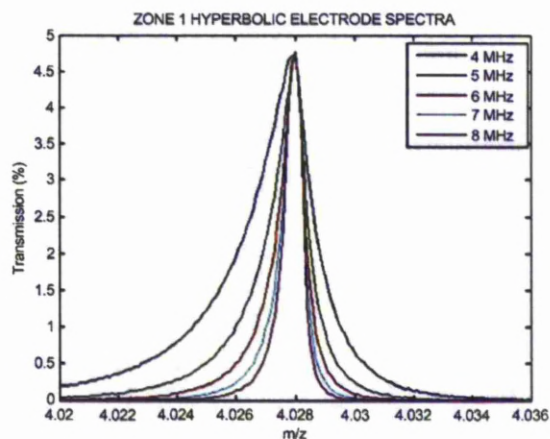

Figure 4. Variation of D_2^+ zone 1 mass spectra (L = 300 mm, r_0 = 2.76 mm, Ei = 3 eV, ion source radius 0.276 mm for a range of rf frequencies.

lution mass scan line (resolution proportional to mass). To achieve unit resolution the ratio of U/V is varied with increasing mass and results in a more complex scan generation system. A shift in the mass scan line is observed as the ratio between the U (dc) and V (rf) voltages varying which in turn results in a change to resolution and/or the mass calibration of the system. A very high instrument resolution η is achieved with the tight control of the drive voltages. Changes to either U or V independently results in a change to η and small changes to peak shape results with minor changes to the inter peak valley shape. These small peak shape changes can occur due to small changes in the U voltage. A greater change in instrument resolution η produced as the tolerance limits increases the error in the ratio of U and V voltages and therefore increasing movement in the position of the scan line relative to the mass stability regions. This increased change in mass scan line position results in increasing distortion of the mass peak. As this voltage error increases the individual peaks widen with an accompanying increase in peak height. The inter peak valley amplitude increases finally disappearing with the two peaks merging.

Figure 5a and b show simulated mass spectra for a HT^+ and D_2^+ mixture (50:50 ratio) for a range of negative U drive voltage errors and the inset in Figure 5a and b show a correct scan line condition at 0.0 V and an incorrect scan line condition at −0.1 V. Normally a reduction in DC drive voltage (negative voltage error) due to the power supply tolerances, results in an increase in ion transmission and a broadening of the mass peak resulting in a reduction in resolution. At the lower end of the voltage error range considered (up to −0.025 V) the observable changes in the mass peak are minimal and acceptable. Above this value the valley between the two species rises resulting in discrimination at 10% PH becoming unachievable and at a voltage error of 0.1 V the stability zones for the two species merge with the resultant superimposed peak emerging. At the negative voltage error of −0.1 V, the resolution has been reduced to a point where there is significant overlap between the stable zones of HT^+ and D_2^+ species as shown in the Figure 5b inset. This results in poor mass discrimination. For this position of the mass scan line both low and high mass species are transmitted resulting in higher transmission accompanied by the appearance of the central peak. The drive voltage tolerance limit is clearly at its most stringent at this part of the mass scan range due to high-resolution required to discriminate between HT^+ and D_2^+. To maintain this performance it is necessary to control the U/V ratio to very tight limits. The tolerance limits depend on the achievable mass resolution limit that can be obtained from the instrument.

Ion Source Positional Displacements

Previous research has characterized the dependence of QMF performance on electrode positional tolerance
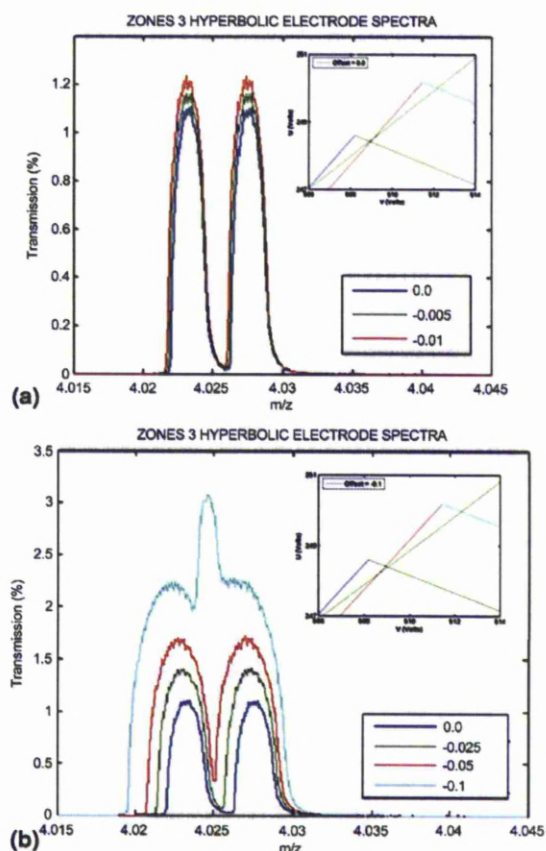

Figure 5. Mass spectra for a range of U voltage acceptable tolerances (volts) (a) acceptable tolerances (b) unacceptable tolerances. Inset shows scan line for (^{4}He 4.0026 u and D_2 4.0282). Overlap of zones gives large central peak.

[19]. Here we show the degradation in performance that occurs for a range of QMF to ion source misalignments. Correct alignment of the ion source with the central axis of the QMF is important to ensure maximum sensitivity. Misalignments of <0.2 mm (for an r_0 of 2.76 mm) results in a small reduction in the peak height (sensitivity) with barely discernible changes of the peak shape. For increasing misalignments the peak heights start to decrease significantly, decreasing by a factor of >2 for a displacement of 0.4 mm associated with an increasing narrowing of the peak width. Similar effects are observed for both x and y axis displacements. The y axis displacement results in greater decrease in peak height reflecting the narrower y-axis stable region of the QMF. We have also demonstrated that the effects of simultaneous x and y displacements are cumulative.

Figure 6a and b show mass spectra for a range of x and y-axis displacement of the ion source with respect to the QMF. Both x and y displacements exhibit similar characteristics with the y-axis displacement having the greater decrease in transmission for a
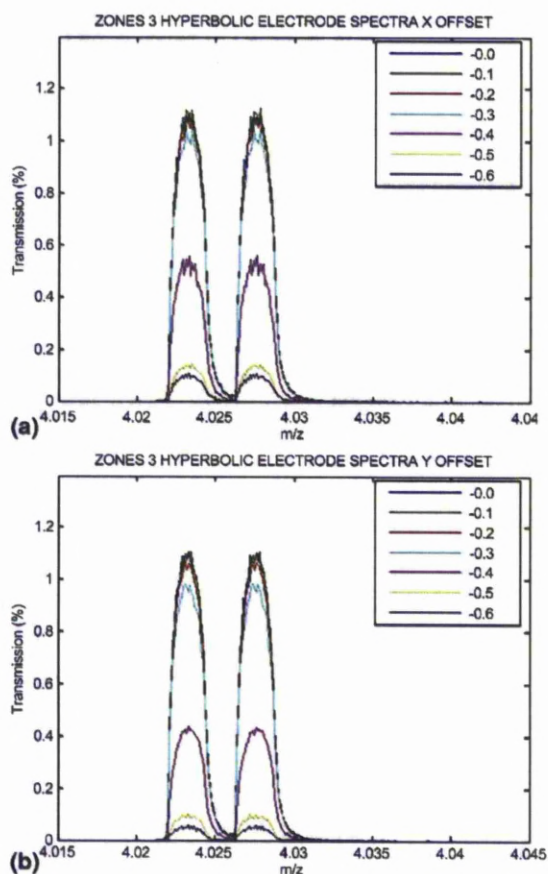
Figure 6. Mass spectra for a range of QMF to ion source alignment tolerances (mm) (L = 300 mm, F = 6 MHz, r_0 = 2.76 mm, Rs = 0.4 mm, Ei = 15 eV) upper X axis misalignment **(a)** and lower Y axis misalignment **(b)**.

given displacement. Displacement in the positive direction results in a similar effect has confirmed this behavior and is due to the asymmetry of the QMF acceptance. For the condition tested, a tolerance of ±0.2 mm would probably be acceptable. The effect of the fringing fields is not reported in the paper. This is the subject of continuing work requiring three dimensional modeling of the ion injection and extraction process from the QMF.

Conclusions

To provide adequate mass discrimination to resolve the peaks of hydrogen and helium isotopes presents certain difficulties. Due to their low mass, these isotopes have a relatively high velocity, which results in them experiencing a low number of rf cycles in their passage through the QMF and results in poor mass resolution with the average QMS. The use of hyperbolic electrodes is the best option to maximize the theoretical resolution, which is necessary for this application.

Our simulations show that the use of hyperbolic electrodes in conjunction with operation in stability zone 3 provides resolutions > 1000, which exceeds the minimum required performance criteria for separation of HT^+ and D_2^+ given in the introduction. The closeness of the species discussed demands high-resolution to achieve mass discrimination and to achieve adequate abundance sensitivity. This places tight constraints on the tolerance budget for the control electronics electrode drive system. The high mass tail has a greater effect than the lower mass tail on abundance sensitivity for these two species. Tighter control of the QMF to ion source alignment accuracy is required in the y-axis compared to the x-axis due to the narrower y-axis stability area. The results show that there is scope to optimize the choice of QMF length and drive frequency. We conclude that further work to include the design and manufacture of a prototype instrument is justified on the basis of the results reported here, and is necessary to investigate and quantify the performance characteristics experimentally.

Acknowledgments

References

1. Dawson, P. H. The Mass Filter: Design and Performance. In *Quadrupole Mass Spectrometry and Its Applications*, Austin, W. E., Holme, A. E., Leck, J. H., Eds.; Elsevier: Amsterdam 1976; pp 121–152.
2. Kay, G. W. C.; Laby, T. H. Fundamental Constants. In *Tables of Physical and Chemical constants and some Mathematical Functions*, Longman: London and New York, 1986; pp 14–16.
3. Ellefson, R. E.; Moddeman, W. E.; Dylia, H. F. Hydrogen Isotope Analysis by Quadrupole Mass Spectrometry. *J. Vac. Sci. Technol.* **1981**, 18, 1062–1066.
4. Hiroki, S.; Abe, T.; Murakami, Y. Separation of Helium and Deuterium Peaks with a Quadrupole Mass Spectrometer by Using the Second Stability Zone in the Mathieu Diagram. *Rev. Sci. Instrum.* **1992**, 63(8), 83874–3876.
5. Hiroki, S.; Abe, T.; Murakami, Y. Detection of a 10^{-4} Helium Peak in a Deuterium Atmosphere Using a Modified High-Resolution Quadrupole Mass Spectrometer. *Rev. Sci. Instrum.* **1994**, 65(6), 1912–1917.
6. Frattolillo, A.; De Ninno, A. A Powerful Tool to Quantitatively Detect Tiny Amounts of ^4He in a Deuterium Rich Background for Fusion Research. *Proceedings of the 22nd IEEE Symposium on Fusion Engineering;* Albuquerque, NM, June, 2007.
7. Hiroki, S.; Abe, T.; Murakami, Y. Sensitive Helium Leak Detection in a Deuterium Atmosphere Using a High-Resolution Quadrupole Mass Spectrometer. *Vacuum* **1996**, 47(6/8), 767–769.
8. Day, C. The Use of a High-Resolution Quadrupole Mass Spectrometer System for Selective Detection of Helium and Deuterium. *Vacuum* **1998**, 51(1), 21–30.
9. Du, Z.; Douglas, D. J.; Konenkov N. Elemental Analysis with Quadrupole Mass Filters Operated in Higher Stability Regions. *J. Anal. At. Spectrom.* **1999**, 14(8), 1111–1119.
10. Hiroki, S.; Abe, T.; Murakami, Y.; Yanagishita, K.; Nakamura, S. Development of a Quadrupole Mass Spectrometer Using the Second Stable Zone in Mathieu's Stability Diagram. *Rev. Sci. Instrum.* **1991**, 62(9), 2121–2124.
11. Gibson, J. R.; Taylor, S. Prediction of Quadrupole Mass Filter Performance for Hyperbolic and Circular Cross Section Electrodes. *Rapid Commun. Mass Spectrom.* **2000**, 14, 1669–1673.
12. Bracco, G. Comparison of Quadrupole Mass Filters Equipped with Rods of Different Convexity: An Analysis by Finite Element

Performance of a Quadrupole Mass Spectrometer Under the Influence of Transverse Magnetic Field

Sarfaraz U. Syed, Jeyan Sreekumar, Boris Brkic, John R. Gibson, and Stephan Taylor
Department of Electrical Engineering and Electronics, University of Liverpool, Liverpool, United Kingdom

We consider the case of a quadrupole mass spectrometer (QMS) in which a static magnetic field is applied axially in the z-direction along the length of the mass filter. The theoretical approach assumed in the model is that the QMS contains hyperbolic rods as electrodes and that the magnetic field acts over the full length of the mass filter assembly. Initial experimental results with argon and helium for a low-resolution instrument confirm the predicted theoretical trends. The analysis also predicts for which values of operating parameters an enhancement of the instrument resolution is achieved when an axial magnetic field is applied. The model predicts instrument resolution R >3000 for a QMS with a 200 mm long mass filter via application of an axial magnetic field. (J Am Soc Mass Spectrom 2010, xx, xxx) © 2010 Published by Elsevier Inc. on behalf of American Society for Mass Spectrometry

First described by W. Paul and H. Steinwedel in 1953 [1], a quadrupole mass spectrometer (QMS) is used to measure molecular masses and relative composition based on mass-to-charge m/z ratio of charged particles. It consists primarily of the following three components: an ion source, a mass analyzer, and an ion detector [2]. Examples of mass analyzers include the quadrupole mass filter (QMF) [3], ion trap [4, 5], and time of flight MS [6], each of which provide different performance and operational characteristics. Attributes of the QMS such as versatility, accuracy, low cost, mass range, and sensitivity have ensured that it has been deployed in a wide range of applications, varying considerably from the modest residual gas analyzer to high-performance mass spectrometer for chemical analysis of simple and complex molecules, e.g., when used in conjunction with gas chromatography [7, 8]. Different applications have different requirements for resolution, sensitivity, and stability.

There have been many analytical predictions of the behavior of QMS. Dawson used matrix methods to calculate ion transmission for various scan lines and various apertures both with and without fringing fields, based on maximum ion displacements for mass filters [9]. Later research describes the performance of the QMS more comprehensively by solving the Mathieu equation in two dimensions for an infinitely long mass filter [2]. Batey showed that some features of the behavior of the QMS could be predicted by tracing the motion of ion through the mass filter [10]. Muntean used the matrix method to develop a computer simulation program to model ion transmission through the filter by calculating ion trajectories in radio frequency (rf) only quadrupoles [11]. More examples of such types of analytical work include the modeling of ion transmission through the filter by calculating ion trajectories in exactly determined hyperbolic quadrupole fields [12], the effects of rf frequency, phase and magnitude on the performance of QMS [13], and the effects of initial ion energy and quadrupole rod length on transmission percentage of ions through the mass filter along with the effects of aperture parameters [14]. Some workers have developed computational methods to determine the trajectories of large number of ions in QMS; their computer program generates large number of ions (at least 10^5 ions injected into the quadrupole model at each point on the mass scale), thus providing a detailed computer simulation for both hyperbolic and circular rods [15, 16]. Douglas and Konenkov have used numerical calculations to investigate the influence of electrode radius r to field radius r_0, which is referred to as (r/r_0) on the peak shape for a linear QMF constructed with round rods [17]. Other workers have used commercially available software tools, such as SIMION 3D, to compute field conditions and ion trajectories of a commercial QMS with a number of imperfections, as compared to ideal hyperbolic geometry [1]. Hogan and Taylor performed computer simulation with a large number of ions (10^8) to investigate the operation of QMS in first and third stability zones, and it was concluded that QMS operation in zone 3 of the Mathieu stability diagram provides an improved immunity from the effects of the variation in the value of (r/r_0) compared to zone 1 [18]. More recently, Sreekumar et al. performed

Address reprint requests to Dr. S. Taylor, Department of Electrical Engineering and Electronics, University of Liverpool, Brownlow Hill, Liverpool L69 3GJ, U.K. E-mail: s.taylor@liv.ac.uk

simulations with a large number of ions ($>10^7$) to determine the required resolution for the qualitative and quantitative identification of low mass isotopes in the mass range 1–6 u [19].

The two main operating characteristics of a quadrupole mass filter are the mass range and the maximum resolution. The maximum resolution and mass range are dependent upon six basic parameters; these are the length and the shortest distance between the rods ($2r_0$), the maximum DC supply voltage to the rods, the rf frequency of the quadrupole, the rf supply voltage, and the ion injection energy. To improve the maximum resolution, the dimensions of the QMF or the operating parameters are to be changed. However, geometric modifications to improve performance increase the manufacturing cost and usually the size of the instrument. A low cost method to increase the resolution of a given QMS is the application of magnetic field to the mass filter [20, 21], and is the motivation behind this study. Magnetic fields have long been used in ion traps, quadrupole ion sources, and magnetic sector instruments; however, little work has been done in relation to the application of magnetic field to the QMS. Tunstall et al. found experimentally that the application of static transverse magnetic field to the mass filter of QMS increases the resolution by reducing the long tail on low mass side of the mass spectra [20]. Later work showed the effect of static magnetic field on ion trajectories and resolution. Simulations showed that an applied transverse magnetic field in the x-direction has no effect on ion motion in the x-direction; however, ion motion in the y-direction is both displaced and increased in amplitude, and that this can result in an improvement in QMS performance [21]. The original model [20, 21] was modified for better sensitivity (using a larger number of steps along the mass scale) and to include large number of ions at each point on the mass scale. Some workers have described an rf-only ion trap mode, with high magnetic fields applied to overcome problems such as the low charge state of ions and ion focusing [22]. This method has been used for in-field matrix-assisted laser desorption ionization Fourier transform mass spectrometry. It was found that for a larger ion trap, a high value of applied magnetic field increases the resolution.

In this paper, therefore, we extend the previous work and present new theoretical and experimental results for a QMS operating under a static magnetic field applied in the z-direction, i.e., axially along the length of the mass filter. The numerical model used in the simulation assumes that the QMF contains hyperbolic electrodes and that the magnetic field penetrates along the full length of the filter.

Theory

Ions oscillating tangentially to a magnetic field will experience a Lorentz force $F = q (E + v \times B)$ where v is the instantaneous velocity of the particle and is directly proportional to ion energy E_z, q is electric charge of the particle, E is the strength of electric field and B is the strength of magnetic field [23]. If the electric field is given by conventional hyperbolic potential where U is the amplitude of DC potential applied to rods, V the amplitude of rf potential, f the frequency of the sinusoidal field and r_0 the inscribed radius of the electrodes, for general magnetic field $B = (B_x, B_y, B_z)$ the coupled equations of motion are given by

$$\frac{d^2x}{d^2\xi} = -x\,(a - 2q\,cos\,2\xi) + \left(\frac{dy}{d\xi}b_3 - \frac{dz}{d\xi}b_2\right) \quad (1)$$

$$\frac{d^2y}{d^2\xi} = y\,(a - 2q\,cos\,2\xi) + \left(\frac{dz}{d\xi}b_1 - \frac{dx}{d\xi}b_3\right) \quad (2)$$

$$\frac{d^2z}{d^2\xi} = \left(\frac{dx}{d\xi}b_2 - \frac{dy}{d\xi}b_1\right) \quad (3)$$

In the numerical model the above equations have been written in a dimensionless form where the only dimension that appears is that of length displacement. The time t has become t = $2\xi/\omega$ where ω is the angular frequency equal to $2\pi f$. In the absence of an applied magnetic field the direct potential U and alternating potential V are related to a and q as

$$a = \left(\frac{4eU}{mr_0^2\omega^2}\right) \quad (4)$$

$$q = \left(\frac{2eV}{mr_0^2\omega^2}\right) \quad (5)$$

The components of the magnetic field B are

$$(b_1, b_2, b_3) = \left(\frac{2eB_x}{m\omega}, \frac{2eB_y}{m\omega}, \frac{2eB_z}{m\omega}\right) \quad (6)$$

It can be seen from eqs 1–3 that if the magnetic field is taken to be zero the coupled differential equations reduce to the familiar Mathieu equations for a linear quadrupole. Solving numerically the coupled differential equations gives the trajectories of the ions through the mass filter. From the trajectories it is feasible to determine the conditions which give successful ion transmission for a given mass to charge ratio. This depends on the values of direct potential U, the rf potential V, the rf voltage frequency f, the inscribed radius of the quadrupole rods r_0 the magnetic field strength B, the initial velocity, initial phase and the ion position. The first four parameters appear as the variables of a and q ℓ in the Mathieu equation for ($B = 0$). For B non-zero there will be a further dependence of a and q upon the magnetic field, however a complete theoretical analysis is beyond the scope of this paper. For simplicity we have assumed that the stability diagram for non-zero B is similar in shape to the case for

$B = 0$ and can be approximated by the stability diagram for $B = 0$. From the mass spectrum obtained by the numerical simulation, the resolution R can be found by using the equation $R = M/\Delta M$, where M is the mass of the given spectral peak and ΔM is the width of the mass peak measured at 10% of its height [2].

Simulation Method

A custom software program (QMS-hyperbolic) is used in this study. The program calculates ion trajectories by solving the Mathieu equations using a fourth order Runge-Kutta algorithm. It operates by dividing the ion trajectories into small steps and assuming that over the steps the ion motion in three directions x, y, and z may be uncoupled. Mass scans are computed by ramping the values of U and V with fixed U/V ratio, which sets the resolution of an instrument. An option of introducing magnetic field in all the three directions (Bx, B_y, B_z), along the whole length of the mass filter is also incorporated.

A second program (IonSrc) allows entry conditions for large number of ions (typically 10^6), to be specified, which are subsequently supplied to the mass filter calculation engine to simulate individual trajectories in each case. The IonSrc file assumes a uniformly illuminated ion distribution across a user defined ion source exit radius. Each ion is injected into the QMF with random phase with respect to the rf at the time of entry. Finally, Matlab and Microsoft Excel were used to post process the data and for the generation of graphical results.

Experimental Results

Reported here are the experimental mass peaks for $^{40}Ar^+$ and $^4He^+$ ions without and with an applied magnetic in the z-direction. A conventional single filter QMS instrument supplied by MKS Spectra Products (UK) was used. The QMF length was 100 mm with an electrode diameter of 6.35 mm and field radius of 2.76 mm, excited at 1.8342 MHz. The instrument was operated in Faraday only mode and in this configuration typically used as a residual gas analyzer (RGA). The QMS was housed in a stainless steel chamber pumped by a turbo pump, backed by a rotary backing pump providing with a residual gas pressure of 2×10^{-6} Torr. After admitting the sample gas into the vacuum chamber the working pressure was raised to about 1×10^{-4} Torr. An axial magnetic field is applied in the z-direction of the mass filter by passing a direct current through a solenoid coil wrapped on the stainless steel chamber housing the QMS exterior to the electrode length. The magnetic field is generated by applying a fixed value of current from a DC supply and measured using Hall effect sensor. The value of magnetic flux density was adjusted at 0.015 T for experiments with Argon, whereas for the case with helium it was set at 0.007 T. The resolution was adjusted by setting ion energy to a value of 4.5 eV, this also gives an easily measurable ion current. The emission current was ad-

justed as 0.5 mA and the electron energy in the QMS ion source was set to 70 eV. The magnetic field extended 80% of the length of QMF.

The QMS used the Microvision Plus software with a fully automated high stability data acquisition electronic drive unit for fast dynamic scanning of the mass filter electrode voltages. The start mass, end mass (range), number of steps, sweep rate, and averaging were user selected. A visual display of each mass scan was displayed in real time on the PC.

To demonstrate the effect of magnetic field in the z-direction on resolution of the QMF, $^{40}Ar^+$ and $^4He^+$ mass peaks was obtained with and without the magnetic field B_z applied. Figure 1a shows typical mass peaks obtained experimentally from the QMS for $^{40}Ar^+$, whereas Figure 1b shows mass peaks obtained experimentally for $^4He^+$. From both figures it can be seen that there is a clear improvement in resolution at 10% peak height with magnetic field applied, from approximately $R = 13$ to $R = 19$ for the case with argon and from $R = 4.1$ to $R = 6.1$ for the case with helium. Although such instrument resolutions are low in comparison with more
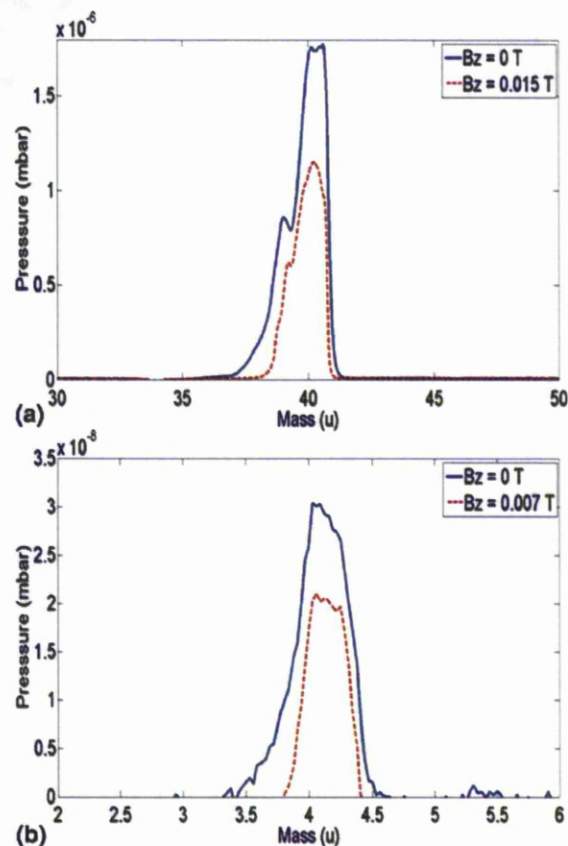

Figure 1. (a) Experimental mass peaks for $^{40}Ar^+$ with and without magnetic field applied (Bz = 0.015 T); (b) experimental mass peaks for $^4He^+$ with and without magnetic field applied (Bz = 0.007 T).

sophisticated instruments (e.g., triple filter QMFs), this experimental result clearly illustrates the resolution enhancement provided by an axially applied magnetic field.

Simulation Results

The Effect of Magnetic Field in the z-Direction on Ion Trajectories

The simulation program includes a trace facility, and this allows many details of individual ions to be recorded. Figure 2 shows typical behavior of the ion trajectories calculated using the theoretical model for ions transmitted with and without the axial magnetic field applied. All the simulations were carried out in stability zone 1 (i.e., $a = 0.23,699$ and $q = 0.706$). The corresponding traces shown in the figure are for the same ion injected into the mass filter at the same point in time (rf phase) and space and at the same point on the mass scale (m = 39.96 u). The upper trace of the figure is for the case with no field applied and lower trace with B_z of 0.03 T. Ion motion in Figure 2 originates at $x = 2.45 \times 10^{-4}$ m and $y = 7.70 \times 10^{-6}$ m with initial velocity of 4.90×10^3 m/s. In the lower trace, due to the Lorentz force provided by B_z, the amplitude of ion trajectory along y-direction increases and the amplitude of the trajectory oscillations in the x-direction decreases. The application of magnetic field therefore displaces the

ion in the y direction so that the ion is lost through impact with the electrodes. It should be noted that ion motion in both the x- and y-directions is affected if the magnetic field is applied in the z-direction. This is in contrast to the case of magnetic field application in the x- direction, where ion motion only in y-direction is affected [20].

The Effect of Magnetic Field in z-Direction on the Resolution of QMS

The simulated mass peaks for $^{40}Ar^+$ ions using the computer software are shown in Figure 3. All the simulations used 200 steps across the mass range, with 1.5×10^5 ion trajectories run at each point on the peak. Mass peaks for $^{40}Ar^+$ are generated for a hyperbolic quadrupole mass filter with length (l) of 100 mm. The inscribed radius of the QMF was taken to be 1.5 mm. The frequency of the rf voltage used in the simulation was 5 MHz and the ion energy was chosen as 5 eV. The ion source radius (r_{ie}) was selected as 0.5 mm and the exit radius was chosen as 3 mm. The operating point (U/V ratio) was selected as 99.99%, where 100% corresponds to the intersection of the scan line with the peak of the Mathieu stability diagram at $U/V = 0.168$. Figure 3a shows the behavior of the resolution, measured at 10% peak height as a function of axial magnetic field for three different lengths of QMF. For L = 100 mm the resolution
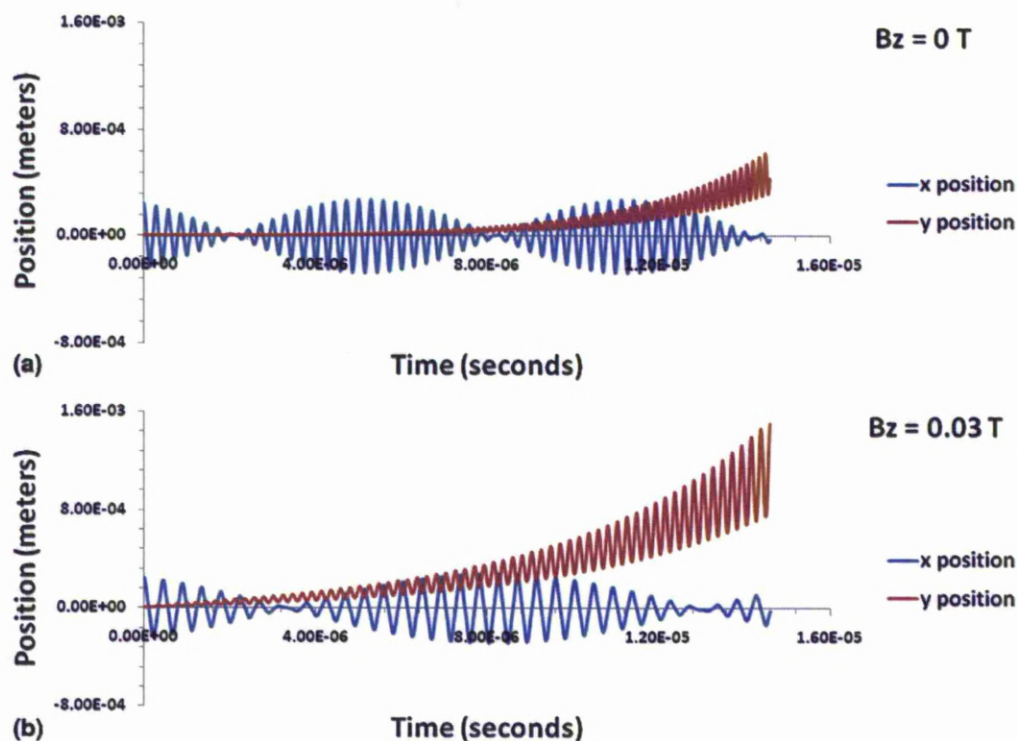

Figure 2. Numerical simulation of ion trajectories in x and y directions for $^{40}Ar^+$ with (a) Bz = 0 (upper trace) and (b) Bz = 0.03 T (lower trace).

T. A low-amplitude structure is present across the low mass and high mass sides of the mass peaks, due to minor changes in the acceptance of the QMF as the position of the mass scan changes. This is because the initial phase space positions of a large number of ions are very close to the QMF acceptance boundary, resulting in small local variations of transmission as the mass scan traverses the mass peak. This observed structure on the peak is an artifact of the simulation and can be reduced by increasing the number of ions although at the expense of increased simulation time [17].

The Performance of the QMS and the Effect of Ion Energy on Resolution in the Presence of Magnetic Field in the z-Direction

Figure 4a shows the dependence of maximum resolution on number of rf cycles without and with an applied magnetic field. The relationship between maximum resolution and number of rf cycles (N) is well known and is given by $M/\Delta M = N^n/K$, where n is the slope and K is a constant [2]. For simulations without the magnetic
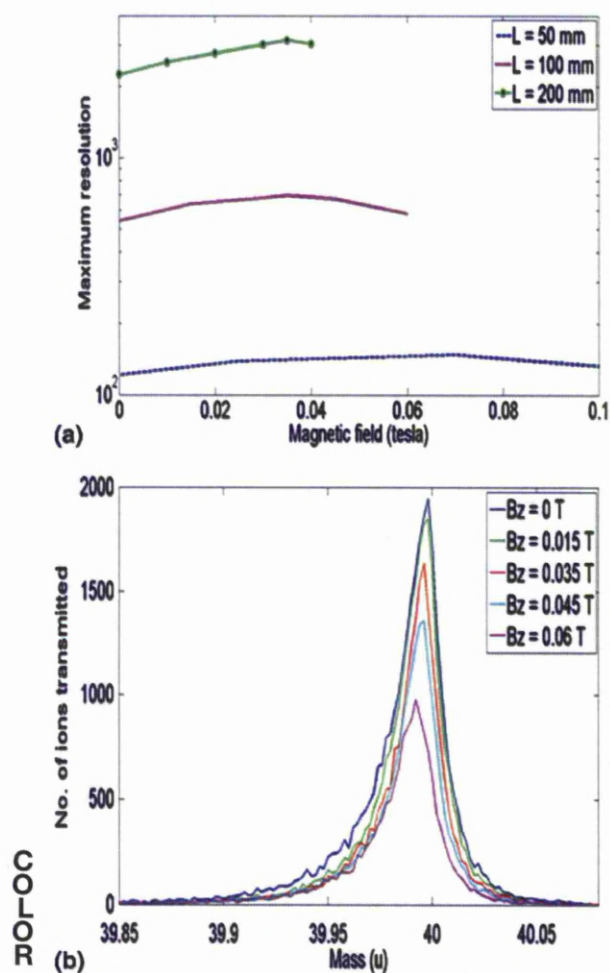
Figure 3. (a) The effect of magnetic field on resolution applied in z-direction (solid line L = 100 mm, dotted L = 50 mm, hyphenated L = 200), (b) simulated mass peaks for $^{40}Ar^+$ with and without magnetic field for L = 100 mm.
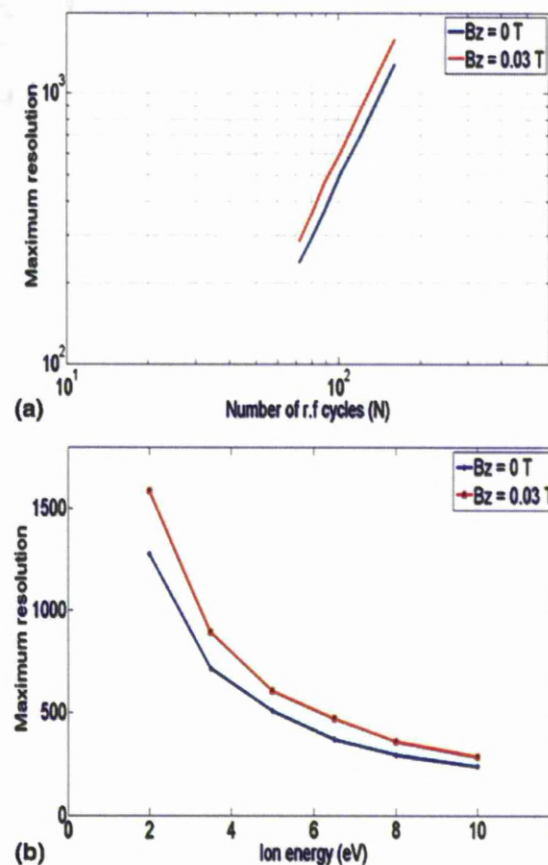

Figure 4. (a) The dependence of maximum resolution on number of rf cycles with and without an applied magnetic field, (b) the dependence of maximum resolution on ion energy with and without an applied magnetic field.

increases as Bz is varied between 0 and 0.035 T, and then decreases as it is varied between 0.035 and 0.06 T, indicating that the QMS resolution will not increase indefinitely with Bz. This is because as Bz increases, the peak shape eventually degrades. A similar effect is seen for shorter and longer QMF: resolution rises with applied Bz reaching a maximum value, then decreases. In the case of L = 200 mm, the predicted value of resolution is in excess of 3000 which, if achieved in practice, would allow specialist high-resolution RGA applications.

Figure 3b shows a set of peaks for $^{40}Ar^+$ within a hyperbolic QMF at different values of magnetic field (Bz) for a QMF of length L = 100 mm. An increase in resolution is clearly observed up to a magnetic field of 0.035T. Transmission through the QMF decreases as magnetic field increases, which results in reduction of QMS resolution at higher values of magnetic field 0.045 to 0.06

field the value of n was found to be 2.05 and that of K to be about 27. For simulations with $B_z = 0.03$ T, the value of n was found to be 2.18 and that of K to be about 40. These results clearly indicate that the predicted performance of the QMS increases in the presence of an axial magnetic field. Figure 4b shows the dependence of maximum resolution on ion energy for $^{40}Ar^+$ with and without magnetic field applied. As can be seen from Figure 4b, in both cases, resolution decreases with increase in ion energy. However, it can also be observed that percentage increase in resolution with magnetic field decreases as ion energy increases. An increase of ~24.5% in resolution at 2 eV can be seen, whereas an increase of only 19.5% at 10 eV is seen at the same value of magnetic field applied.

The effect can be best demonstrated with the help of ion trajectories in the presence of magnetic field at different ion energies. Figures 5 and 6 show trajectories of ions transmitted with and without magnetic field, at ion energies of 2 and 10 eV, respectively. The corresponding traces shown in the figures are for the same ion injected into the QMF at the same point in time (rf phase) and space and at the same point on the mass scale (m = 40.00 u). In both figures the upper trace is for the case with no field applied and lower trace with Bz of 0.03 T. In Figure 5 the ion motion originates at $x = -2.03 \times 10^{-4}$ m and $y = -2.15 \times 10^{-4}$ m with initial velocity of 3.10×10^3 m/s. It can be seen from the figure that in the presence of magnetic field at lower ion

energy (2 eV) ion motion in both the directions is affected. It is also seen that the amplitude of ion motion in the x-direction increases, whereas the amplitude in y-direction decreases.

In Figure 6 the ion motion originates at $x = 2.94 \times 10^{-4}$ m and $y = -1.78 \times 10^{-4}$ m with initial velocity of 6.93×10^3 m/s. It can be observed from the figure that increase in ion energy has a major impact on behavior of ion trajectories in the presence of magnetic field. It can be seen that ion motion in the x-direction remains unaffected, while ion motion in the y- direction is modified. It can be concluded that for a QMF with magnetic field applied in the z-direction, the effect of magnetic field on resolution is greater at lower ion energies. This is due to the increased length of time that the ion experiences the magnetic field.

Conclusions

Experimental results for a low-resolution QMS instrument show an increase in resolution when a static, axial magnetic field is applied along the mass filter in the z-direction. This enhanced resolution observed experimentally has been simulated theoretically using our numerical model, which solves the equation of motion for individual ions injected into the QMF with a magnetic field applied. By determining the ion trajectories for a large number of ions ($>10^5$), mass spectra may be simulated. The effects
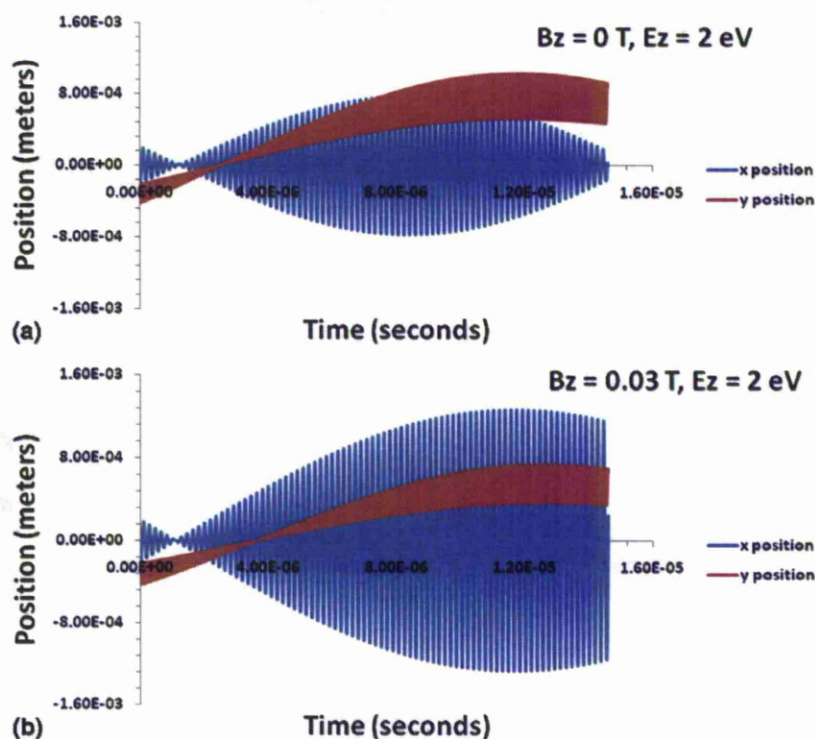

Figure 5. Numerical simulation of ion trajectories in x and y directions for $^{40}Ar^+$ with $E_z = 2$ eV and with (**a**) Bz = 0 (upper trace) and (**b**) Bz = 0.03 T (lower trace).
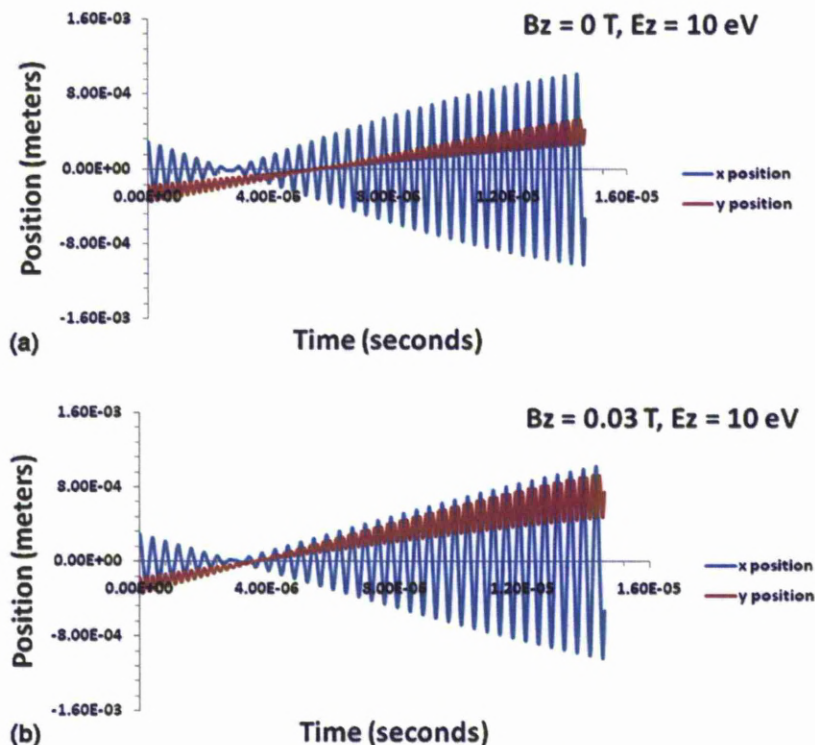
Figure 6. Numerical simulation of ion trajectories in x and y directions for $^{40}Ar^+$ with $E_z = 10$ eV and with (**a**) Bz = 0 (upper trace) and (**b**) Bz = 0.03 T (lower trace).

may be explained by considering the additional Lorentz force produced by ion motion in the magnetic field. All ions oscillating transversely to the applied magnetic field will experience a Lorentz force in addition to the time varying electrostatic force due to alternating quadrupole field. This results in rejection of ions in the low mass tail as well as high mass tail, giving increased resolution for a given set of operating parameters. High resolutions (R > 3000) are predicted for QMFs of length 200 mm as a result of the applied magnetic field which allows wider instrument application.

References

1. Blaum, K.; Geppert, C.; Muller, P.; Nortershauser, W.; Otten, E.W.; Schmitt, A.; Trautmann, N.; Wendt, K.; Bushaw, B. A. Properties and Performance of a Quadrupole Mass Filter Used for Resonance Ionization Mass Spectrometry. *Int. J. Mass Spectrom.* **1998**, *181*, 67–87.
2. Dawson, P. H. Quadrupole Mass Spectrometry and Its Applications; Elsevier: Amsterdam, 1976;
3. Douglas, D. J. Linear Quadrupoles in Mass Spectrometry. *Mass Spectrom. Rev.* **2009**, *28*, 937–960.
4. Schwartz, J. C.; Senko, M. W.; Syka, J. E. P. A two-Dimensional Quadrupole Ion Trap Mass Spectrometer. *J. Am. Soc. Mass Spectrom.* **2002**, *13*, 659–669.
5. Hager, J. W. A New Linear Ion Trap Mass Spectrometer. *Rapid Commun. Mass Spectrom.* **2002**, *16*, 512–526.
6. Wiley, W. C.; McLaren, I. H. Time-of-Flight Mass Spectrometer with Improved Resolution. *Rev. Sci. Instrum.* **1955**, *26*, 1150–1157.
7. Taylor, S.; Srigengan, B.; Gibson, J. R.; Tindall, D.; Syms, R.; Tate, T.; Ahmad, M. A Miniature Mass Spectrometer for Chemical and Biological Sensing. *Proc. SPIE 200, 4036*, 187–193.
8. Taylor, S.; Tunstall, J. J.; Leck, J. H.; Tindall, R. F.; Jullien, J. P.; Batey, J.; Syms, R. R. A.; Tate, T.; Ahmad, M. M. Performance Improvements for a Miniature Quadrupole with a Micromachined Mass Filter. *Vacuum* **1999**, *53*, 203–206.
9. Dawson, P. H. A Detailed Study of Quadrupole Mass Filter. *Int. J. Mass Spectrom. Ion Phys.* **1974**, *14*, 317–337.
10. Batey, J. H. Quadrupole Gas Analyzers. *Vacuum* **1987**, *37*, 659–668.
11. Muntean, F. Transmission Study for rf-Only Quadrupoles by Computer Simulations. *Int. J. Mass Spectrom. Ion Processes* **1995**, *151*, 197–206.
12. Reuben, A. J.; Smith, G. B.; Moses, P.; Vagov, A.V.; Woods, M. D.; Gordon, D. B.; Munn, R. W. Ion Trajectories in Exactly Determined Quadrupole Fields. *Int. J. Mass Spectrom. Ion Processes* **1996**, *154*, 43–59.
13. Ma, F. M.; Taylor, S. Simulation of Ion Trajectories Through the Mass Filter of a Quadrupole Mass Spectrometer. *IEE Proc.-Sci. Meas. Technol.* **1996**, *143*(1), 71–76.
14. Voo, A. C. C.; Ng, R.; Tunstall, J. J.; Taylor, S. Transmission Through the Quadrupole Mass Filter: The Effect of Aperture and Harmonics. *J. Vac. Sci. Technol. A* **1997**, *15*(4), 2276–2281.
15. Gibson, J. R.; Taylor, S.; Leck, J. H. Detailed Simulation of Mass Spectra for Quadrupole Mass Spectrometer systems. *J. Vac. Sci. Technol. A* **2000**, *18*(1), 237–243.
16. Gibson, J. R.; Taylor, S. Prediction of Quadrupole Mass Filter Performance for Hyperbolic and Circular Cross Section Electrodes. *Rapid Commun. Mass Spectrom.* **2000**, *14*, 1669–1673.
17. Douglas, D. J.; Konenkov, N. V. Influence of the Sixth and Tenth Harmonics on the Peak Shape of a Quadrupole Mass Filter with Round Rods. *Rapid Commun. Mass Spectrom.* **2002**, *16*, 1425–1431.
18. Hogan, T. J.; Taylor, S. Performance Simulation of a Quadrupole Mass Filter Operating in the First and Third Stability Zones. *IEEE* **2008**, *57*(3), 498–508.
19. Sreekumar, J.; Hogan, T. J.; Taylor, S.; Turner, P.; Knott, C. A Quadrupole Mass Spectrometer for Resolution of Low Mass Isotopes. *J. Am. Soc. Mass Spectrom.* **2010**,
20. Tunstall, J. J.; Taylor, S.; Vourdas, A.; Leck, J. H.; Batey, J. Application of Static Magnetic Field to the Mass Filter of a Quadrupole Mass Spectrometer. *Vacuum* **1999**, *53*, 211–213.
21. Srigengan, B.; Gibson, J. R.; Taylor, S. Ion Trajectories in Quadrupole Mass Spectrometer with a Static Transverse Magnetic Field Applied to Mass Filter. *IEE Proc-Sci. Meas. Technol.* **2000**, *147*(6), 274–278.
22. Gooden, J. K.; Rempel, D. L.; Gross, M. L. Evaluation of Different Combinations of Gated Trapping, rf-Only Mode and Trap Compensation for In-Field MALDI Fourier Transform Mass Spectrometry. *J. Am. Soc. Mass Spectrom.* **2004**, *15*, 1109–1115.
23. Kraus, J. D. Electromagnetics; McGraw-Hill: New York, 1991;